Pergamon

Micron, Vol. 27, No. 3–4, pp. 265–299, 1996

0968–4328/96 $32.00

PII: S0968–4328(96)00011–X

Valence Electron Excitations and Plasmon Oscillations in Thin Films, Surfaces, Interfaces and Small Particles

Z. L. WANG

School of Materials Science and Engineering, Georgia Institute of Technology, Atlanta, GA 30332-0245, U.S.A.

Abstract—Plasmon oscillation is a collective excitation of electrons in a valence band of a solid material. The motion and polarization of valence electrons under the impact of a fast moving charged particle directly reflect the solid state properties of the material. Oscillations of surface charges depend sensitively on dielectric properties of the material and, more importantly, on the geometrical configuration of the media. The advances of electron microscopy techniques have made it possible to study local excitations from each individual particle smaller than a few nanometers in diameter. Dielectric response theory has shown remarkable success in describing the observed valence-loss spectra and resonance modes. This review gives a systematic description on the classical electron energy-loss theory and its applications in characterizing interband transition and plasmon excitations in thin films, surfaces, interfaces, isolated particles and supported particles of different geometrical configurations. These fundamental studies are important for characterizing many advanced nanophase and nanostructured materials of technological importance. This article is focused on quantitative calculation of valence-loss spectra acquired from different geometrical configurations of dielectric objects. The classical energy-loss theory is equivalent to the quantum mechanical theory, provided all the scattered electrons are collected by the spectrometer. The hydrodynamic model is also described to include fluctuation of electron density in metallic particles smaller than 10 nm in diameter. Applications of valence electron excitation spectroscopy are demonstrated using numerous experimental results. Copyright © 1996 Elsevier Science Ltd.

Key words: dielectric response theory; valence electron excitation; plasmon; interband transition; small particles; electron energy-loss spectroscopy; scanning transmission electron microscopy.

CONTENTS

I. INTRODUCTION

When a fast electron passes through a thin metal foil, the most noticeable energy-loss is to plasmon oscillations in the sea of conduction electrons. For an ideal case in which the electrons can move 'freely' in the sea, the system can be treated as an electron gas. This case is best represented by aluminum metal. The outer shell electrons can be considered as free electrons. The negatively charged particles are mixed with nuclei, forming a solid state plasmon 'gas'. The resonance frequency of this plasmon is directly related to the density of electrons in the solid. This simple plasmon

* Corresponding author. Fax: (404) 894-9140; e-mail: zhong.wang@mse.gatech.edu

model may also be adopted to describe the valence electron excitation of semiconductor materials, such as Si. For non-conductive materials, the plasmon model is generalized into valence electron excitation. In practice, plasmon oscillation has been used as a universal phrase to describe the excitation of valence electrons in solids although it was first defined for free electron metals.

Valence band structure is solely determined by the solid state structure of the material. The collective excitation of electrons in the valence states will produce numerous low-energy excited states, resulting in the energy-loss of the incident electron. A detailed study of valence electron excitation by electron energy-loss spectroscopy (EELS) can provide substantial information about the structure of valence bands. The geometrical shape of the medium determines resonance modes of surface charge oscillations. Surface charges induced by the moving particle can affect the physical adsorption of the particle on the surface (Echenique and Pendry, 1975; Schmeits and Lucas, 1977). Plasmon excitations can also reduce or enhance the emission rate of secondary electrons from the solid surface because of the Coulomb interaction (Gervasoni and Arista, 1992; Mullejans *et al.*, 1993).

Many sophisticated quantum mechanical many-body theories have been developed to characterize the interactions of electrons in metals (Bohm, 1953; Nozieres and Pine, 1958; Ferrell, 1956, 1957; Stern and Ferrell, 1960). These theories are based on the harmonic oscillator model of plasmons; the plasmon is considered as a quantum excitation, analogous to a phonon in lattice dynamics. However, the theories become very complex if the solid is a non-metallic material so that the electron gas model is no longer valid. The valence band of a crystalline material is a collection of many electronic states, and it is usually characterized by a dielectric function $\varepsilon(\omega,\mathbf{q})$, which depends on the frequency ω of the plasmon oscillation and the wave vector $\mathbf{q}$ of the disturbance (Lindhard, 1954). The dielectric function characterizes the polarization response of the medium to an electric field generated by an external source, such as a fast moving electron. This interaction process results in the loss of electron energy due to excitation of interband transitions and plasmon oscillations. The analysis of electron energy-loss spectra provides direct information on the excitation modes of the solid. It is now possible to generate an electron probe smaller than 0.5 nm in a scanning transmission electron microscope (STEM), so that the local excitation of a small particle can be analyzed. This is a powerful technique which allows one to study valence-band electronic structures of nanophase materials at high spatial resolution.

There are a few review articles on dielectric excitation of surfaces. The review by Bah *et al.* (1992) was focused on layered dielectric and composite dielectric materials. Dielectric excitations in spherical and cylindrical geometries were described by Kliewer and Fuchs (1974). The review by Lucas and Sunjic (1972) was concentrated on the quantum mechanical description of plasmon excitation, and a comparison between the classical theory and the quantum theory was also given. The book by Raether (1980) gave a comprehensive description on the volume and surface excitations. The review of Echenique *et al.* (1990) gives a thorough description on the dynamic screening of a fast ion interacting with condensed matter. A recent review by Schattschneider and Jouffrey (1995) gives a systematic coverage on the nature and dispersion of plasmon oscillations. Most of these reviews concentrate on the plasmon resonance modes rather than the energy-loss spectra.

The objective of this review is focused on quantitative calculations of EELS spectra for different dielectric media in order to provide a comprehensive coverage of the valence electron excitation in surfaces, interfaces, nanotubes and supported and unsupported particles. Starting from fundamental dielectric response theory, a step-by-step application of the theory for calculating valence-loss spectra in planar interface geometries is presented. Then, the applications of the theory in various excitation configurations are reviewed. The effect of electron density fluctuation in a small metal particle is considered with the use of the hydrodynamic model. Finally, the equivalence is proven between classical energy-loss theory and the quantum mechanical approach, thus establishing a basis for applying dielectric response theory in valence electron excitations.

This article covers only collective excitation in solids, which occurs in the energy-loss range less than approximately 30–40 eV. No multiple- and multi-plasmon excitations are considered. Applications of inner-shell ionization edges in EELS can be found elsewhere (Egerton, 1986; Colliex, 1984). A review of the various inelastic scattering processes in electron diffraction and imaging can be found elsewhere (Wang, 1995).

II. CLASSICAL ELECTRON ENERGY-LOSS THEORY

A. *Dielectric function*

The electron energy loss associated with a single-loss (or single-scattering) plasmon excitation is usually less than 40 eV. The real space scale associated with charge oscillations is for the most part much larger than the interatomic distance in solids. Thus, the response of a dielectric system to the long-range electromagnetic fields can be described by a continuum medium theory, and the medium is characterized by a macroscopic dielectric function $\varepsilon(\omega,\mathbf{q})$. A majority of the experimental studies of surface dynamical properties are focused on the long-wavelength surface excitation. Dielectric response theory has shown remarkable success in describing experimental results in this field.

The dielectric function depends not only on the frequency of the charge oscillation but also on the wave vector, $\mathbf{q}$, of the excitation. The $\mathbf{q}$ dependence of ε is referred to as the dispersion characteristic of the dielectric medium; this relationship characterizes the

non-local response property of the medium as described below. For a bulk, homogeneous, isotropic system, the electric displacement vector $(\tilde{\mathbf{D}})(\mathbf{r},t)$ is related to the electric field by

$$(\tilde{\mathbf{D}},)(\mathrm{r},t) = \varepsilon_0 \int_{-\infty}^{\infty} \mathrm{d}t' \int_{-\infty}^{\infty} \mathrm{d}\mathbf{r}' \varepsilon(t-t', \mathbf{r}-\mathbf{r}')\tilde{\mathbf{E}}(\mathbf{r}', t'), \tag{2.1}$$

where $\varepsilon(\mathbf{r}-\mathbf{r}', t-t')$ is a real-space, real-time response function. For a general case, ε is a tensor containing nine components. The Fourier transform of this equation in frequency space is

$$\mathbf{D}(\mathbf{r},\omega) = \varepsilon_0 \int_{-\infty}^{\infty} \mathrm{d}\mathbf{r}')\varepsilon(\omega, \mathbf{r}-\mathbf{r}')\mathbf{E}(\mathbf{r}', \omega). \tag{2.2}$$

This is a convolution relation. In this paper, the Fourier transform of a function $\tilde{\mathrm{A}}$ (r,t) is denoted as $\mathbf{A}(\mathbf{r},\omega)$. The entire theoretical analysis of this paper is based on the local response approximation for homogeneous media, which means

$$\varepsilon(\omega, \mathbf{r}-\mathbf{r}') = \delta(\mathbf{r}-\mathbf{r}')\varepsilon(\omega), \tag{2.3}$$

and $\varepsilon(\omega)$ is independent of the wave vector $\mathbf{q}$, i.e., no dispersion. Thus

$$\mathbf{D}(\mathbf{r},\omega) = \varepsilon_0\varepsilon(\omega)\mathbf{E}(\mathbf{r},\omega). \tag{2.4}$$

The dielectric function is usually a complex function. As will be shown in future sections, the imaginary component ε_r describes the energy loss of the incident electron.

Figure 1a shows a plot of the real (ε_r) and imaginary (ε_i) components of the dielectric function of GaAs. The imaginary part has the same order of magnitude as the real component. Fig. 1b shows the energy loss function of GaAs. A plasmon peak located at 14.5 eV is seen which corresponds to the excitation of the volume plasmon. The experimentally measured dielectric functions for simple compounds, semiconductors and metals have been tabulated in the book edited by Palik (1985).

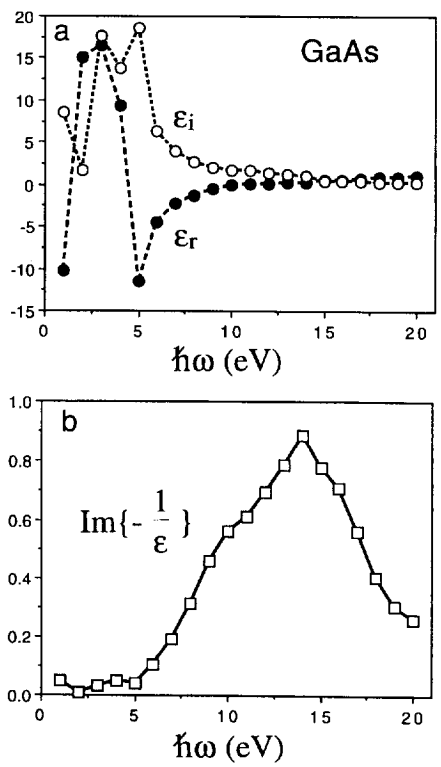

Fig. 1. Plot of the real and imaginary components of the dielectric function of GaAs. Energy resolution 1 eV.

If the dielectric response is non-local (i.e. ε depends on $\mathbf{r}$), $\mathbf{D}$ is a convolution of ε with $\mathbf{E}$ in real space. In momentum space, $\mathbf{D}(\mathbf{q}, \omega) = \varepsilon_0\, \varepsilon(\omega, \mathbf{q})\, \mathbf{E}(\mathbf{q}, \omega)$. For an inhomogeneous medium, the dielectric function is expressed in a form of tensor, a description of the plasmon excitation can be found elsewhere (Schattschneider and Jouffrey, 1995).

The dielectric function of an ionic crystal is closely related to the phonon characteristics of the crystal. The dielectric function characterizes the polarization response of the medium to an external electric field. The interactions among the atoms directly determine the phonon dispersion relations of the crystal. Thus, the phonon modes directly influence the polarization response of the crystal, because both the nuclei motion and electron motion affect the polarization of the crystal. For a diatomic ionic crystal, the dielectric response function is (Kliewer and Fuchs, 1974)

$$\varepsilon(\omega) = \varepsilon(\infty)\frac{\omega_{\mathrm{LO}}^2 - \omega^2}{\omega_{\mathrm{TO}}^2 - \omega^2}, \tag{2.5}$$

where ω_{TO} is the long-wavelength transverse optical phonon frequency and ω_{LO} is the longitudinal optical frequency. This equation clearly illustrates the relationship between phonon modes in crystals and the dielectric response properties of the crystal.

B. *Dielectric response theory*

This theory aims to give a quantitative description on the response of a dielectric system when it is exposed to an external field. The impact of an incident electron is equivalent to a time-dependent pulse, which causes transitions of valence electrons and results in plasmon oscillations. Classical dielectric response theory is based on the assumptions described below. An incident electron is treated as a classical particle following a pre-defined trajectory, which is assumed not to be affected by the interaction between the incident electron and the dielectric media. There is only one electron interacting with the system at a time; no interaction and no correlation between successive incident electrons is considered. These are excellent approximations for the current and current density provided by a field emission source in STEM (Wang, 1995). In STEM, a fine electron probe smaller than 0.5 nm in diameter is generated, which can be used to probe the local inelastic excitations. The effect produced by the finite size of the probe will be compensated using a convolution technique, as for incoherent scattering.

For high-energy electrons, the velocity of an electron approaches the speed of light. For 100 keV electrons,

$v = 0.53$ c. It is necessary to consider retardation effects in dielectric excitation theory. In this section, dielectric response theory is described and the physical mechanism of classical electron energy-loss theory is introduced. The applications of this general theory will be shown in Section 3. For a homogeneous medium and under the local dielectric response condition, the electric field $\tilde{\mathbf{E}}$ (or displacement vector $\tilde{\mathbf{D}}$ and magnetic field $\tilde{\mathbf{H}}$ (or $\tilde{\mathbf{B}}$) $= \mu_0 \tilde{\mathbf{H}}$ for non-magnetic materials) which are excited in the space are determined by the solution of Maxwell's equations

$$\nabla \times \tilde{\mathbf{E}}(\mathbf{r}, t) = -\frac{\partial \tilde{\mathbf{B}}(\mathbf{r}, t)}{\partial t}, \tag{2.6a}$$

$$\nabla \times \tilde{\mathbf{H}}(\mathbf{r}, t) = \tilde{\mathbf{J}}(\mathbf{r}, t) + \frac{\partial \tilde{\mathbf{D}}(\mathbf{r}, t)}{\delta t}, \tag{2.6b}$$

$$\nabla \cdot \tilde{\mathbf{D}}(\mathbf{r}, t) = \tilde{\rho}(\mathbf{r}, t), \tag{2.6c}$$

and

$$\nabla \cdot \tilde{\mathbf{B}}(\mathbf{r}, t) = 0, \tag{2.6d}$$

where $\tilde{\mathbf{J}}$ is the current density of free charge and ρ is the free charge density function. A transformation is introduced which converts each time-dependent quantity to a frequency-dependent quantity,

$$\mathbf{A}(\mathbf{r}, \omega) = \int_{-\infty}^{\infty} \mathrm{d}t \exp(i\omega t) \tilde{\mathbf{A}}(\mathbf{r}, t), \tag{2.7a}$$

or

$$\tilde{\mathbf{A}}(\mathbf{r}, t) = \frac{1}{2\pi} \int_{-\infty}^{\infty} \mathrm{d}\omega \exp(-i\omega t) \mathbf{A}(\mathbf{r}, \omega). \tag{2.7b}$$

The Maxwell's equations are transformed into

$$\nabla \times \mathbf{E}(\mathbf{r}, \omega) = i\omega \mathbf{B}(\mathbf{r}, \omega), \tag{2.8a}$$

$$\nabla \times \mathbf{H}(\mathbf{r}, \omega) = \mathbf{J}(\mathbf{r}, \omega) - i\omega \mathbf{D}(\mathbf{r}, \omega), \tag{2.8b}$$

$$\nabla \cdot \mathbf{D}(\mathbf{r}, \omega) = \rho(\mathbf{r}, \omega), \tag{2.8c}$$

and

$$\nabla \cdot \mathbf{B}(\mathbf{r}, \omega) = 0. \tag{2.8d}$$

These equations are coupled. The Hertz vector $\tilde{\prod}$ (Stratton, 1941) is now introduced, using which $\mathbf{E}$ and $\mathbf{H}$ are expressed as

$$\mathbf{E}(\mathbf{r}, \omega) = \nabla[\nabla \cdot \tilde{\prod}(\mathbf{r}, \omega)] + \frac{\varepsilon \omega^2}{c^2} \tilde{\prod}(\mathbf{r}, \omega) \tag{2.9a}$$

and

$$\mathbf{H}(\mathbf{r}, \omega) = -i\omega \varepsilon(\omega) \varepsilon_0 \nabla \times \tilde{\prod}(\mathbf{r}, \omega). \tag{2.9b}$$

Substituting (2.9a) and (2.9b) into (2.8a) and (2.8b), for $\mathbf{D}(\mathbf{r},\omega) = \varepsilon\varepsilon_0 \mathbf{E}(\mathbf{r},\omega)$, the equation which determines $\tilde{\prod}$ is

$$[\nabla^2 + \frac{\varepsilon \omega^2}{c^2}] \tilde{\prod}(\mathbf{r}, \omega) = \frac{1}{i\omega \varepsilon(\omega) \varepsilon_0} \mathbf{J}(\mathbf{r}, \omega). \tag{2.10}$$

where $\nabla^2 = [\frac{\partial^2}{\partial x^2} + \frac{\partial^2}{\partial y^2} + \frac{\partial^2}{\partial z^2}]$ is the Laplace operator. Thus, Maxwell's equations are reduced into a single equation. eqn. (2.8d) is automatically satisfied with the magnetic field given by eqn. (2.9b). We now prove that eqn. (2.8c) is also satisfied with the $\mathbf{E}$ and $\mathbf{H}$ given by eqn. (2.9a) and eqn. (2.9b). From eqn. (2.8c) and using eqn. (2.9a) and eqn. (2.10)

$$\rho(\mathbf{r}, \omega) = \nabla \cdot \mathbf{D}(\mathbf{r}, \omega) = \varepsilon\varepsilon_0 \nabla \cdot \mathbf{E}(\mathbf{r}, \omega)$$
$$= \varepsilon\varepsilon_0 \nabla \cdot \left[\nabla^2 + \frac{\varepsilon \omega^2}{c^2}\right] \tilde{\prod}(\mathbf{r}, \omega) = \frac{\nabla \cdot \mathbf{J}(\mathbf{r}, \omega)}{i\omega}, \tag{2.11a}$$

or equivalently

$$\nabla \cdot \tilde{\mathbf{J}}(\mathbf{r}, t) + \frac{\partial \tilde{\rho}(\mathbf{r}, t)}{\partial t} = 0. \tag{2.11b}$$

This is just the law of charge conservation, which holds under any circumstance. Therefore, the Hertz vector covers all the characteristics of the electric and magnetic fields.

When an incident electron strikes a dielectric medium, electric and magnetic fields are generated not only by the incident electron but also by the polarization charges in the medium. In the classical electron energy-loss theory, an incident electron is treated as a particle that moves along a certain trajectory, provided the changes of electron energy and momentum are small. For a high energy electron, the electron trajectory is assumed to be unaffected by the induced charges distributed in the media. Its energy loss equals the work done by the induced charges distributed in the bulk and at the interface and surface to slow down the incident electron. In STEM, the electron is assumed to travel at speed v along the z axis, as shown in Fig. 2, thus the current density for a moving electron is expressed as

$$\tilde{\mathbf{J}}(\mathbf{r}, t) = -ev\, \hat{z}\, \delta(\mathbf{r} - \mathbf{r}_0(t))$$
$$= -ev\, \hat{z}\, \delta(x - x_0)\delta(y)\delta(z - vt), \tag{2.12}$$

where $\hat{z}$ is the unit vector of the z-axis. The solution of $\prod$ is separated into two components,

$$\tilde{\prod}(\mathbf{r}, \omega) = \tilde{\prod}_{\mathrm{i}}(\mathbf{r}, \omega) + \tilde{\prod}_{\mathrm{e}}(\mathbf{r}, \omega) \tag{2.13}$$

$\tilde{\prod}_{\mathrm{e}}(\mathbf{r},\omega)$ is due to the field generated by the moving electron itself and is a special solution of eqn. (2.10); $\tilde{\prod}_{\mathrm{i}}(\mathbf{r},\omega)$ is the homogeneous solution of $[\nabla^2 + \frac{\varepsilon\omega^2}{c^2}]\tilde{\prod}$ $\omega i(\mathbf{r},\omega) = 0$, which is due to the field produced by the induced charges in the dielectric media and at the surface, as schematically shown in Fig. 2.

The resultant solution $\tilde{\prod}$ $(\mathbf{r},\omega)$ must satisfy the following boundary conditions: continuity of the tangential components of $\mathbf{E}(\mathbf{r},\omega)$ and $\mathbf{H}(\mathbf{r},\omega)$ parallel to the surface/interface of the dielectric media at the boundary.

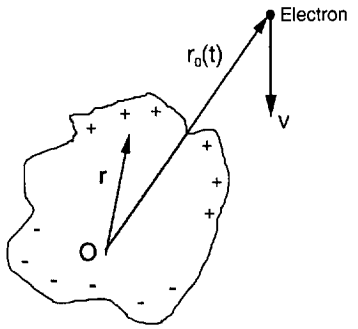

Fig. 2. A schematic model showing the excitation of a dielectric media system by a fast moving electron.

E and **H** are calculated from $\tilde{\prod}$ using eqn. (2.9a) and eqn. (2.9b). These boundary conditions must be met in frequency space, because the dielectric function is frequency-dependent.

In classical physics, electron energy loss is a continuous process, in which the electron is decelerated due to the attractive force $F_z=(-e)\tilde{E}_{iz}$ generated by the induced charges. The energy loss per unit path length is known as stopping power of the media. The stopping power is an important quantity in scanning electron microscopy and it determines the effective penetration depth into the surface of the incident electron (Joy *et al.*, 1994). For a general case in which the incident electron is moving along the z axis, if the instantaneous position of the electron is denoted by $\mathbf{r}_0=(x_0,\ 0,\ vt)$, where x_0 is called the impact parameter, the total energy loss of the incident electron is calculated by

$$\begin{aligned}\Delta E &= \int_{-\infty}^{\infty} dz[-(-e)\tilde{E}_z(\mathbf{r},t)]|_{\mathbf{r}=\mathbf{r}_0(t)} \\ &= \frac{e}{2\pi}\int_{-\infty}^{\infty} dz \int_{-\infty}^{\infty} d\omega \exp(-i\omega t)E_z(\mathbf{r},\omega)|_{\mathbf{r}=\mathbf{r}_0} \\ &= \frac{e}{2\pi}\int_{-\infty}^{\infty} dz \int_{-\infty}^{\infty} d\omega \exp(-i\omega z/v) \\ &\quad \left[\frac{\partial}{\partial z}(\nabla\cdot\tilde{\prod}(\mathbf{r},\omega)) + \frac{\varepsilon\omega^2}{c^2}\tilde{\prod}_z(\mathbf{r},\omega)\right]|_{\mathbf{r}=\mathbf{r}_0},\end{aligned} \tag{2.14}$$

The central task for dielectric response theory is to find the Hertz vector for relevant geometries and impact positions. The total energy loss of the incident electron is calculated according to eqn. (2.14). A detailed application of this exact theory will be demonstrated in Section 3.

C. *Non-relativistic approximation*

The solution of Maxwell's equations could be quite complex for some dielectric geometries. For lower speed electrons, the non-relativistic approximation is usually made, under which the solution is significantly simplified. This approximation is usually adopted to simplify the analytical calculations. For c$\rightarrow\infty$, eqn. (2.9a) and eqn. (2.9b) become

$$\mathbf{E}(\mathbf{r},\omega) = \nabla[\nabla\cdot\tilde{\prod}(\mathbf{r},\omega)], \tag{2.15a}$$

and

$$\mathbf{H}(\mathbf{r},\omega) = -i\omega\varepsilon\varepsilon_0\nabla\times\tilde{\prod}(\mathbf{r},\omega). \tag{2.15b}$$

eqn. (2.10) is approximated as

$$\nabla^2\tilde{\prod}(\mathbf{r},\omega) = \frac{1}{i\omega\varepsilon\varepsilon_0}\mathbf{J}(\mathbf{r},\omega). \tag{2.16}$$

By defining an scalar electric potential

$$V(\mathbf{r},\omega) = -\nabla\cdot\tilde{\prod}(\mathbf{r},\omega), \tag{2.17}$$

using the charge conservation law, $\nabla\cdot\mathbf{J}((\mathbf{r},\omega) - i\omega\ \omega(\mathbf{r},\omega)=0$, applying an operation of $\nabla\cdot$ to both sides of eqn. (2.16), yields

$$\nabla^2 V(\mathbf{r},\omega) = \frac{1}{\varepsilon(\omega)\varepsilon_0}\rho(\mathbf{r},\omega), \tag{2.18}$$

where $\rho(\mathbf{r},\omega)=-\frac{e}{v}\delta(x-x_0)\delta(y)\exp(i\omega z/v)$. This is just Poisson's equation, the solution of which describes the electric field distribution in space. Again, the solution of $V(\mathbf{r},\omega)$ is composed of a special solution $V_e(\mathbf{r},\omega)$ and a homogeneous solution $V_i(\mathbf{r},\omega)$. $V_e(\mathbf{r},\omega)$ is due to the field generated by the moving electron itself and $V_i(\mathbf{r},\omega)$ is the homogeneous solution of $\nabla^2V_i(\mathbf{r},\omega)=0$. The boundary conditions for $V(\mathbf{r},\omega)$ are: the continuity of $V(\mathbf{r},\omega)$ across the boundary, and the continuity of the normal component of the displacement vector across the boundary.

The magnetic field generated by the moving electron will not reduce its speed but may slightly deflect it because the Lorentz force is perpendicular to the moving direction of the particle. This deflection is small for high-energy electrons. Therefore, as far as energy-loss is concerned, the electric potential V is the only required function. The electron energy loss is produced by the potential of the induced charge:

$$\Delta E = \frac{e}{2\pi}\int_{-\infty}^{\infty} dz \int_{-\infty}^{\infty} d\omega \exp(-i\omega z/v)\left[\frac{\partial}{\partial z}(V_i(\mathbf{r},\omega))\right]\Big|_{\mathbf{r}=\mathbf{r}_0}. \tag{2.19}$$

Introducing the inverse Fourier transform of V_i, eqn. (2.19) can be rewritten as

$$\begin{aligned}\Delta E &= \frac{e}{2\pi}\int_{-\infty}^{\infty} dz \int_{-\infty}^{\infty} d\omega \exp(-i\omega z/v) \\ &\quad \left\{\frac{\partial}{\partial z}\left[\int_{-\infty}^{\infty} dt' \exp(i\omega t')\tilde{V}_i(\mathbf{r},\mathbf{r}_0(t'))\right]\right\}\Big|_{\mathbf{r}=\mathbf{r}_0} \\ &= \frac{e}{2\pi v}\int_{-\infty}^{\infty} d\omega \int_{-\infty}^{\infty} dz \exp(-i\omega z/v) \\ &\quad \int_{-\infty}^{\infty} dz' \exp(i\omega z'/v)\left[\frac{\partial}{\partial z}\tilde{V}_i(\mathbf{r},\mathbf{r}_0)\right]\Big|_{\mathbf{r}=\mathbf{r}_0}\end{aligned}$$

$$= \frac{ie}{2\pi v^2}\int_{-\infty}^{\infty} d\omega \int_{-\infty}^{\infty} dz' \exp(i\omega z'/v)$$
$$\int_{-\infty}^{\infty} dz\, \omega \exp(-i\omega z/v)\tilde{V}_i(\mathbf{r},\mathbf{r}_0)|_{\mathbf{r}=\mathbf{r}_0}$$
$$= \frac{e}{\pi v^2}\int_0^{\infty} d\omega \int_{-\infty}^{\infty} dz'$$
$$\int_{-\infty}^{\infty} dz\, \omega\, \mathrm{Im}{-}\exp[i\omega(z'-z)/v]\tilde{V}_i(\mathbf{r},\mathbf{r}_0)|_{\mathbf{r}=\mathbf{r}_0}, \tag{2.20a}$$

since $\tilde{V}_i$ becomes $\tilde{V}_i^*$ if $\varepsilon(\omega)$ is replaced by $\varepsilon(-\omega)$. For a finite system, an assumption of $\tilde{V}_i(\mathbf{r},\mathbf{r}_0)=0$ at $z=\pm\infty$ was made. This assumption may not hold if the dielectric medium is infinitely large. $\tilde{V}_i(\mathbf{r},\mathbf{r}_0)$ is the potential due to the induced charge when a 'stationary' electron is located at $\mathbf{r}_0=(x_0, 0, z')$, i.e. it is the homogeneous component of $\tilde{V}$ satisfying

$$\nabla^2\tilde{V}(\mathbf{r},\mathbf{r}_0) = -\frac{e}{\varepsilon(\omega)\varepsilon_0}\delta(\mathbf{r}-\mathbf{r}_0)$$

for the dielectric media considered. It is important to note that $\tilde{V}_i(\mathbf{r},\mathbf{r}_0)$ is ω-dependent. The potential distribution in space is a quasi-electrostatic potential for each point along the trajectory of the incident electron. The integral over z' is a sum over the contributions made by all the points along the trajectory of the incident electron.

The total energy loss is related to the excitation probability by

$$\Delta E = \int_0^{\infty} d\omega\, \hbar\omega \frac{dP(\omega)}{d\omega}. \tag{2.20b}$$

The comparison of eqn. (2.20a) and eqn. (2.20b) gives

$$\frac{dP(\omega)}{d\omega} = \frac{e}{\pi\hbar v^2}\int_{-\infty}^{\infty} dz'$$
$$\int_{-\infty}^{\infty} dz\, \mathrm{Im}{-}\exp[i\omega(z'-z)/v]\tilde{V}_i(\mathbf{r},\mathbf{r}_0)|_{\mathbf{r}=\mathbf{r}_0} \tag{2.21}$$

Therefore, the calculation of valence-loss spectra is actually to find the solution of the electrostatic potential for a stationary electron located at $\mathbf{r}_0$ in the dielectric-media system. For an isolated sphere, the 'mirror' charge technique can be used and in many complex geometries an analytical solution could even be obtained (Smythe, 1950). The result given by eqn. (2.21) is identical to that obtained based on the theory of self-energy (Echenique *et al.*, 1987a, 1990). Equation (2.21) has been extensively used to calculate the valence-loss spectra in isolated and supported particle geometries (Rivacoba *et al.*, 1994, 1995a). For fast electrons in STEM, the trajectory is usually a straight line unless specified for different scattering configurations, such as in reflection electron microscopy at gracing angle incidence (Wang, 1996) or at normal incidence (Yubero and Tougaard, 1992).

The electron inelastic mean free path Λ is calculated according to

$$\frac{1}{\Lambda} = \int_0^{\infty} d\omega \frac{d^2P}{d\omega dz}.$$

A detailed calculation of Λ for free-electron metals has been given by Ashley *et al.* (1979) and Tung *et al.* (1979). The valence-loss spectra of Si, Cu, Ag, Au, Ti, Fe and Pd have been calculated by Tougaard and Kraaer (1991).

1. *Resonance modes and dispersion relations*

As shown above, the solution of Poisson's equation is required if one is interested in energy-loss spectra. In most cases, the resonance frequencies and modes are the interesting quantities. These are the resonance modes of the dielectric system and are independent of the excitation trajectory of the incident electron. In this case, the solution of Laplace's equation is required:

$$\nabla^2 V_i(\mathbf{r}) = 0. \tag{2.22}$$

The dispersion relation is obtained by matching the boundary conditions of $V_i(\mathbf{r})$.

III. VALENCE-ELECTRON EXCITATION NEAR PLANAR INTERFACES

A. *Surface and interface plasmons*

Dielectric response theory introduced in Section 2.3 is now applied to calculate the electron energy-loss spectra of surfaces (or interfaces). In a general case, an interface is formed by two media with dielectric constants $\varepsilon_1(\omega)$ and $\varepsilon_2(\omega)$ (Fig. 3). The incident electron is assumed to travel at a distance x_0 in medium ε_1 parallel to the interface. The interface is assumed to be infinitely long in order to simplify mathematical operations. For interface excitation as shown in Fig. 3, since the energy-loss of the incident electron is independent of the origin of the y-axis, another transform is introduced (Garcia-Molina *et al.*, 1985):

$$\tilde{\prod}(\mathbf{r},\omega) = \int du_y \int du_z \exp[2\pi i(u_y y + u_z z)] \prod(x, u_y, u_z, \omega). \tag{3.1}$$

Substituting eqn. (3.1) into eqn. (2.10), one has

$$\left[\frac{d^2}{dx^2} - \left(4\pi^2u^2 - \frac{\varepsilon\omega^2}{c^2}\right)\right]\prod(x, u_y, u_z, \omega) = \frac{1}{i\omega\varepsilon\varepsilon_0}\mathbf{J}'(x, u_y, u_z, \omega), \tag{3.2a}$$

where

$$\mathbf{J}'(x, u_y, u_z, \omega) = -2\pi e v\, \hat{z}\, \delta(x - x_0)\delta(2\pi v u_z - \omega), \tag{3.2b}$$

and $u^2 = u_y^2 + u_z^2$. From symmetry, one may assume

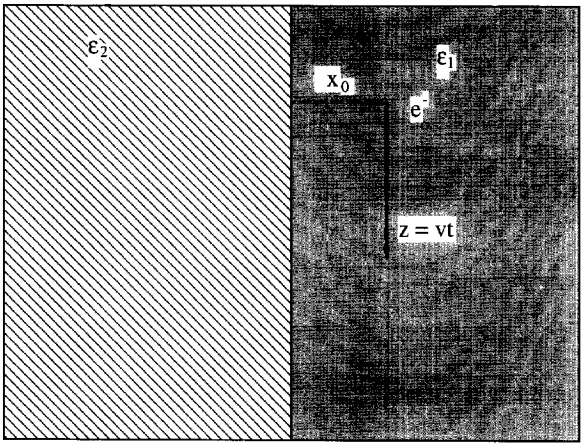

Fig. 3. Model of dielectric response theory of interface excitation for two homogeneous media. The incident electron is traveling along the z axis at a distance x_0 from the interface.

that $\prod$ has components only in the x and z axis directions: $\prod=(\prod_x, 0, \prod_z)$. The equation one needs to solve (for the case in which the beam is in medium ε_1 is

$$\left[\frac{d^2}{dx^2}-\chi_2^2\right]\bar{\prod_z}(x,u_y,u_z,\omega)=0, \tag{3.3a}$$

$$\left[\frac{d^2}{dx^2}-\chi_1^2\right]\overset{+}{\prod_z}(x,u_y,u_z,\omega) = -\frac{2\pi ev}{i\omega\varepsilon_1\varepsilon_0}\delta(x-x_0)\delta(2\pi vu_z-\omega), \tag{3.3b}$$

$$\left[\frac{d^2}{dx^2}-\chi_2^2\right]\bar{\prod_x}(x,u_y,u_z,\omega)=0, \tag{3.3c}$$

and

$$\left[\frac{d^2}{dx^2}-\chi_1^2\right]\overset{+}{\prod_x}(x,u_y,u_z,\omega)=0, \tag{3.3d}$$

where $\prod^-$ and $\prod^+$ represent the Hertz vectors for $x<0$ and $x>0$, respectively,

$$\chi_1^2=4\pi^2(u_y^2+u_z^2)-\frac{\varepsilon_1\omega^2}{c^2}, \tag{3.4a}$$

and

$$\chi_2^2=4\pi^2(u_y^2+u_z^2)-\frac{\varepsilon_2\omega^2}{c^2}. \tag{3.4b}$$

The solutions of eqn. (3.3a–d) are written as

$$\bar{\prod_z}(x,u_y,u_z,\omega)=C\exp(\chi_2 x), \tag{3.5a}$$

$$\overset{+}{\prod_z}(x,u_y,u_z,\omega)=\frac{\pi ev}{i\omega\varepsilon_1\varepsilon_0\chi_1}\delta(2\pi vu_z-\omega)\exp[-\chi_1|x-x_0|] + A\exp(-\chi_1 x), \tag{3.5b}$$

$$\bar{\prod_x}(x,u_y,u_z,\omega)=D\exp(\chi_2 x), \tag{3.5c}$$

and

$$\overset{+}{\prod_x}(x,u_y,u_z,\omega)=F\exp(-\chi_1 x). \tag{3.5d}$$

Both χ_1 and χ_2 are required to have a positive real part in all subsequent manipulations, in order that the expressions in eqn. (3.5a–d) converge at large x.

The four constants appearing in the solutions must be evaluated from the continuity of the tangential components of **E** and **H** parallel to the interface at the boundary plane defined by $x=0$. According to eqn. (2.9a) and eqn. (2.9b) the corresponding boundary conditions for the Hertz vectors at $x=0$ are

$$\varepsilon_1\overset{+}{\prod_z}=\varepsilon_2\bar{\prod_z}, \tag{3.6a}$$

$$2i\pi u_z\overset{+}{\prod_z}+\frac{d\prod_x^+}{dx}=2i\pi u_z\bar{\prod_z}+\frac{d\prod_x^-}{dx}, \tag{3.6b}$$

$$\varepsilon_1\overset{+}{\prod_x}=\varepsilon_2\bar{\prod_x}, \tag{3.6c}$$

and

$$\varepsilon_1\frac{d\prod_z^+}{dx}=\varepsilon_2\frac{d\prod_z^-}{dx}. \tag{3.6d}$$

Only the coefficients A and F are required for the following calculation,

$$A=\frac{\chi_1-\chi_2}{\chi_1+\chi_2}\zeta, \tag{3.7a}$$

and

$$F=4\pi iu_z\chi_1\zeta\frac{\varepsilon_2-\varepsilon_1}{(\chi_1+\chi_2)(\chi_2\varepsilon_1+\chi_1\varepsilon_2)}, \tag{3.7b}$$

where

$$\zeta=\frac{\pi ev}{i\omega\varepsilon_1\varepsilon_0\chi_1}\delta(2\pi vu_z-\omega)\exp[-\chi_1 x_0]. \tag{3.7c}$$

The retarding force at the electron in the $(-z)$ direction is equal to its energy loss per unit path length. From eqn. (2.14)

$$\frac{d\Delta E}{dz}=\frac{e}{2\pi}\int_{-\infty}^{\infty}d\omega\exp(-i\omega t)\int du_y\int du_z\exp[2\pi i u_z vt]\times\left\{2\pi i u_z\left[2\pi i u_z\prod_z^{+}(x,u_y,u_z,\omega)+\frac{d}{dx}\prod_x^{+}(x,u_y,u_z,\omega)\right]+\frac{\varepsilon_1\omega^2}{c^2}\prod_z^{+}(x,u_y,u_z,\omega)\right\}\Bigg|_{x=x_0}. \tag{3.8}$$

Also, the energy loss per unit path length is related to the differential excitation probability of valence electron excitations by

$$\frac{d\Delta E}{dz}=\int_0^{\infty}d\omega\,\hbar\omega\frac{d^2P}{d\omega dz}. \tag{3.9}$$

Substituting the solutions given by eqn. (3.5a–d) into eqn. (3.8), using a relation of $\varepsilon(-\omega,\mathbf{u})=\varepsilon^*(\omega,\mathbf{u})$, one has

$$\frac{d^2P}{d\omega dz}=\frac{e^2}{\pi\hbar v^2\varepsilon_0}\int_0^{\infty}du_y\,\mathrm{Im}\left\{\left[\frac{2(\varepsilon_2-\varepsilon_1)\chi_1}{\varepsilon_1(\chi_1+\chi_2)(\chi_2\varepsilon_1+\chi_1\varepsilon_2)}-\frac{[1-(v/c)^2\varepsilon_1](\chi_1-\chi_2)}{\varepsilon_1\chi_1(\chi_1+\chi_2)}\right]\exp(-2\chi_1|x_0|)-\frac{[1-(v/c)^2\varepsilon_1]}{\varepsilon_1\chi_1}\right\}, \tag{3.10a}$$

where

$$\chi_1^2=4\pi^2u_y^2+(\omega/v)^2-\frac{\varepsilon_1\omega^2}{c^2}, \tag{3.10b}$$

and

$$\chi_2^2=4\pi^2u_y^2+(\omega/v)^2-\frac{\varepsilon_2\omega^2}{c^2}. \tag{3.10c}$$

Equation (3.10a) contains the electron energy loss due to excitation of the dielectric media and to the generation of electromagnetic radiation. The integral of u_y is a sum over the contributions made by the electrons transferring momenta in different directions. In practice, the upper limit of the integral is q_c, the cut-off wave vector for plasmon excitation (Raether, 1980).

1. *Transition radiation*

The condition for producing electromagnetic radiation is examined as below. In eqn. (3.10b), if $\varepsilon_1(v/c)^2\geq1$ for some particular frequencies, χ_1 can be rewritten as

$$\chi_1=4\pi^2u_y^2-\frac{\omega^2}{c^2}[\varepsilon_1-(c/v)^2]^{1/2}. \tag{3.11}$$

Thus, χ_1 can be imaginary if $|u_y|\leq\frac{\omega}{2\pi c}[\varepsilon_1-(c/v)^2]^{1/2}$. In eqn. (3.10a), the $\exp(-2\chi_1|x_0|)$ term becomes an oscillatory function rather than an exponentially decaying one, provided energy loss $\hbar\omega\neq0$. Then, transition radiation and Cerenkov radiation can occur (Kröger, 1970). The plasmons which correspond to transition radiation are referred to as radiative plasmons; other plasmons are called non-radiative plasmons. This paper concerns the non-radiative plasmons.

2. *Non-relativistic results*

For the non-relativistic limit case $c\to\infty$, $\chi_1^2=\chi_2^2=4\pi^2u_y^2+(\omega/v)^2$, and the classical excitation probability becomes

$$\frac{d^2P}{d\omega dz}=\frac{e^2}{2\pi^2\hbar v^2\varepsilon_0}\int_0^{\infty}du_y\,\mathrm{Im}\left\{\frac{\varepsilon_2-\varepsilon_1}{\varepsilon_1(\varepsilon_1+\varepsilon_2)}\exp(-2[4\pi^2u_y^2+(\omega/v)^2]^{1/2}|x_0|)-\frac{1}{\varepsilon_1}\right\}[u_y^2+(\omega/2\pi v)^2]^{-1/2}. \tag{3.12}$$

The radiation disappears. If ε is independent of q,

$$\frac{d^2P}{d\omega dz}\approx\frac{e^2}{2\pi^2\varepsilon_0\hbar v^2}\left\{\mathrm{Im}\left\{-\frac{1}{\varepsilon_1}\right\}\ln(2\pi q_c v/\omega)+\mathrm{Im}\left\{\frac{\varepsilon_2+\varepsilon_1}{\varepsilon_1(\varepsilon_1+\varepsilon_2)}\right\}K_0(2\omega x_0/v)\right.$$
$$\left.=\frac{e^2}{2\pi^2\varepsilon_0\hbar v^2}\left\{\mathrm{Im}\left\{-\frac{1}{\varepsilon_1}\right\}\{\ln(2\pi q_c v/\omega)-K_0(2\omega x_0/v)\}+\mathrm{Im}\left\{-\frac{2}{\varepsilon_1+\varepsilon_2}\right\}K_0(2\omega x_0/v)\right\}, \tag{3.13a}$$

where K_0 is the zeroth order modified Bessel function. The first term is the volume plasmon and the second term is the interface excitation. The interface plasmon frequency is determined by $\varepsilon_1+\varepsilon_2=0$.

In comparison with the result of relativistic theory, the non-relativistic theory ignores the retardation effect and Cerenkov radiation, which occurs when $\varepsilon_r(v/c)^2\geq1$. When passing close by a dielectric medium, a charged particle suffers both surface–plasmon excitation and Cerenkov radiation. Figure 4 shows the ratio between the non-retarded and the retarded excitation probabilities for a 100 keV electron beam interacting externally with a MgO cube at different impact parameters with respect to its surface (Garcia-Molina *et al.*, 1985). It is seen that the retarded probability is always larger than the non-retarded prediction, except for beams close to the surface. This is because the classical expression neglects retardation effects, and these will be appreciable at large beam–surface distances.

The classical electron energy-loss theory is based on the particle properties of the incident electron. Strictly speaking, eqn. (3.10a) can only be applied to calculate valence-loss spectra acquired using a very fine electron probe. For an electron probe of finite size, the theory needs to be modified to convolute ($\otimes$) with the shape

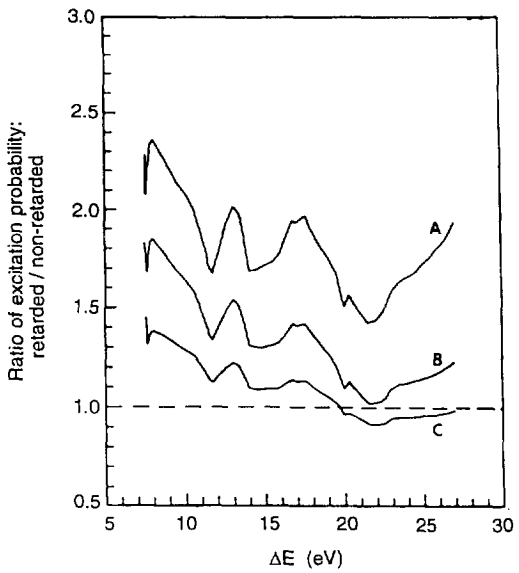

Fig. 4. Ratio between the excitation probability for a relativistic beam and a non-relativistic beam, traveling externally parallel to a MgO flat surface. The distances from the surface to the beam are A: $x_0 = 10$ nm; B: $x_0 = 4$ nm and C: $x_0 = 0.5$ nm. Beam energy 100 keV.

function I(**b**) of the electron probe (Ritchie and Howie, 1988). The scattering intensity observed for electron impact position $\mathbf{b}_p$ is

$$\frac{dP_{obs}(\mathbf{b}_p)}{d\omega} = I(\mathbf{b}_p) \otimes \frac{dP(\mathbf{b}_p)}{d\omega} = \int d\mathbf{b}\, I(\mathbf{b} - \mathbf{b}_p) \frac{dP(\mathbf{b})}{d\omega}, \tag{3.13b}$$

where $\mathbf{b} = (x,y)$. Equation (3.13b) means that the observed spectrum is an incoherent summation over the spectra calculated for different impact parameters of the incident electrons, weighted by the intensity distribution function of the electron probe. This is the result of incoherent scattering theory.

It is also important to note that the above theory is developed for high-energy electrons. For electrons of incident energy less than about 2 keV, the theoretical model breaks down (Tougaard and Kraaer, 1991).

B. *Volume plasmons in bulk materials*

The result obtained in Section 3.1 can be applied to calculate volume–plasmon excitation in a bulk material where $\varepsilon_1 = \varepsilon_2 = \varepsilon$. From eqn. (3.10a)

$$\frac{d^2P}{d\omega dz} = \frac{e^2}{\pi\hbar v^2 \varepsilon_0} \int_0^\infty du_y \, \mathrm{Im} - \frac{[1 - (v/c)^2\varepsilon]}{\varepsilon \left[4\pi^2 u_y^2 + (\omega/v)^2 - \dfrac{\varepsilon\omega^2}{c^2}\right]^{1/2}}. \tag{3.14}$$

For convenience in the following discussion, the imaginary component of the dielectric function in the term $\frac{\varepsilon\omega^2}{c^2}$ is ignored so that $\frac{\varepsilon\omega^2}{c^2} \approx \frac{\varepsilon_r\omega^2}{c^2}$. Thus, eqn. (3.14) is approximated as

$$\frac{d^2P}{d\omega dz} \approx \frac{e^2}{\pi\hbar v^2 \varepsilon_0} \int_0^\infty du_y \left\{ \mathrm{Im}\left[- \frac{1}{\left[4\pi^2 u_y^2 + (\omega/v)^2 - \dfrac{\varepsilon_r\omega^2}{c^2}\right]^{1/2}} \right] + \mathrm{Im}\left[\frac{(v/c)^2}{\left[4\pi^2 u_y^2 + (\omega/v)^2 - \dfrac{\varepsilon_r\omega^2}{c^2}\right]^{1/2}} \right] \right\} \tag{3.15}$$

The second term is zero unless $|u_y| \leq \frac{\omega}{2\pi c}[\varepsilon_r - (c/v)^2]^{1/2}$, which requires $\varepsilon_r \geq (c/v)^2$, the condition for Cerenkov radiation. Thus, part of the electron energy loss is due to Cerenkov radiation. Cerenkov radiation occurs even when the imaginary component $\varepsilon_i = 0$. The scattering angle which corresponds to the maximum intensity of Cerenkov radiation occurs at

$$[u_y]_{max} = \frac{\omega}{2\pi c}[\varepsilon_r - (c/v)^2]^{1/2}. \tag{3.16}$$

Under the non-relativistic approximation, eqn. (3.14) is approximated as

$$\frac{d^2P}{d\omega dz} = \frac{e^2}{\pi\hbar v^2 \varepsilon_0} \int_0^{u_c} du_y \frac{1}{[4\pi^2 u_y^2 + (\omega/v)^2]^{1/2}} \mathrm{Im}\left\{-\frac{1}{\varepsilon}\right\} = \frac{e^2}{4\pi^2 \varepsilon_0 \hbar v^2} \mathrm{Im}\left\{-\frac{1}{\varepsilon}\right\} \ln[1 + (2\pi u_c v/\omega)^2], \tag{3.17}$$

where $\mathrm{Im}\{-\frac{1}{\varepsilon}\} = \frac{\varepsilon_i}{\varepsilon_r^2 + \varepsilon_i^2}$ is known as the energy-loss function for volume excitation.

1. *Free-electron-gas model*

The characteristic shape of valence-loss spectra can be illustrated using the quasi-free-electron model. In an electron gas with electron density n, the dielectric response function is given by eqn. (3.18) if the dissipative effects are considered:

$$\varepsilon(\omega) = 1 - \frac{\omega_p^2}{\omega(\omega + i/\tau)} \tag{3.18}$$

with

$$\varepsilon_r(\omega) = 1 - \frac{\omega_p^2}{\omega^2 + 1/\tau^2} \text{ and } \varepsilon_i(\omega) = \frac{\omega_p^2}{\omega\tau(\omega^2 + 1/\tau^2)}, \tag{3.19}$$

where τ is the relaxation time, ω_p the frequency of the bulk plasmon, and $\omega_p^2 = \frac{ne^2}{\varepsilon_0 m}$. Thus the energy-loss function is

$$\mathrm{Im}\left\{-\frac{1}{\varepsilon}\right\} = \frac{\omega_p^2 \omega/\tau}{(\omega^2 - \omega_p^2)^2 + \omega^2/\tau^2}. \tag{3.20}$$

Figure 5 shows a schematic plot of $\varepsilon_r(\omega)$, $\varepsilon_i(\omega)$ and $\mathrm{Im}\{-\frac{1}{\varepsilon}\}$. The volume plasmon loss corresponds to a sharp peak centered at $\omega = \omega_p$. The full-width at half-

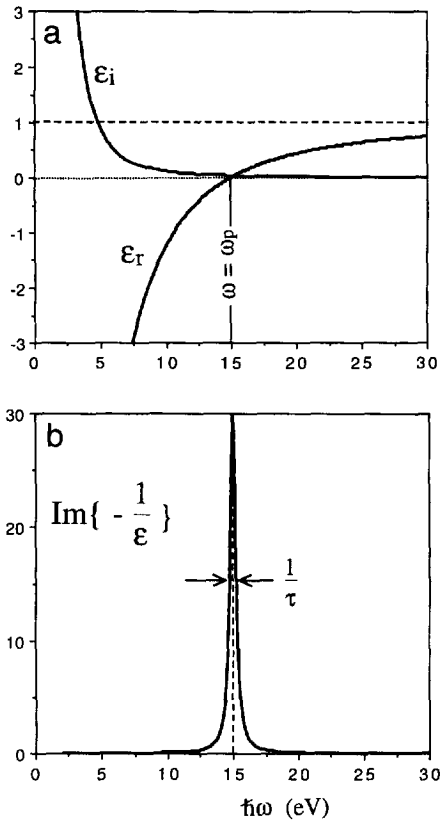

Fig. 5. (a) Plot of real and imaginary components of the dielectric function for Al based on the quasi-free-electron gas model. (b) The calculated volume plasmon energy-loss function.

maximum (FWHM) of the plasmon peak is $1/\tau$. Aluminum is a typical example of the free-electron case with $\hbar\omega_p = 15$ eV, $\hbar/\tau = 0.5$ eV and $[\mathrm{Im}(-1/\varepsilon)]_{max} = 30$. The volume plasmon energies for conventional metals have been tabulated by Egerton (1986) and Raether (1980). Fig. 5 shows the calculated dielectric functions and the corresponding energy-loss function of Al, based on the quasi-free-electron gas model. The volume plasmon is represented by a sharp peak.

Figure 6 shows EELS spectra acquired from Al and TiH specimens. The volume plasmons of Al and TiH are

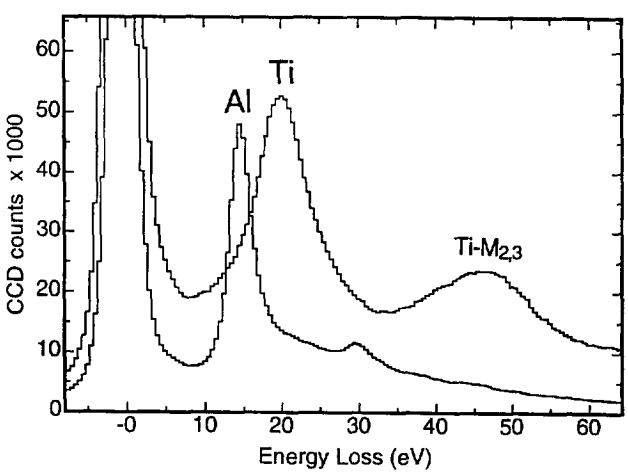

Fig. 6. Plasmon-loss spectra acquired from thin foil Al and TiH, respectively, showing the dependence of the volume plasmon frequency on the density of the valence electrons in the solid. The Ti–$M_{2,3}$ edge is due to the excitation of 3p electrons of Ti. Beam energy 300 keV.

located at 15 and 21 eV, respectively. The difference in volume plasmon energies is due mainly to the difference in valence electron density. The TiH plasmon has at higher energy because of the higher density of valence electrons in TiH. The FWHMs of the two peaks are different, indicating the difference in decay time. The Al plasmon peak is significantly lower and sharper than the TiH plasmon peak. In comparison to the calculated peak shown in Fig. 5b, the width of the Al peak is broadened by the energy spread of the electron source, which is 1.5 eV for this case. The dependence of plasmon energy on the density of free electrons has been used to quantitatively map Li distribution in an Al–Li alloy (Hunt, 1991).

In an assembly involving quasi-free-electrons of density n_f and bound electrons of density n_b with an eigenfrequency ω_n, the dielectric function is written as

$$\varepsilon(\omega) = 1 - \frac{n_f e^2}{\varepsilon_0 m}\cdot\frac{1}{\omega(\omega + i/\tau)} + \frac{n_b e^2}{\varepsilon_0 m}\cdot\frac{1}{\omega_n^2 - \omega^2 + i\omega/\tau}. \tag{3.21}$$

2. *Kramers–Kronig transformation and measurement of dielectric function*

From the valence-loss spectra, the energy-loss function $\mathrm{Im}[-1/\varepsilon]$ can be directly obtained if the multiple plasmon scattering effects are eliminated. This information allows a calculation of the real part $\mathrm{Re}[-1/\varepsilon]$ according to the Kramers–Kronig relation (Johnson, 1975; Colliex, 1984)

$$\mathrm{Re}\left\{\frac{1}{\varepsilon(\omega,\mathbf{q})}\right\} = 1 - \frac{2}{\pi}\mathrm{PP}\int_0^\infty \mathrm{d}\omega' \mathrm{Im}\left\{-\frac{1}{\varepsilon(\omega',\mathbf{q})}\right\}\frac{\omega'}{\omega'^2 - \omega^2}, \tag{3.22a}$$

where PP represents the principal part of the integral. The measured dielectric function is normalized according to the Kramers–Kronig (K–K) sum rule (Egerton, 1986):

$$1 - \mathrm{Re}\left\{\frac{1}{\varepsilon(0,\mathbf{q})}\right\} = -\frac{2}{\pi}\int_0^\infty \mathrm{d}\omega\ \mathrm{Im}\left\{\frac{1}{\varepsilon(\omega,\mathbf{q})}\right\}\frac{1}{\omega}. \tag{3.22b}$$

ε_r and ε_i can be calculated from $\mathrm{Re}[-1/\varepsilon(\omega)]$ and $\mathrm{Im}[-1/\varepsilon(\omega)]$

$$\varepsilon_r = \frac{\mathrm{Re}(1/\varepsilon)}{[\mathrm{Re}(1/\varepsilon)]^2 + [\mathrm{Im}(1/\varepsilon)]^2}, \tag{3.22c}$$

and

$$\varepsilon_i = -\frac{\mathrm{Im}(1/\varepsilon)}{[\mathrm{Re}(1/\varepsilon)]^2 + [\mathrm{Im}(1/\varepsilon)]^2}. \tag{3.22d}$$

The K–K transformation is a powerful technique which can be applied to determine the dielectric response function from an energy-loss spectrum acquired from a region smaller than a few nm in TEM and STEM. This is a unique advantage, particularly in the

cases where chemical non-stoichiometry is significant. It must be pointed out that the K–K transform holds only for isotropic materials. The K–K transform has been applied to determine the dielectric response functions of a high temperature superconductor (Wang *et al.*, 1991, 1993a,b,c; Lin *et al.*, 1993; Wang and Ritter, 1991). The fine peaks observed in the low-loss region reveal transitions from the valence states and the integrated intensity of the peak is approximately related to the occupation number of valence electrons in the state, which can be applied to determine the location of the excitation in crystal lattices, provided a standard spectrum from a specimen with known excitation is available. This study can reveal the structure of valence bands. The perovskite-like structures of functional materials usually exhibit anisotropic dielectric properties, and EELS is ideally suited for this orientation-dependent dielectric function measurement (Wang *et al.*, 1993b; Zhang *et al.*, 1993). Factors which may affect the measurement of the dielectric function of a thin specimen using EELS have been outlined by Yuan (1989). The K–K transformation has been applied to measure the dielectric function of carbon nanotubes (Kuzuo *et al.*, 1992), but no correction was made for the geometry of the carbon tube, which, as will be shown in Section VIII, affects the spectrum shape. For small particles, the spectrum shape is dominated by surface excitation, thus a large error could be introduced if either the medium configuration or the excitation condition (such as the impact parameter/position) is ignored. The most reliable condition for measurement of dielectric function is using homogeneous thin foils.

Two more sum rules also apply to the dielectric function (Egerton, 1986):

$$\int d\omega\, \omega\, \mathrm{Im}[-1/\varepsilon(\omega)] = \frac{\pi}{2}\omega_p^2; \tag{3.23a}$$

and

$$\int d\omega\, \omega\, \mathrm{Im}\{-2/[1+\varepsilon(\omega)]\} = \frac{\pi}{4}\omega_p^2. \tag{3.23b}$$

3. *Momentum-resolved EELS*

An alternative derivation of eqn. (3.17) was given from the Fourier transform of Poisson's equation (Ritchie, 1957); the differential probability of an electron inelastically scattered to momentum $\hbar\mathbf{q}$ [see eqn. (12.23) in a later section] in an infinite large isotromic medium characterized by a $\mathbf{q}$-dependent dielectric function $\varepsilon(\omega,\mathbf{q})$ is

$$\frac{d^3P}{d\omega dz d\mathbf{q}} = \frac{e^2}{2\pi^2\hbar\varepsilon_0 v^2}\frac{1}{[q^2+(\omega/v)^2]}\mathrm{Im}\left\{-\frac{1}{\varepsilon(\omega,\mathbf{q})}\right\}, \tag{3.24a}$$

which can be expressed as a function of the scattering angle defined by $q = K\theta$ and $\theta_E(\omega) = \frac{\omega}{Kv}$,

$$\frac{d^3P}{d\omega dz d\theta} = \frac{e^2}{2\pi^2\hbar\varepsilon_0 v^2}\frac{\theta}{[\theta^2+\theta_E^2]}\mathrm{Im}\left\{-\frac{1}{\varepsilon(\omega,q)}\right\}, \tag{3.24b}$$

where K is the wave vector of the incident electron. eqn. (3.24b) clearly indicates that energy-loss spectra acquired at different scattering angles can be applied to calculate the momentum-dependent energy-loss function $\mathrm{Im}\left\{-\frac{1}{\varepsilon(\omega,q)}\right\}$. This experiment can be conducted by positioning the entrance aperture of the EELS spectrometer at different scattering angles with respect to the central transmitted beam, provided the size of the aperture is sufficiently small that it allows the momentum-resolved information be retrieved (Batson and Silcox, 1983). This is the so-called momentum-resolved (or angular-resolved) EELS. If the semi-collection angle of the spectrometer is much larger than the inelastic characteristic angle θ_E, the momentum transfer $\hbar\mathbf{q}$ is approximately confined in a plane perpendicular to the incident beam. If the incident beam direction is along the **c** axis of the crystal, **q** would be parallel to the **a**–**b** plane. By varying the crystal orientation with respect to the incident beam direction, the momentum-resolved EELS allows measurement of the dispersive dielectric function $\varepsilon(\omega,\mathbf{q})$ (Zhang *et al.*, 1993; Wang *et al.*, 1993a) because the K–K transform holds for a $\mathbf{q}$-dependent $\varepsilon(\omega,\mathbf{q})$ (Mahan, 1990).

C. *Surface excitation of thin foils in TEM*

For the excitation of thin foils, only the excitation of the surface (interface) that is parallel to the incident beam was considered. For thin films in the transmission electron case, the excitation of the top and bottom surfaces also contribute to the valence spectra, particular when the specimen is thin. For a simple case of a thin slab of thickness d_0 and dielectric function ε with the incident beam perpendicular to the slab surface, the valence electron excitation probability is given by (Ritchie, 1957)

$$\frac{dP(x)}{d\omega} = \frac{e^2}{2\pi^2\varepsilon_0\hbar v^2}\int_0^{2\pi q_c} du\, \frac{u^2}{[u^2+(\omega/v)^2]^2} \times \mathrm{Im}\left\{-\frac{1-\varepsilon}{\varepsilon}\right.$$
$$\left.\cdot\frac{2(\varepsilon-1)\cos(\omega d_0/v)+(\varepsilon-1)^2\exp(-ud_0)+(1-\varepsilon^2)\exp(ud_0}{(\varepsilon-1)^2\exp(-ud_0)-(\varepsilon+1)^2\exp(ud_0)}\right\}$$
$$+\frac{e^2 d_0}{2\pi^2\hbar\varepsilon_0 v^2}\int_0^{2\pi q_c} du\, \frac{u}{u^2+(\omega/v)^2}\mathrm{Im}\left\{-\frac{1}{\varepsilon}\right\}, \tag{3.25}$$

where the first term corresponds to surface excitation and the second term to volume excitation. An extensive theory which includes spatial dispersion has been given by Gumbs and Horing (1991). In a general case, the direction of the incident electron may not be perpendicular to the foil surface. For oblique incidence, the valence electron excitation probability has been given by several authors (Otto, 1967; Kröger, 1970; Geiger, 1967).

From eqn. (3.25), the resonance frequencies for surface excitations are determined by

$$\frac{\varepsilon-1}{\varepsilon+1}=\pm\exp(ud_0). \qquad ()$$

For free-electron metals, the dispersion relationships of the surface excitation are given by

$$\omega_s^2=\frac{\omega_p^2}{2}[1\pm\exp(-ud_0)]. \qquad (3.27)$$

If the specimen is sufficiently thick so that the coupling between the top and bottom surfaces is weak, eqn. (3.25) is approximated as

$$\begin{aligned}\frac{dP(x)}{d\omega}&=\frac{e^2}{2\pi^2\varepsilon_0\hbar v^2}\int_0^{2\pi q_c}dq_y\frac{q^2}{[q^2+(\omega/v)^2]^2}\mathrm{Im}\left\{\frac{1}{\varepsilon}-\frac{4}{\varepsilon+1}\right\}\\&+\frac{e^2d_0}{2\pi^2\hbar\varepsilon_0v^2}\int_0^{2\pi q_c}du\,\frac{u}{u^2+(\omega/v)^2}\mathrm{Im}\left\{-\frac{1}{\varepsilon}\right\}\\&\approx\frac{e^2}{4\pi^2\varepsilon_0\hbar v^2}\left[\mathrm{arctg}(2\pi q_cv/\omega)\mathrm{Im}\left\{\frac{1}{\varepsilon}-\frac{4}{\varepsilon+1}\right\}\right.\\&\left.+\ln(1+(2\pi q_cv/\omega)^2)\mathrm{Im}\left\{-\frac{1}{e}\right\}\right],\end{aligned} \qquad (3.28)$$

which contains the contributions made by both the surface and volume plasmons. Figure 7 shows plots of the theoretical volume and surface energy-loss functions of Fe. The surface-loss peak is located at lower energies. The experimentally observed spectrum is a superposition of the surface-loss and the volume-loss. For thin films of known thickness, the surface-plasmon spectrum, although small, can be separated from the volume plasmon spectrum using a method introduced by Evans and Wang (1992).

Plasmon loss represents charge oscillation in a thin film. Polarization fields are excited in the medium when the charged particle approaches it. For a thin slab, two characteristic plasmon modes are excited: $\omega_a\approx\omega_p/\sqrt{2}$ for $ud_0>>1$ and $\omega_b\approx\omega_p\sqrt{ud_0}/\sqrt{2}$ for $ud_0\ll1$. Figure 8 represents schematically the a and b modes of surface polarization electric fields within a thin slab. Mode a is strongly associated with the charge oscillation at each surface. Mode b is largely determined by the coupling between the top and bottom surfaces. The excitation probability of mode b is determined by the thickness of the foil. For thick foils and $ud_0>>1$, mode a is dominant; for thin foils and $ud_0<1$, mode b is dominant.

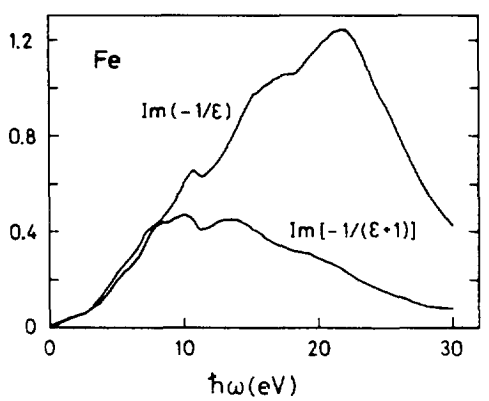

Fig. 7. Plot of volume and surface plasmon loss functions of Fe.

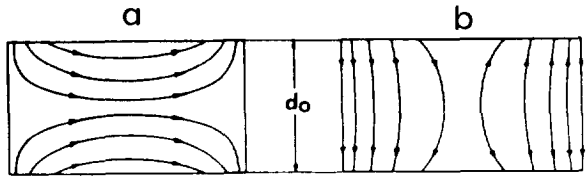

Fig. 8. A physical representation of the surface polarization electric fields within a thin free-electron slab for the two plasmon modes.

D. *Surface excitation in reflection electron microscopy and STEM*

To illustrate the application of eqn. (3.13a), a simple case shown in Fig. 3 is considered. If the electron is moving in vacuum parallel to the surface, i.e. $\varepsilon_1=1$ and $\varepsilon_2=\varepsilon$, eqn. (3.13a) reduces to

$$\frac{d^2P(x_0)}{dzd\omega}=\frac{e^2}{2\pi^2\varepsilon_0\hbar v^2}\mathrm{Im}\left\{-\frac{2}{\varepsilon+1}\right\}K_0(2\omega x_0/v). \qquad (3.29)$$

$\mathrm{Im}\{-2/\varepsilon+1\}$ is called the surface energy-loss function. No volume plasmon would be excited in this case. Valence-electron excitation is an unlocalized scattering process, which occurs even when the electron is a few nm away from the surface in vacuum. If the electron penetrates into the crystal, i.e. $\varepsilon_2=1$ and $\varepsilon_1=\varepsilon$, eqn. (3.13a) reduces to (Howie, 1983, 1988; Howie and Milne, 1984):

$$\begin{aligned}\frac{d^2P(x_0)}{dzd\omega}&=\frac{e^2}{2\pi^2\varepsilon_0\hbar v^2}\left\{\mathrm{Im}\left(-\frac{1}{\varepsilon}\right)[\ln(2\pi q_cv/\omega)\right.\\&\left.-K_0(2\omega x_0/v)]+\mathrm{Im}\left\{-\frac{2}{\varepsilon+1}\right\}K_0(2\omega x_0/v)\right.\end{aligned} \qquad (3.30)$$

The $\mathrm{Im}(-\frac{1}{\varepsilon})$ term describes the excitation of the volume plasmon and depends on the distance of the electron from the surface; the second term characterizes the excitation of the surface plasmon. The decrease of the volume excitation as the electron approaches the surface compensates the increase of the surface excitation. The excitation probability of the volume plasmon drops to zero at $x_0=0$.

From eqn. (3.30), the volume plasmon and surface plasmon of metals can be given below. For simplicity, one uses the free-electron model. The resonance excitation of the volume occurs at $\varepsilon(\omega)=0$, thus, ω_p is the volume plasmon frequency. The surface resonance excitation occurs at $\varepsilon(\omega)+1=0$, thus $\omega_s=\omega_p/\sqrt{2}$.

1. *Effect of dielectric spatial dispersion*

In eqn. (3.30), the Bessel function $K_0(2\omega x_0/v)$ tends to infinity at $x_0=0$. This non-physical result was artificially introduced from two sources. One source is the

assumption of $\varepsilon(\omega)$ being independent of q, i.e. no dispersion (Zabala and Echenique, 1990). The other source is the unlimited momentum transfer. For valence-electron excitation, there is a cut-off at $q = q_c$, so the upper limit of u_y integration in eqn. (3.15) should be replaced by q_c.

The dispersion of the dielectric function has enormous effect on the image potential experienced by a point charge as it approaches the surface. Figure 9 shows a comparison of the image potential at a metal surface calculated with and without consideration of the dielectric dispersion (Echenique *et al.*, 1981). The difference in the results increases as the impact parameter from the surface decreases. The divergence of the potential at the surface disappears when the dispersion of the dielectric function is included. Also, the potential at the surface is substantially low, in correspondence to the practical situation. The inclusion of dispersion is essential in determination of the angular dependence of electron energy-loss spectra (Barrachina and Gras-Marti, 1992).

Figure 10 shows the calculated differential excitation probabilities per unit distance for an electron traveling parallel with a GaAs(110) surface. The dashed and solid lines represent the excitation probabilities of the volume and surface plasmons inside the crystal, respectively. The dotted line is the total probability of the plasmon excitations (surface and volume). The excitation probabilities of the surface and volume plasmons sensitively depend on the impact parameter of the electron from the surface, but the total excitation probability is almost a constant (for $x < 0$). The excitation of the volume plasmon occurs only when the electron penetrates deep into the crystal. The excitation of the surface plasmon happens in a region about 1.5 nm from the surface. Only the surface plasmon is excited if the electron is outside of the crystal. The electron–surface interaction is a long range Coulomb interaction.

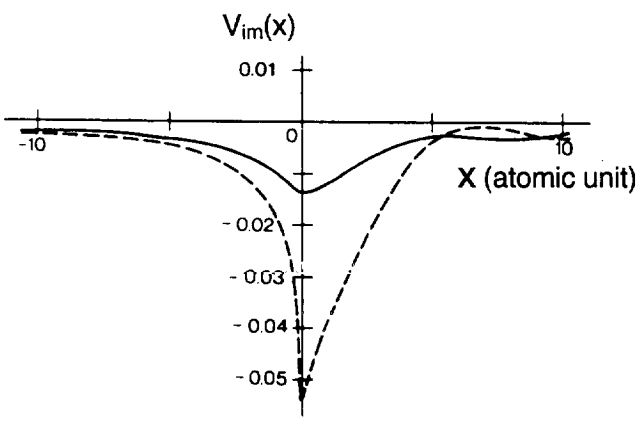

Fig. 9. Variation of the image potential experienced by a point charge when it penetrate from the vacuum ($x > 0$) into the metal ($x < 0$). The solid and dashed lines are the calculations with and without including dispersion. The unphysical divergence of the potential at the surface is absent when the dispersion relation is included. 1 atomic unit = 0.053 nm.

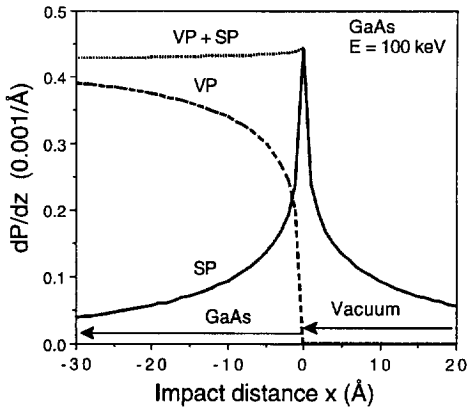

Fig. 10. Calculated excitation probability per unit distance across a GaAs surface as a function of the electron impact parameter x from the surface. With $x < 0$ inside GaAs crystal and $x > 0$ in vacuum. Electron energy is 100 keV.

2. *Quantifying surface excitation spectra*

The fine electron probe in STEM is ideally suited for observation of surface excitation. For cubic MgO crystals, for example, the electron probe can be directly positioned on an MgO crystal, at the surface and outside the surface (Cowley, 1982). Thus, the electron energy-loss spectra can be acquired as a function of the electron impact parameter (Batson, 1983). Figure 11a and Fig. 11b show the calculated valence-loss spectra (dashed lines) and the experimentally observed spectra (solid lines) of an MgO cube. The spectra were calculated using dielectric response theory as outlined in Section 3.1. The volume excitation is dominant if the electron probe directly penetrates the cube (Fig. 11a). The dielectric function of MgO is retrieved from the volume excitation data according to the K–K transform; the results were applied to calculate the spectrum shape when the electron probe is outside the MgO cube, in which only the surface excitation occurs (Fig. 11b). The calculated spectra not only show the major features of the spectra but also exhibit the same absolute scattering probability in reference to the observed data (Walls and Howie, 1989). This is a direct proof of the success of dielectric response theory for valence electron excitations.

In reflection electron microscopy (REM) (Wang, 1993, 1996), the simplest scattering geometry is the mirror-reflection model in which the electron is reflected from the surface without any penetration, thus there is no diffraction effect. This is similar to the reflection of light from a planar mirror surface. Equation (3.29) and eqn. (3.30) can be applied to simulate EELS spectra acquired in REM geometry by modifying the scattering trajectory of the electron as a staircase (Fig. 12), the distance of the electrons from the surface is represented by a mean value for each step, which is approximately valid if the step size is chosen to be small. The path length of the electron within each segment is $\Delta x/\sin\theta$. This has been demonstrated as an effective experimental method for measuring electron penetration depth into the surface (Wang, 1993).

According to eqn. (3.30), only surface excitations

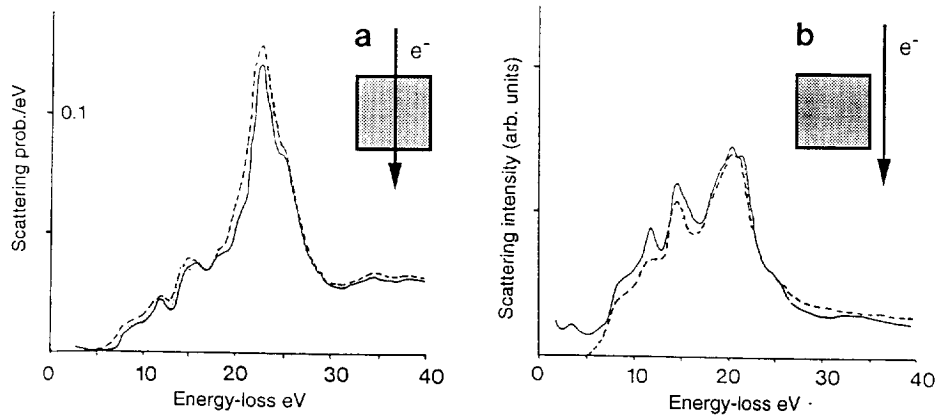

Fig. 11. (a) Volume and (b) surface excitation spectra acquired at 100 kV from a MgO cube of thickness about 120 nm. The dashed lines are the simulated spectra based on dielectric response theory presented in Section 3.1 (Walls and Howie, 1989).

occur in REM geometry when the electron is traveling in vacuum. In the mirror reflection model, surface excitation occurs when the electron approaches and leaves the surface. The probability of excitations in this scattering geometry is calculated as

$$\bar{m}_0 = 2\int_0^\infty \frac{dx_0}{\sin\theta}\int_0^\infty d\omega \frac{d^2P(x_0)}{dz d\omega} = \frac{e^2}{4\pi\varepsilon_0\hbar v\sin\theta}\int_0^\infty d\omega \frac{1}{\omega}\mathrm{Im}\left\{\frac{-2}{\varepsilon+1}\right\}. \tag{3.31}$$

E. *Transverse force on a moving electron*

The theories presented in Section 2.2 assume that the incident electron trajectory is unaffected by the energy-loss. In addition to the reduction of the electron velocity due to energy loss, the induced charges attract the electron towards the interface, resulting in a deflection of the incident beam direction. In this section, the transverse force F_x, perpendicular to the direction of electron travel, is calculated for the dielectric configuration shown in Fig. 3. The transverse force is produced by the electric field E_x of the induced charges; from eqn. (2.9a):

$$\begin{aligned}
F_x &= (-e)\tilde{E}_{ix}(\mathbf{r},t)|_{\mathbf{r}=\mathbf{r}_0(t)} \\
&= -\frac{e}{2\pi}\int_{-\infty}^{\infty} d\omega \exp(-i\omega z/v)E_{ix}(\mathbf{r},\omega)|_{\mathbf{r}=\mathbf{r}_0} \\
&= -\frac{e}{2\pi}\int_{-\infty}^{\infty} d\omega \exp(-i\omega z/v)\left[\frac{\partial}{\partial x}\left(\nabla\cdot\tilde{\prod}_i^+(\mathbf{r},\omega)\right)\right. \\
&\quad \left.+\frac{\varepsilon_1\omega^2}{c^2}\tilde{\prod}_{ix}^+(\mathbf{r},\omega)\right]|_{\mathbf{r}=\mathbf{r}_0} \\
&= -\frac{e}{2\pi}\int_{-\infty}^{\infty} d\omega \exp(-i\omega z/v)\int du_y\int du_z \exp[2\pi i u_z z] \\
&\quad \times\left\{2\pi i u_z\frac{d}{dx}\prod_{iz}^+(x,u_y,u_z,\omega)+\frac{d^2}{dx^2}\prod_{ix}^+(x,u_y,u_z,\omega)\right. \\
&\quad \left.+\frac{\varepsilon_1\omega^2}{c^2}\prod_{iz}^+(x,u_y,u_z,\omega)\right\}\Big|_{x=x_0} \\
&= -\frac{e^2}{\pi v\varepsilon_0}\int_0^\infty d\omega\int_0^\infty du_y \mathrm{Re}\left\{\left[\chi_2-\chi_1\right.\right. \\
&\quad \left.\left.+\frac{2(\varepsilon_2-\varepsilon_1)(4\pi^2u_y^2+(\omega/v)^2)}{\chi_2\varepsilon_1+\chi_1\varepsilon_2}\right]\frac{\exp(-2\chi_1|x_0|)}{\varepsilon_1(\chi_1+\chi_2)}\right\}.
\end{aligned} \tag{3.32}$$

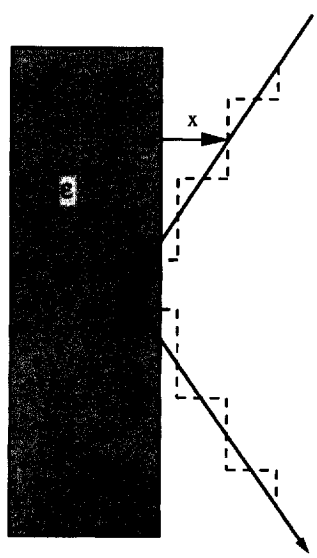

Fig. 12. Stair-type electron traveling trajectory for simulating EELS spectra acquired in RHEED geometry. The dashed line indicates the approximated electron trajectory for theoretical calculations. The electron is consider to travel parallel to the surface within each stair step.

Taking limit $c\to\infty$, corresponding to a non-relativistic electron,

$$F_x = -\frac{e^2}{\pi v\varepsilon_0}\int_0^\infty d\omega\int_0^\infty du_y \mathrm{Re}\left\{\frac{(\varepsilon_2-\varepsilon_1)}{\varepsilon_1(\varepsilon_1+\varepsilon_2)}\right\} \exp[-2(4\pi^2u_y^2+(\omega/v)^2)^{1/2}|x_0|]. \tag{3.33}$$

Thus, $F_x<0$ and the electron is attracted towards the interface (Echenique and Howie, 1985; Marks, 1982), as observed experimentally (Cowley and Wang, 1986).

IV. VALENCE-LOSS SPECTRA OF LAYERED MATERIALS

Multilayered materials are composed of layers of different compounds. The thickness of each layer can be made so small that the one-dimensional quantum effect is expected. This type of material exhibits unique properties and has potential applications in advanced technologies. The plasmon oscillations in these materials are strongly affected by the coupling between interfaces. Figure 13 shows valence-loss spectra acquired from an Al foil coated with Al_2O_3 of different thicknesses (Raether, 1967). For an extremely thin coating case (spectrum 1), the surface plasmon is located at an energy approximately determined by $\omega_p/\sqrt{2}$, the surface plasmon of a clean Al surface. With the increase in thickness of the Al_2O_3 coating, the surface plasmon energy decreases significantly because the excitation of the Al–Al_2O_3 interface becomes dominant. This is an example of the sensitivity of the plasmon-oscillation frequency to the dielectric configuration of the media.

There are two methods used to examine the characteristics of valence-electron excitation in layered materials: the incident beam is either perpendicular to or parallel to the layers, as shown in Fig. 14. In this section, a simple case is considered: two media (of dielectric functions ε and ε'') with a sandwich layer (dielectric function ε') of thickness $2h$ between them, as shown in Fig. 14a. The excitation probability of the valence electrons is given by eqn. (4.1a) if the electron is located at a distance x ($x > h$) from the center of the sandwich layer in medium ε'' and moving parallel to the interface (Howie and Milne, 1985).

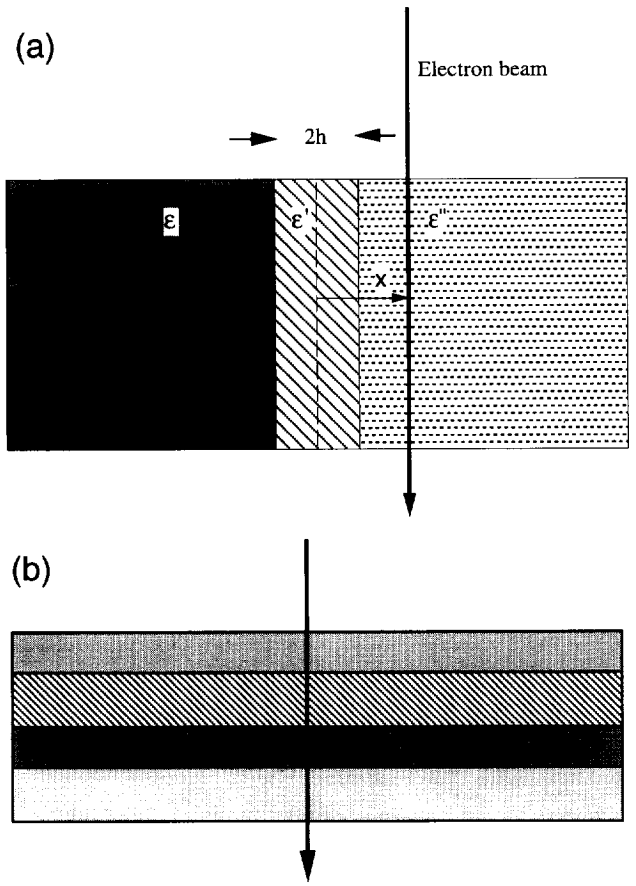

Fig. 14. (a) Excitation of a 'sandwich' layer by an electron beam which is traveling parallel to the interface. (b) Excitation of a multilayered material when the incident electron direction is perpendicular to the layers.

$$\frac{d^2P(x)}{d\omega dz} = \frac{e^2}{2\pi^2\varepsilon_0\hbar v^2}\int_0^{2\pi q_c} dq_y \frac{1}{q}\left\{\mathrm{Im}\left(-\frac{1}{\varepsilon''}\right) + F(\varepsilon,\varepsilon',\varepsilon'',q,h)\exp[-2q|x-a|]\right\}, \tag{4.1a}$$

where $q^2 = q_y^2 + \omega^2/v^2$, and

$$F = \mathrm{Im}\left\{\frac{[(\varepsilon'+\varepsilon)(\varepsilon'-\varepsilon'')\exp(2qh) - (\varepsilon'-\varepsilon)(\varepsilon'+\varepsilon'')\exp(-2qh)]}{\varepsilon''[(\varepsilon'+\varepsilon)(\varepsilon'+\varepsilon'')\exp(2qh) - (\varepsilon'-\varepsilon)(\varepsilon'-\varepsilon'')\exp(-2qh)]}\right\}. \tag{4.1b}$$

These equations are useful for simulating the EELS spectra acquired in REM geometry from a surface if there is a thin layer of another phase (Wang, 1991).

In the case where the incident electron is moving perpendicular to the interface, as shown in Fig. 14b, Bah *et al.* (1992) and Richter and Geiger (1981) have given comprehensive reviews of dielectric response theory in the layered materials. The anisotropy property of the dielectric medium was also considered. For layered metal films, Economou (1969) and Bolton and Chen (1995) gave a detailed description about the dispersion relations of the system.

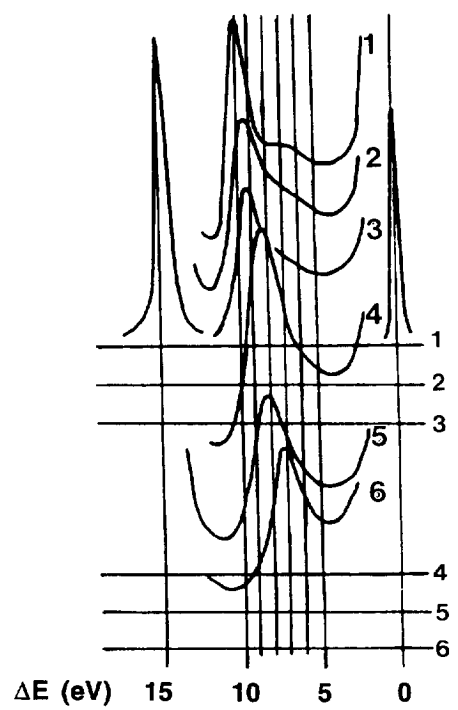

Fig. 13. EELS spectra from an Al foil coated with Al_2O_3 of different thicknesses.

V. VALENCE-LOSS SPECTRA OF SPHERICAL PARTICLES

A. *Single-particle or cavity model*

The theoretical scheme used to solve Maxwell's equations for the electromagnetic fields in the spherical geometry was described in detail by Stratton (1941) and Born and Wolf (1980). The solutions are too lengthy and complex to be presented here. For simplicity, one makes the non-relativistic approximation, under which the surface excitation of a sphere embedded in a large medium can be solved exactly (Ferrell *et al.*, 1987; Ferrell and Echenique, 1985; Echenique *et al.*, 1987b). A quantum mechanical treatment of plasmon excitation in a metal sphere has been given by Schmeits (1981) and Ashley and Ferrell (1976).

Consider a point electron moving at a constant velocity $\mathbf{v}$ in medium ε_1 along a trajectory specified by $\mathbf{r}_0(t)=(x_0,0,vt)$, as schematically shown in Fig. 15. If $v \ll c$, the potential generated by this moving charge is the solution of Poisson's equation. In terms of spherical coordinates (r,θ,ϕ), one has $r_0=(x_0^2+v^2t^2)^{1/2}$ and cos $\theta_0=vt/r_0$. The potential due to the incident electron in free-space for $r_0>r$ is

$$\tilde{V}_e(\mathbf{r},t) = -\frac{e}{4\pi\varepsilon_0|\mathbf{r}-\mathbf{r}_0(t)|} = -\frac{e}{4\pi\varepsilon_0 r_0}\sum_{L=0}^{\infty}\sum_{m=0}^{L} N_{Lm}(r/r_0)^L P_{Lm}(\cos\theta)P_{Lm}(\cos\theta_0)\cos(m\phi), \tag{5.1a}$$

where P_{Lm} is the associated Legendre function. Also,

$$N_{Lm}=\frac{(2-\delta_{0m})(L-m)!}{(L+m)!}, \tag{5.1b}$$

where δ_{0m} is unity if $m=0$ and is zero otherwise. If $r>r_0$, then r and r_0 are exchanged in eqn. (5.1a). If one uses spatially local, frequency-dependent, complex, dielectric functions to characterize the response of the media, it is necessary to introduce the Fourier transform to match boundary conditions. Consider a sphere of radius $a<x_0$ centered at the origin and having complex dielectric function ε_2. If $V_e(\mathbf{r},\omega)$ is the Fourier transform of $\tilde{V}_e(\mathbf{r},t)$ due to the incident electron, then the potential outside the sphere has Fourier transform

$$V_{out}(\mathbf{r},\omega)=\frac{V_e(\mathbf{r},\omega}{\varepsilon_1} + \sum_{L=0}^{\infty}\sum_{m=0}^{L} A_{Lm}(2-\delta_{0m})(a/r)^{L+1}P_{Lm}(\cos\theta)\cos(m\phi), \tag{5.2}$$

and inside the sphere the Fourier transform of the potential is

$$V_{in}(\mathbf{r},\omega)=\sum_{L=0}^{\infty}\sum_{m=0}^{L} B_{Lm}(2-\delta_{0m})(r/a)^L P_{Lm}(\cos\theta)\cos(m\phi). \tag{5.3}$$

Frequency-dependent coefficients A_{Lm} and B_{Lm} are determined by matching the solution at the boundary $r=a$. The homogeneous potential outside the sphere is responsible for producing the energy loss, which is

$$V_{out}^{(i)}(\mathbf{r},\omega)=\frac{e}{4\pi\varepsilon_0}\sum_{L=1}^{\infty}\sum_{m=0}^{L} N_{Lm}a^L[a_L(\omega)+\gamma_L(\omega)] (a/r)^{L+1}P_{Lm}(\cos\theta)\cos(m\phi)I_{Lm}(\omega,x_0), \tag{5.4a}$$

where

$$\alpha_L(\omega)=\frac{L\varepsilon_2(\omega)+(L+1)\varepsilon_1(\omega)-(2L+1)}{L\varepsilon_2(\omega)+\varepsilon_1(\omega)(L+1)}; \tag{5.4b}$$

$$\gamma_L(\omega)=\left[-1+\frac{1}{\varepsilon_1(\omega)}\right], \tag{5.4c}$$

I_{Lm} is given by

$$I_{Lm}(\omega,x_0)=\int_{-\infty}^{\infty} dt\, r_0^{-(L+1)}P_{Lm}(\cos\theta_0)\exp(i\omega t) = \frac{2i^{L-m}|\omega/v|^L K_m(|\omega x_0/v|)}{v(L-m)!}(\omega/|\omega|)^{L-m}, \tag{5.4d}$$

where K_m is the modified Bessel function of order m. The $\gamma_L(\omega)$ term characterizes reduction of the volume plasmon due to the presence of the surface plasmon, which is neglected henceforth as far as surface-plasmon

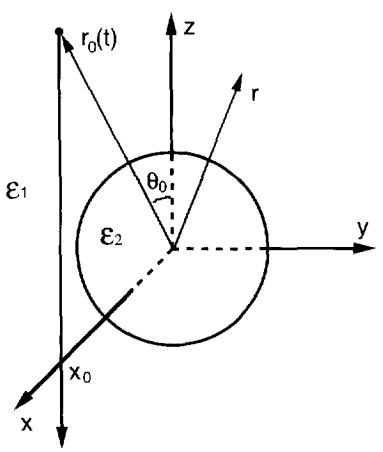

Fig. 15. A schematic model showing the excitation of a sphere embedded in a large medium by an external electron beam.

excitation is concerned. The electron energy loss due to surface-plasmon excitation is calculated by

$$\frac{d\Delta E}{dz} = -e\frac{\partial}{\partial z}\tilde{V}^{(i)}_{out}(\mathbf{r},t)|_{\mathbf{r}=\mathbf{r}_0(t)} = \frac{e^2}{8\pi^2\varepsilon_0}\sum_{L=1}^{\infty}\sum_{m=0}^{L} \int_{-\infty}^{\infty} d\omega \exp(-i\omega z/v)\alpha_L(\omega)\frac{a^{2L+1}}{r^{L+2}} (L+1-m)N_{Lm}I_{Lm}(\omega,x_0)P_{L+1,m}(\cos\theta). \tag{5.5}$$

If one performs the integral over z, the total energy loss of the electron due to surface excitation is

$$\frac{d\Delta E}{dz} = \frac{e^2}{\pi^2\varepsilon_0 v}\sum_{L=1}^{\infty}\sum_{m=0}^{L} M_{Lm} \int_0^{\infty} d\omega [K_m(\omega x_0/v)]^2(\omega a/v)^{2L+1}\mathrm{Im}[\alpha_L(\omega)], \tag{5.6a}$$

where

$$M_{Lm} = \frac{(2-\delta_{0m})}{(L-m)!(L+m)!}. \tag{5.6b}$$

The differential excitation probability is

$$\frac{dP}{d\omega} = \frac{e^2 a}{\pi^2\varepsilon_0\hbar v}\sum_{L=1}^{\infty}\sum_{m=0}^{L} M_{Lm}[K_m(\omega x_0/v)]^2(\omega a/v)^{2L}\mathrm{Im}[\alpha_L(\omega)]. \tag{5.6c}$$

Two special cases are now considered.

1. *Isolated metal particle*

For a freely suspended sphere in vacuum

$$\mathrm{Im}[\alpha_L(\omega)] = -\mathrm{Im}\left[\frac{2L+1}{L\varepsilon_2(\omega)+L+1}\right]. \tag{5.7}$$

The resonance frequency of the surface plasmon of mode L occurs at

$$L\varepsilon_2(\omega)+L+1=0. \tag{5.8}$$

For free-electron metals

$$\omega_s = \omega_p\sqrt{\frac{L}{2L+1}},\quad L=1,2... \tag{5.9}$$

L is a positive integer which characterizes the mode of plasmon oscillation in the sphere. $\omega_s=\omega_p/\sqrt{3}$, for $L=1$ and $\omega_s\approx\omega_p/\sqrt{2}$ for large L.

To illustrate the meaning of the angular momentum number L, one uses the calculated results of Stratton (1941). For simplicity a free-electron metal particle is considered. The charge wave can be excited to oscillate at particular frequencies. Figure 16 shows the electric and magnetic lines of force for the first four modes of the electric type. $L=1$ and $L=2$ are the dipole and quadruple oscillations, respectively. $L=3$ and high Ls

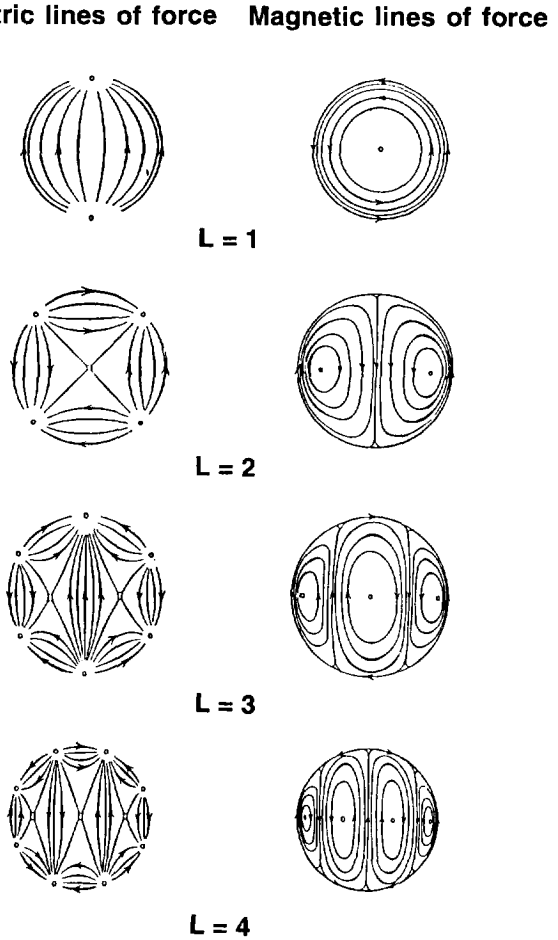

Fig. 16. Schematic lines of force corresponding to the first four modes of electric type in a spherical metal particle.

are the multiple plasmon oscillations. These resonance modes are likely to be excited by the impact of the incident electron, but the spectra are generally dominated by the contributions from the first three modes.

The surface plasmon associated with a spherical particle has been observed experimentally. Figure 17 shows an EELS spectrum of an Al particle, acquired from the transmitted electrons. Besides the volume plasmon appearing at 15 eV, the surface plasmon located at 9 eV is seen; $\omega_s=8.66$ eV for $L=1$, and $\omega_s=10.6$ eV for $L=\infty$. The plasmon peaks produced by different modes are indistinguishable because of the widths of the plasmon peaks.

2. *Single spherical cavity*

For a spherical cavity embedded in an infinitely large dielectric medium (Natta, 1969)

$$\mathrm{Im}[\alpha_L(\omega)] = -\mathrm{Im}\left[\frac{2L+1}{L+\varepsilon_1(\omega)(L+1)}\right]. \tag{5.10}$$

The resonance frequency of the surface plasmon of mode L occurs at

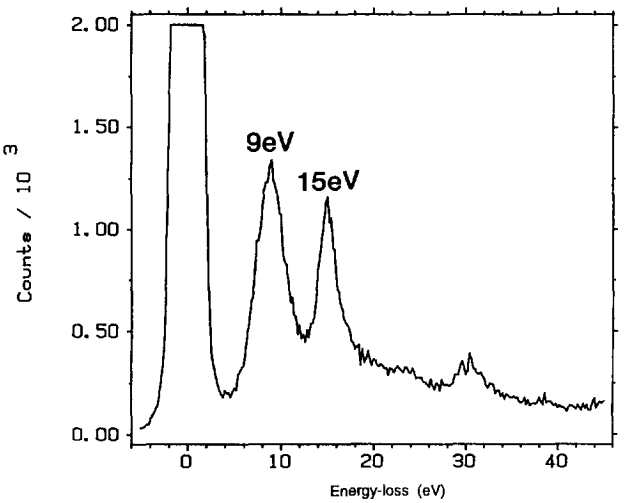

Fig. 17. EELS spectrum of an aluminum spherical particle showing surface plasmon and volume plasmon peaks at 9 and 15 eV, respectively. Beam energy 120 kV.

$$L + \varepsilon_1(\omega)(L+1) = 0. \qquad ()$$

For a bubble in a free-electron metal, the surface plasmon frequencies are

$$\omega_s = \omega_p \sqrt{\frac{L+1}{2L+1}}. \qquad (5.12)$$

B. *Particles with surface oxidation*

In practice, metal particles are usually covered by a thin layer of oxide or adsorbates. For aluminum, the oxide layer is usually unavoidable. The excitation of a dielectric sphere covered by a uniform layer of dielectric function ε_3 can be treated using the procedures given for the spherical particle case (Ferrell *et al.*, 1987). For the dielectric media shown in Fig. 18, the resonance frequencies of surface plasmons are determined by (Ferrell *et al.*, 1987)

$$[\varepsilon_3(\omega)]^2 + \frac{\varepsilon_3(\omega)}{1-g_L}\{\varepsilon_1(\omega)[(L+1)/L + g_L] + \varepsilon_2(\omega)[L/(L+1) + g_L]\} + \varepsilon_1(\omega)\varepsilon_2(\omega) = 0, \qquad (5.13)$$

where $g_L = (a/R)^{2L+1}$, a and R are the inner and outer radii of the surface layer, respectively. The surface- and interface-plasmon excitations in a particle coated with double spherical layers have been given by Ugarte *et al.* (1992).

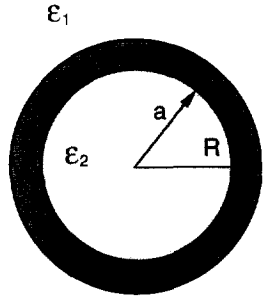

Fig. 18. An isolated spherical particle coated with a dielectric shell.

When a particle is coated with a thin layer of oxide, it may be difficult, particularly when the layer thickness is small, to directly image the layer using conventional imaging techniques. However, the existence of a thin layer on the particle surface can dramatically change the excitation probability of the plasmon peaks. In this case, an energy-filtered electron image can be very useful. Figure 19c shows a set of energy-filtered electron images of a Si particle coated with SiO_2 (Ugarte *et al.*, 1992). Four characteristics plasmon peaks, located at 3.5, 8.5, 17 and 23.5 eV, were observed. The 3.5 and 8.5 eV peaks are the surface/interface plasmons, 17 eV the volume plasmon of Si and 23.5 eV the volume excitation of SiO_2. The energy-filtered image is a map of the excitation probability across the particle for the corresponding plasmon peak, provided a point electron

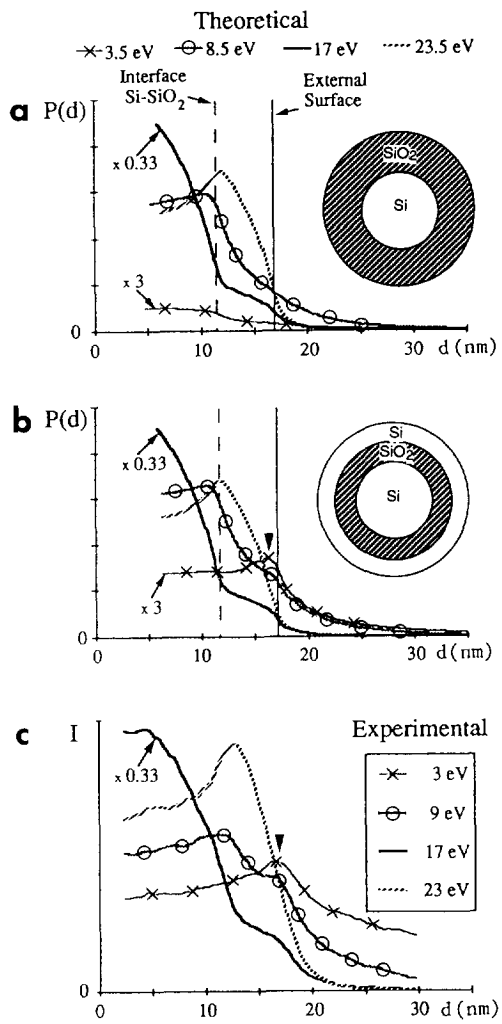

Fig. 19. Comparison between the experimental intensity line profile (c) and the calculated excitation probabilities for the two models (a) and (b), as a function of impact parameter x (Ugarte *et al.*, 1992). The probabilities are obtained using an integration energy window of 1 eV, and a convolution with a Gaussian profile (FWHM 0.94 nm) in order to include the spatial extension of the electron probe.

probe is used. The classical electron energy-loss theory is used to calculate the excitation probability for each beam impact position (or trajectory) with proper consideration of the probe size according to eqn. (3.13b), and the results are shown in Fig. 19a and Fig. 19b for two different models. In contrast to the experimental images shown in Fig. 19a, in which the 3–4 eV plasmon peak exhibits the maximum excitation probability at the external surface (as indicated by an arrowhead), the calculation for model a (Fig. 19a) shows no detectable contrast at the external surface. This fine feature is the only observable evidence using STEM that can discriminate model b from model a. Thus, in addition to the SiO_2 layer, a conductive Si layer exists on the outer surface. Here, energy-filtered imaging is the only technique which can identify the origin of the observed peaks. Energy-filtered electron imaging can also be performed using the signals acquired from ionization edges in STEM, forming compositional sensitive (Leapman and Hunt, 1995) and valence-state-sensitive (Batson, 1994) images.

VI. VALENCE-LOSS SPECTRA OF SUPPORTED PARTICLES

In the last few sections, the surface excitation in small particles was based on an isolated single particle model. The interaction between the particle and the substrate was ignored. This model is usually inappropriate for experimentally attainable systems, in which the particle must be supported by a substrate. The interaction between the particle and the substrate introduces new plasmon peaks due to the coupling and resonance between the interfaces. For a cluster of two oxidized Al spheres, two surface plasmons located at 3.4 and 6.7 eV have been observed (Batson, 1982). The 6.7 eV peak arises from the interface of Al with Al_2O_3. The 3.4 eV peak comes from the excitation of the oxide layer.

A theoretical description of the plasmon excitation in the supported particle case was first considered by Wang and Cowley (1987a) and later by Zabala and Rivacoba (1991). A half-embedded spherical particle model is proposed to study the new resonance frequencies introduced by the interactions among the particle, its oxidation layer and the substrate, as schematically shown in Fig. 20. A metal particle of radius a is surrounded by an oxide layer of thickness $R-a$, where R is the outer radius of the surface layer. The solution of Poisson's equation can be found using the mirror-charge method (Zaremba, 1985; Zabala and Rivacoba, 1991), and the result has been applied to calculate the valence-loss spectra of supported metal particles according to eqn. (2.21) (Rivacoba *et al.*, 1994; Zabala and Rivacoba, 1993).

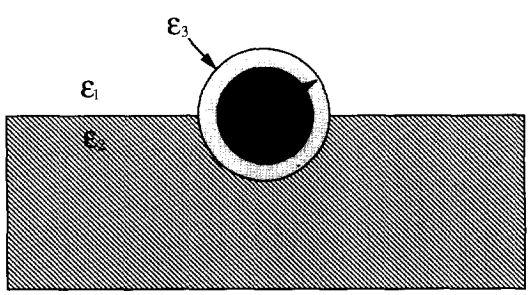

Fig. 20. A half-embedded spherical particle model used in the calculation of plasmon excitations in supported particle case.

The dispersion relations which determine the resonance frequencies of surface plasmons in the supported metal particle system have been given by Wang and Cowley (1987a) and Zabala and Rivacoba (1991). In general, four characteristic surface-plasmon peaks should be observed in the valence spectra for an oxidized metal particle sitting on a large metal substrate (Fig. 21): one from the planar substrate surface (ω_1), one from the substrate–oxide interface (ω_2), one from the metal particle–oxide interface (ω_3), and one from the surface of the oxide shell (ω_4). All these predicted surface plasmon peaks have been observed experimentally (Wang and Cowley, 1987b). Theoretical calculations have been performed to identify the origins of these peaks and experimental results from the energy-filtered plasmon-loss electron images have shown good agreement (Wang and Cowley, 1987a,b; Batson, 1982). In the general case, the number of plasmon peaks equals the number of different interfaces and surfaces in the system.

For an Al sphere sitting on AlF_3, two characteristic resonance frequencies are observed: one from the Al–AlF_3 interface and the other one from the Al spherical

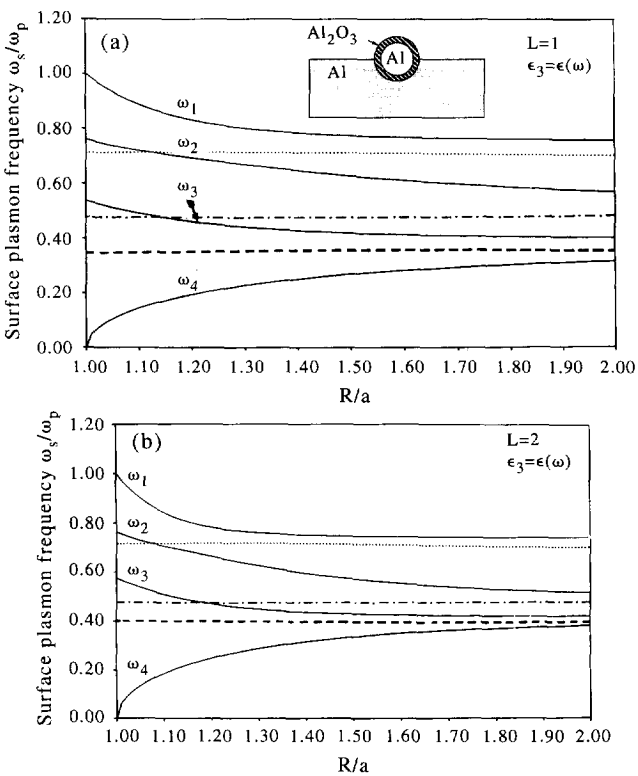

Fig. 21. Surface plasmon frequencies calculated form an oxidized Al particle sitting on an Al substrate using the model shown in Fig. 20 for (a) $L=1$ and (b) $L=2$. (· · ·) plasmon frequency for infinite vacuum–Al planar interface, (– · – · – · –) plasmon for infinite Al_2O_3–Al planar interface, and (– – – –) plasmon of an Al sphere surrounded by a large Al_2O_3 medium.

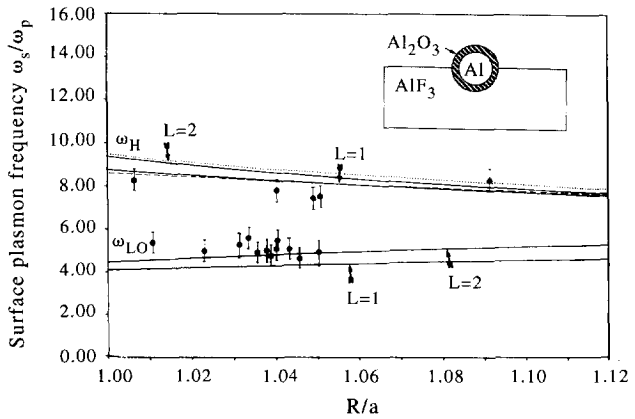

Fig. 22. A comparison of the experimental observed and theoretically calculated surface plasmon resonance frequencies for an oxidized Al particle supported on AlF_3. The dotted and dashed curves represent the theoretical calculation plasmon frequencies for $L=1$ and $L=2$, respectively, when the AlF_3 substrate is absent.

surface. Figure 22 shows a comparison of the theoretically calculated and experimentally observed surface-plasmon energies for a system of an oxidized Al sphere sitting on an AlF_3 substrate as a function of the R/a ratio. The 8 eV peak is due to the excitation of the Al–Al_2O_3 interface; the 4 eV peak is the excitation of the oxide–substrate interface.

The existence of the substrate significantly affects the polarization mode of the metal particle. Figure 23 shows the induced charge distribution for the first few excitation modes of a spherical particle sitting on a substrate (Zabala and Rivacoba, 1991). For even values of L, the effect of both external media is similar to an effective medium of average dielectric response around the sphere and consequently no charge density is induced on the planar interface. For odd Ls, however, the charge oscillations are more complex, indicating a strong effect from the substrate. The half-embedded particle model is easier to solve analytically. Numerical solution is necessary if the particle-support geometry is complex (Ouyang and Issacson, 1989a).

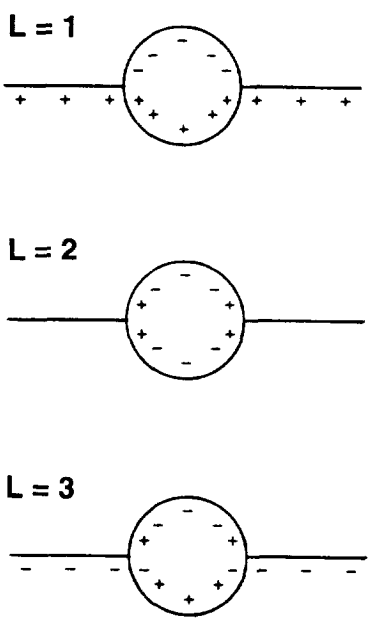

Fig. 23. Calculated surface charge distribution in a half-embedded spherical particle system for $L=1$, 2 and 3 modes.

The valence-loss spectrum for the half-embedded particle model has been calculated by Wang and Cowley (1987c), who solved Poisson's equation in the geometry of Fig. 20. More rigorous calculations have been performed by Rivacoba *et al.* (1992, 1994) and Zabala and Rivacoba (1993) using the semi-classical theory proposed by Echenique *et al.* (1987a). Figure 24 shows a comparison of the calculated EELS spectrum with an experimental spectrum for an Al particle sitting on AlF_3 (Wang and Cowley, 1987c). It is apparent that the calculated spectrum shows a good agreement with the experimental spectrum.

A 3–4 eV low-energy plasmon peak was also observed in EELS spectra of a Si particle coated with SiO_2 (Ugarte *et al.*, 1992). The result was interpreted based on a model of a spherical particle coated with double layers (see Fig. 19), the inner layer being SiO_2 and the outer layer being Si. This Si–SiO_2–Si spherical model accounts for, at least in part, the resonance effect between the particle and the substrate. The 3–4 eV plasmon indeed came from the resonance of the particle and the substrate. The surface plasmon frequencies for a bi-spherical system have been calculated by Schmeits and Dambly (1991), who showed that the 3–4 eV plasmon peak came from the resonance of the two spheres with equal or different radii, in agreement with the observation of Batson (1980, 1982).

Figure 25 gives a comparison of the EELS spectra calculated for different dielectric configurations of an Al sphere sitting on an AlF_3 substrate (Zabala and Rivacoba, 1993). The spectrum from an isolated Al sphere shows two strong peaks located at 8.7 and 9.6 eV. For the half embedded case, the spectrum shape is dramatically changed. Comparing the spectra calculated for the two different excitation positions A and B in the Al/AlF_3 case, the spectrum shapes are very different but the energies of the characteristic peaks remain unchanged. This is because the resonance modes in a dielectric system are an intrinsic property of the

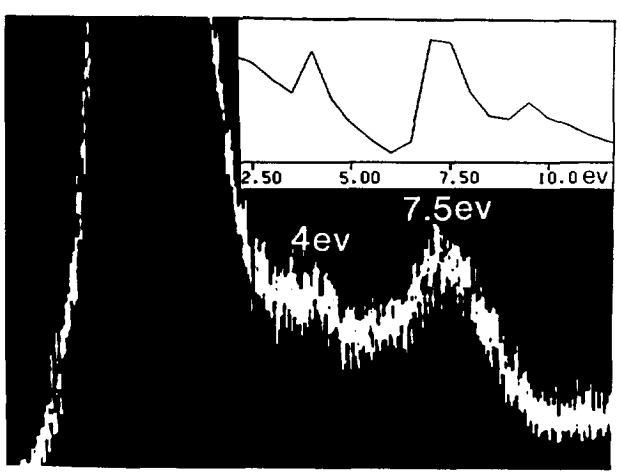

Fig. 24. A comparison of the calculated valence-loss spectrum and an experimental spectrum for an Al particle of 20 nm in diameter sitting on an AlF_3 substrate.

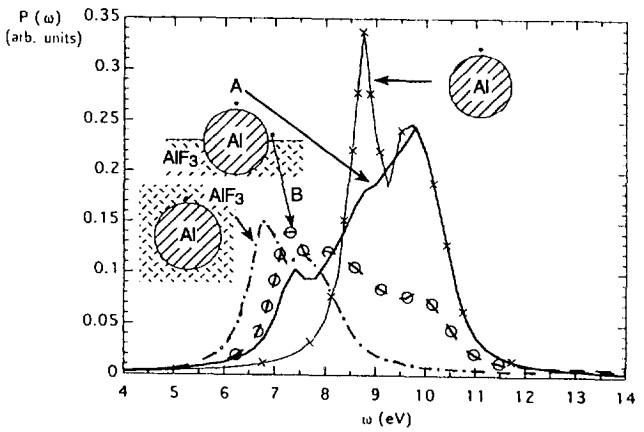

Fig. 25. Calculated EELS spectra for a point electron probe traveling near an Al particle half embedded in AlF_3 medium for trajectories A (dark solid line) and B (dark dashed line). The spectra corresponding to an isolated Al sphere in vacuum (thin solid line) and in AlF_3 (thin dashed line) are also shown for comparison. The particle radius is 10 nm and the impact parameter is 11 nm (from the center of the sphere).

system and are independent of the position and source of excitations, as shown by the calculation of Wang and Cowley (1987b). However, the relative excitation probability of each mode depends sensitively on the position and the impact parameter of the electron beam from the corresponding surface/interface. For an Al sphere embedded in a large AlF_3 medium, the spectrum shifts significantly to low energies, and a 7.5 eV peak in correspondence to the Al–AlF_3 interface appears.

The experimental observations of Batson (1982) proved the above conclusions. Figure 26 shows three experimental EELS spectra acquired for three different excitation positions of an oxidized Al particle sitting on a large Al sphere. With the electron directly positioned on the particle (position A), a strong volume plasmon at 15–16 eV is seen; two surface plasmons located at 4 and 7 eV are also seen. When the probe is moved to position B, the 7 eV peak remains but the 4 eV peak almost disappears. At position C, only the peak at 4 eV remains in the spectrum. These data show that the 4 eV is closely related to the excitation of the Al_2O_3 layer coating on the sphere, while the 7 eV peak is the resonance of the

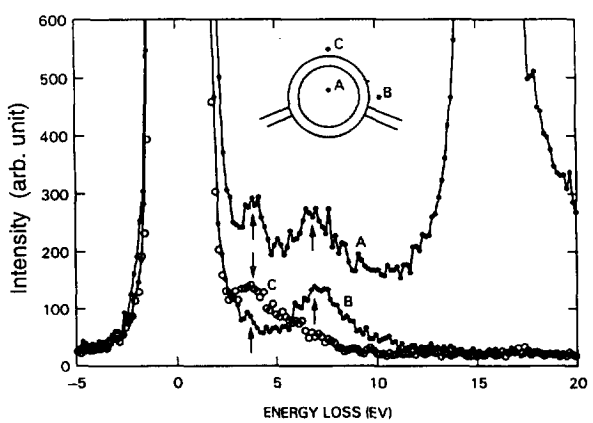

Fig. 26. Valence-loss spectra of a supported Al particle acquired from three excitation positions of the electron probe, as shown in the diagram. The ratio $R/a = 1.4$.

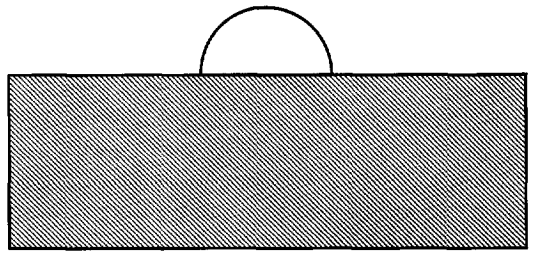

Fig. 27. A model of a hemispherical particle supported by a planar surface.

Al particle with the substrate. It is apparent that the energies of these peaks remain the same although the signal intensity changes with the change of probe impact position.

Another supported-particle case is a hemisphere lying on a flat substrate surface (Fig. 27). This is a good approximation to many practical cases in which the particle shape changes when it is attached onto a substrate. The valence electron excitation in hemisphere particles sitting on a planar surface was first calculated by Wang and Cowley (1987d) and the results showed reasonable agreement with experimental observations (see Fig. 27). The calculations of Rivacoba *et al.* (1995a) for the hemispherical case have shown significant difference in comparison to those of spherical particles, indicating the high sensitivity of the valence-loss spectra to the geometrical configuration of small particles.

VII. VALENCE-LOSS SPECTRA OF CYLINDRICAL INTERFACES

A cylindrical medium is a typical case of electromagnetism. The excitation of a cylindrical object is closely related to the studies of carbon nanotubes and metallic nanowires (Dravid *et al.*, 1993). Recent experiments have shown the shift of the plasmon peak with increase of the tube diameter, or equivalently the number of graphite layers (Bursill *et al.*, 1994; Ajayan *et al.*, 1993). The theoretical modeling of Yannouleas *et al.* (1994) has shown the dimensional crossovers of the volume plasmon in coaxial carbon nanotubes, depending on the number of graphite shells composing the tube.

The valence-loss spectra can provide important electronic-structure information for cylindrical objects and their dielectric response properties. The theoretical scheme for calculating the valence-electron excitation spectra in the cylindrical geometry was first outlined by Chu *et al.* (1984). The theory was extended by Walsh (1989) to calculate the spectra acquired from a cylindrical hole drilled in amorphous AlF_3 by a fine electron probe in STEM. Later, this theory was developed to include the relativistic effect (retardation and Cerenkov radiation) by Walsh (1991), who showed that the non-relativistic solution underestimates the magnitude and overestimates the energy of the surface plasmon modes. The theory is suitable for calculating the spectra acquired when an electron beam is traveling parallel to channels

produced by micro-lithographic techniques (Mamola *et al.*, 1987). Recently, Rivacoba *et al.* (1995b) has calculated the electron energy-loss of a fast electron when it is moving perpendicular to the symmetry axis of the cylinder at an arbitrary impact parameter.

In this section, the basic theoretical scheme is outlined for applying dielectric response theory in the cylindrical system. Figure 28 shows a geometry of fast electron excitation in the cylindrical configuration. The electron is assumed to travel parallel to the cylindrical axis, inside the cylinder. For simplicity, the non-relativistic approximation is made. The potential distribution in space due to a stationary charge at $\mathbf{r}_0=(r, 0, z')$ is determined by

$$\nabla^2\tilde{V}(\mathbf{r},\mathbf{r}_0) = -\frac{e}{\varepsilon\varepsilon_0}\delta(r-r_0)\delta(\phi)\delta(z-z'). \tag{7.1}$$

The solution for eqn. (7.1) is written as

$$\tilde{V}_{\text{in}}(\mathbf{r},\mathbf{r}_0) = \tilde{V}_{\text{e}}(\mathbf{r},\mathbf{r}_0) + \sum_{m=0}^{\infty}(2-\delta_{0\text{m}})\cos(m\phi) \int_{-\infty}^{\infty}\frac{\mathrm{d}k}{2\pi}\exp(ikz)A_{\text{m}}(k,t)K_{\text{m}}(|k|a)I_{\text{m}}(|k|r), \tag{7.2}$$

$V_{\text{e}}(\mathbf{r},t)$ is the potential due to the incident electron:

$$\tilde{V}_{\text{e}}(\mathbf{r},\mathbf{r}_0) = -\frac{e}{2\pi\varepsilon\varepsilon_0}\sum_{m=0}^{\infty}(2-\delta_{0\text{m}})\cos(m\phi) \int_{-\infty}^{\infty}\frac{\mathrm{d}k}{2\pi}\exp[ik(z-vt)]L_{\text{m}}(|k|r,|k|r_0), \tag{7.3}$$

and

$$\tilde{V}_{\text{out}}(\mathbf{r},\mathbf{r}_0) = \sum_{m=0}^{\infty}(2-\delta_{0\text{m}})\cos(m\phi) \int_{-\infty}^{\infty}\frac{\mathrm{d}k}{2\pi}\exp(ikz)B_{\text{m}}(k)I_{\text{m}}(|k|a)K_{\text{m}}(|k|r), \tag{7.4}$$

where A_{m} and B_{m} are coefficients that are determined by the boundary conditions; K_{m} and I_{m} are modified Bessel functions; L_{m} is defined as

$$L_{\text{m}}(|k|r,|k|r_0) = K_{\text{m}}(|k|r)I_{\text{m}}(|k|r_0)\theta(r-r_0) + K_{\text{m}}(|k|r_0)I_{\text{m}}(|k|r)\theta(r_0-r), \tag{7.5}$$

and $\theta(x)$ is a step function defined as: $\theta(x)=1$ for $x>0$ and $q(x)=0$ for $x<0$. The Fourier transform of $\tilde{V}(\mathbf{r},\mathbf{r}_0)$ must be used to determine the A_{m} and B_{m} coefficients, and details have been given by Chu *et al.* (1984). The solution for the valence-loss spectra of a fast electron traveling parallel to the axis of two concentric cylinders (Fig. 29) has been given by Walsh (1989). The concentric cylindrical configuration occurs in cases such as electron beam hole drilling and carbon tubes filled with metals. For carbon tubes smaller than a few nm in diameter, the hydrodynamic model is necessary to predict the dispersion relations (see Section 10; Yannouleas *et al.*, 1994).

VIII. VALENCE-LOSS SPECTRA OF SPHEROIDS AND IRREGULAR-SHAPED MEDIA

The dielectric media described in the last few sections have constant curvatures. In practice, a small particle may have a shape that is neither spherical nor cubic. It becomes difficult or impossible to express the excitation probability of a small particle in an analytical form if its shape deviates from the conventional geometrical configurations. Although it is possible, in principle, to give the solution for a dielectric medium of arbitrary shape in a form of operators (Ouyang and Issacson, 1989b; Cini, 1977), numerical calculation is essential in solving the operator equations.

For a dielectric wedge (Fig. 30a), the parabolic-cylindrical coordinates can be used to solve Poisson's equation if the electron is traveling parallel to the wedge (Martinez-Torregrosa *et al.*, 1990). The excitation of a MgO cube can be approximated as the wedge case if a fine electron probe is positioned parallel to and near a corner of the cube.

Analytical solutions can also be found for dielectric spheroids if the incident electron is traveling parallel to the symmetry axis at an arbitrary impact parameter

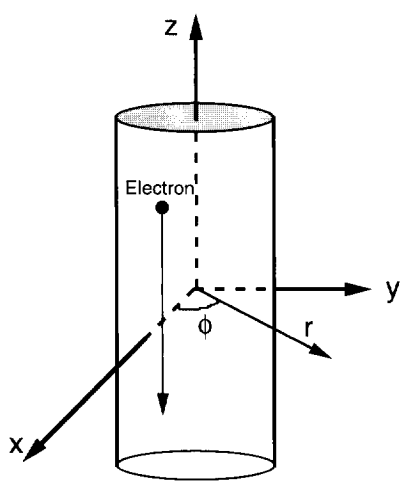

Fig. 28. A schematic model showing valence electron excitation in a cylindrical dielectrics by an external electron beam.

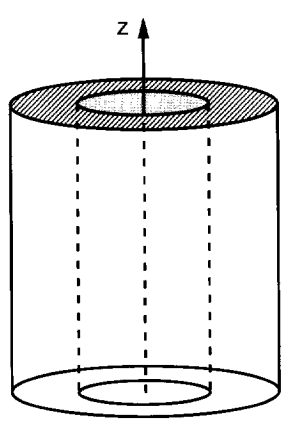

Fig. 29. A coaxial cylinder object that is likely to occur in carbon nanotubes filled with metals.

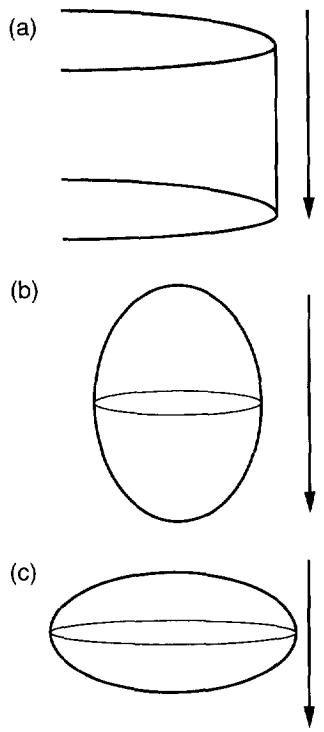

Fig. 30. Schematics showing several irregular dielectric objects that have been analyzed in the literature for valence electron excitation.

(Illman *et al.*, 1988, 1991; Little *et al.*, 1982; Brako *et al.*, 1975). The rotational-parabolic coordinates are used for describing the oblate and prolate dielectric media (Fig. 30b and Fig. 30c). The surface-plasmon frequencies of these media with variable curvature have been tabulated by Brako *et al.* (1975), who also gave the potential distribution near the end of a thin prolate spheroid. This result is useful in studying the potential distribution near the probe tip in scanning tunneling microscopy.

Another type of irregular particle shape is hemispherical (Wang and Cowley, 1987d). The surface-plasmon frequencies of the hemispherical system were given analytically. The valence-loss spectra of a hemisphere as a function of the impact position of the incident electron have been calculated by Rivacoba *et al.* (1995a), who showed the high sensitivity of the spectrum shape to the excitation position of the fine electron probe. The calculations were made based on eqn. (2.21) using the potential generated by a stationary electron located at $\mathbf{r}_0$. For a finite media system, eqn. (2.21) is probably the most effective method for calculating the valence-loss spectra. Figure 31 shows a set of EELS spectra and the energy-filtered images of a non-spherical Al particle sitting on a large AlF_3 substrate. From the energy-filtered electron image of the Al volume plasmon (15 eV), the particle exhibits a hemispherical-like shape. The theoretical calculation of Wang and Cowley (1987d) for a supported hemisphere gives two surface plasmon peaks, located at 10.8 and 4.7 eV. The experimental observation showed peaks at 11 and 3.5 eV. The 3.5 eV peak is due to the resonance of the particle with the support (Fig. 31b), and the 11 eV peak is due to the excitation of the hemisphere particle (Fig. 31c).

IX. VALENCE-LOSS SPECTRA OF COMPOSITE MEDIA

Nanophase and nanocomposite materials have attracted much interest recently. These materials are composed of small particles and a matrix phase so that the collective excitation of the material is a combined excitation of the volumes and interfaces, as shown in Fig. 32. In general, it is difficult to separate the excitation of each individual particle, particular for condensed composite, because of small size and strong overlap. In this section, the effective medium theory is outline for calculating the valence-loss spectra of composite materials.

We start with the example of Al reduction from α-alumina (Al_2O_3) under electron-beam radiation. Figure 33 shows a comparison of the EELS spectra acquired in REM geometry (Wang, 1993) from an alumina surface after being illuminated for different lengths of time under a strong electron beam. After the surface was illuminated for about 4 min, the peak located at 9–10 eV clearly begins to grow. The energy of this peak can be related to the surface-plasmon energy of small aluminium particles. The volume plasmon of Al located at 15 eV does not increase significantly in intensity at this stage because the valence electron excitation is dominated by the surface effect if the particles are small. The alumina peak remains at about the same energy (22 eV). The 15 eV peak became more prominent after the surface was illuminated for 9 min or more, indicating the formation of larger aluminium particles. With the increase of the particle size the excitation probability of the volume plasmon is increased. The excitation of the surface plasmon (9–10 eV) is also strengthened, because the total surface area of the particles is increased.

Evolution of the spectrum shape is due to the formation of aluminium particles on the surface. The Al reduction process is attributed to the electron-beam-induced desorption of oxygen atoms after exciting the internal Auger decay process (Knotek and Feibelman, 1978, 1979; Feibelman and Knotek, 1978). According to the energy level diagram of Al_2O_3, the highest occupied level of the Al^{+3} ion is the Al(2p) level, with a binding energy of 73 eV. If an external electron ionizes this level the dominant decay mode is an inter-atomic Auger process in which one O(2p) electron decays into the Al(2p) hole. This releases about 70 eV of energy which is taken up by the emission of one or two Auger electrons from the O(2p) state. The O^{-2} ion thus loses up to three electrons and becomes a positively charged O^{+1} ion, so will be rejected by the repulsive Coulomb force. The accumulation of Al ions forms Al particles.

In the case of Al metal formed by reduction of alumina, the surface layer is not a uniform dielectric layer but a mixture of small Al particles separated by vacuum. Since many small particles are present under the beam, the dielectric property of this mixed layer can be statistically described by an effective dielectric function (Maxwell-Garnett, 1904, 1906),

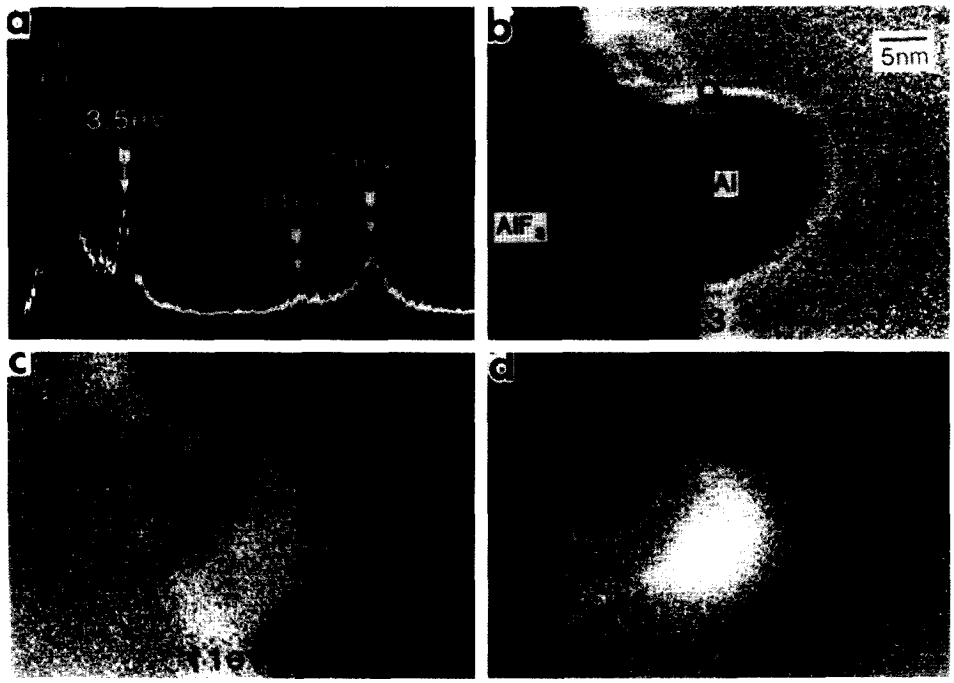

Fig. 31. (a) EELS spectrum acquired from a hemispherical-like particle sitting on an AlF_3 substrate, (b)–(d) are the energy-filtered electron images recorded using the electrons that have suffered 3.5, 11 and 15 eV energy-losses, respectively.

$$\varepsilon' = \varepsilon_B \left\{ \frac{(1+2f_v)\varepsilon_A + 2(1-f_v)\varepsilon_B}{(1-f_v)\varepsilon_A + (2+f_v)\varepsilon_B} \right\}, \qquad (9.1)$$

where ε_A is the dielectric function of the particles with volume fraction f_v mixed in the matrix of dielectric function ε_B. In the case of Fig. 33, ε_A applies to Al and $\varepsilon_B = 1$. The calculation can be made using the electron trajectory shown in Fig. 12b, with consideration of the surface layer by using eqn. (4.1a). Figure 34 shows a comparison of the calculated EELS spectrum with an observed spectrum from an alumina surface with Al reduction. The effective penetration depth of the beam into alumina was chosen as $d_p = 1$ nm. The choice of d_p can sensitively affect the spectral match at higher energies as well as the peak at 22 eV. The thickness of the sandwich layer was taken as $2h = 3$ nm and the volume fraction of the Al particles was chosen to be $f_v = 0.07$. These parameters were chosen in order to match the intensity of the 10 eV surface plasmon peak and the 22 eV alumina plasmon. The choice of the thickness of the sandwich layer is correlated with the choice of the volume fraction f_v, because the average thickness of Al metal is determined by $2hf_v$, which was estimated as 0.2 nm. The peak located at about 9–10 eV is present only when Al particles are a constituent of the sandwich layer, and is obviously the surface plasmon of the Al metal particles.

It must be pointed out that the effective-medium

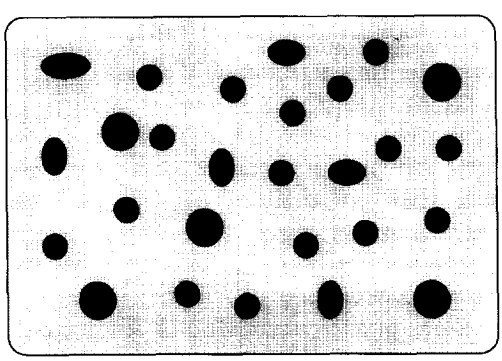

Fig. 32. Model of a composite material composed of spherical particles and a continuous matrix.

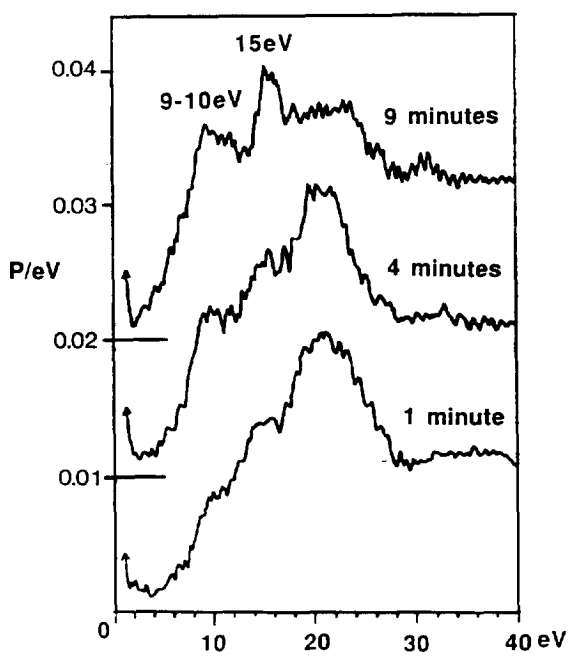

Fig. 33. A comparison of the EELS spectra acquired in REM geometry from an alumina surface at different lengths of illumination time after first seen under the beam. The growth of the 9–10 eV (surface plasmon for Al particles) and 15 eV (volume plasmon of Al) peaks indicates the formation of Al particles.

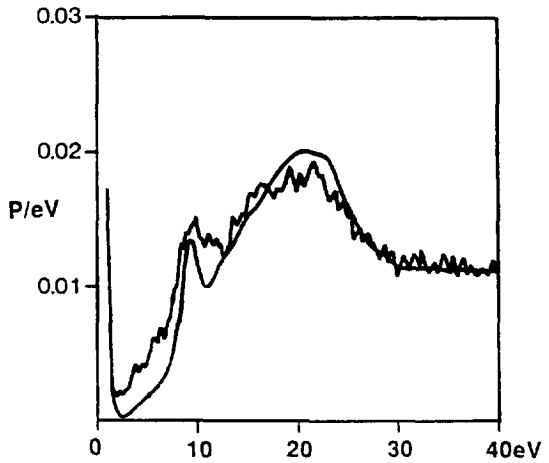

Fig. 34. A comparison of a simulated EELS spectrum in REM geometry according to dielectric response theory and an observed spectrum from the alumina surface in Fig. 33 during the reduction of aluminum.

theory breaks down if the particles are so big that the excitation property of each individual particle cannot be represented by an average excitation. Thus, the calculation cannot fit the spectrum displayed at the top of Fig. 33, especially at the position of the 15 eV peak of the Al volume plasmon, because this peak is the volume excitation of Al. A detailed analysis of the effective-medium theory has been given by Howie and Walsh (1991), who compared several effective-medium models and concluded that, they are only partially successful in explaining the energy-loss spectra observed and do not account for the bulk-loss peak from the minority phase; a simple averaged excitation model, described below, was presented and appeared to give much better results.

The average excitation starts from the bulk energy-loss functions $\mathrm{Im}(-1/\varepsilon_A)$ and $\mathrm{Im}(-1/\varepsilon_B)$ as well as the interface energy-loss function $\mathrm{Im}[-3/(\varepsilon_A+2\varepsilon_B)]$ (for a spherical particle with $L=1$) which is appropriate for a small sphere of material A embedded in material B. The effective energy-loss function is written as (Howie and Walsh, 1991)

$$\mathrm{Im}\left\{-\frac{1}{\varepsilon_{\mathrm{eff}}}\right\} = f_v\left\{\mathrm{Im}\left\{-\frac{1}{\varepsilon_A}\right\} + g_{\mathrm{int}}\left[\mathrm{Im}\left\{-\frac{3}{\varepsilon_A+2\varepsilon_B}\right\} - \mathrm{Im}\left\{-\frac{1}{\varepsilon_A}\right\}\right]\right\} + (1-f_v)\left\{\mathrm{Im}\left\{-\frac{1}{\varepsilon_B}\right\} + g_{\mathrm{ext}}\left[\mathrm{Im}\left\{-\frac{3}{\varepsilon_A+2\varepsilon_B}\right\} - \mathrm{Im}\left\{-\frac{1}{\varepsilon_B}\right\}\right]\right\}. \tag{9.2}$$

where $g_{\mathrm{int}} = 1/(1+3a\omega/v)$, and $g_{\mathrm{ext}} = 2f_v/(1+2f_v)$. In eqn. (9.2), the main terms with factors f_v and $(1-f_v)$ describe the contributions from two types phases which form the composite. The g_{int} and g_{ext} terms give the interface contribution and the corresponding reduction in the bulk contribution. The calculation according to eqn. (9.2) gives the best fit to the Al surface and volume plasmons as well as the spectrum of AlF_3 as in the case of Al reduction from AlF_3. In eqn. (9.2), if the particles are large enough so that the interface excitation is unimportant,

$$\mathrm{Im}\left\{-\frac{1}{\varepsilon_{\mathrm{eff}}}\right\} \approx f_v\mathrm{Im}\left\{-\frac{1}{\varepsilon_A}\right\} + (1-f_v)\mathrm{Im}\left\{-\frac{1}{\varepsilon_B}\right\}. \tag{9.3}$$

Equation (9.3) can be interpreted as follows. In composite materials, the observed valence-loss spectra are considered as a linear superposition of the spectra recorded from each component of the composite, weighted by the volume fraction of the corresponding phase. It is therefore possible to determine the ratio of the two materials contained in the composite, as has been demonstrated by Evans *et al.* (1991) in determination the cross-section depth-profile of Al implanted in $MgAl_2O_4$. This analysis ignores the contribution made by the interfaces but this is a reasonable approximation if the particle sizes are large.

For a general case, eqn. (9.3) is rewritten as

$$\mathrm{Im}\left\{-\frac{1}{\varepsilon_{\mathrm{eff}}}\right\} \approx \sum_{j=1} f_v^{(j)}\mathrm{Im}\left\{-\frac{1}{\varepsilon_j}\right\}, \tag{9.4a}$$

and

$$\sum_{j=1} f_v^{(j)} = 1, \tag{9.4b}$$

where $f_v^{(j)}$ is the volume fraction of phase j with dielectric function ε_j. Therefore, the experimentally observed spectrum is a linear superposition of the spectra acquired from the pure phases, respectively, that compose the material

$$\frac{\mathrm{d}P(\omega)}{\mathrm{d}\omega} = \sum_{j=1} \mathrm{d}_0 f_v^{(j)} \frac{\mathrm{d}^2 P_j(\omega)}{\mathrm{d}\omega \mathrm{d}z}. \tag{9.5}$$

The superposition coefficient is a thickness-integrated fraction of the corresponding phase at the region where the spectrum was acquired. If this analysis is performed for each position of the beam in STEM, a digital image is obtained for the intensity of $[d_0(x,y)\, f_v^{(j)}(x,y)]$ across the specimen. This image is simply the thickness-integrated distribution map of phase j. This technique has been successfully applied to map subcellular distribution of water in frozen-hydrated biological cryosections (Sun *et al.*, 1993, 1995; Leapman *et al.*, 1994), as shown below. A series of detailed data-processing techniques used in this study has been described by Sun *et al.* (1993).

Figure 35 shows a comparison of single-loss valence spectra acquired from several standard specimens which are vitally important in biological science. Each of the compounds has its own characteristic EELS spectrum that is different from others either at the energy-loss region 3–10 eV or at the position of the main peak located approximately at 20–25 eV. These characteristics are the 'finger prints' of those compounds. If the experimentally acquired single-loss EELS spectrum (after data processing) from a real specimen is expressed as a sum of the contributions from the constituent compounds, as listed in Fig. 35, these components are

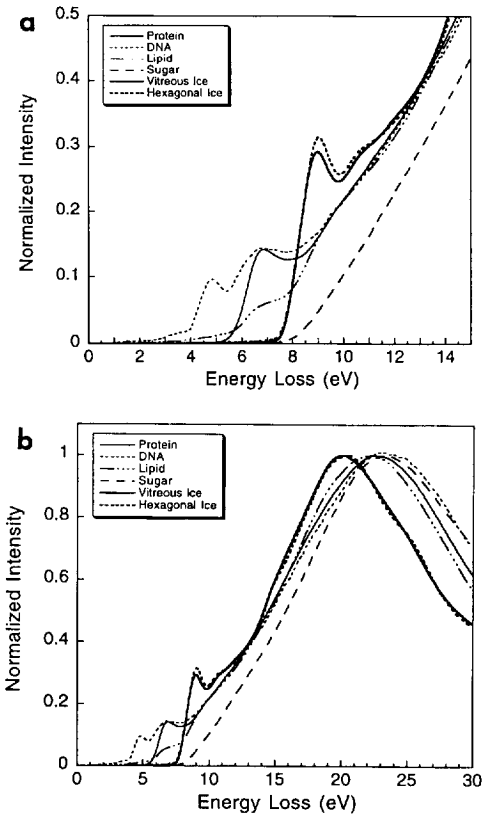

Fig. 35. A comparison of valence EELS spectra acquired from standard specimens of vitreous water, hexagonal ice, protein, lipid, nucleic acid and sucrose in the energy-loss range (a) 0–15 eV and (b) 0–30 eV (Sun *et al.*, 1993). The width of view is 10 mm.

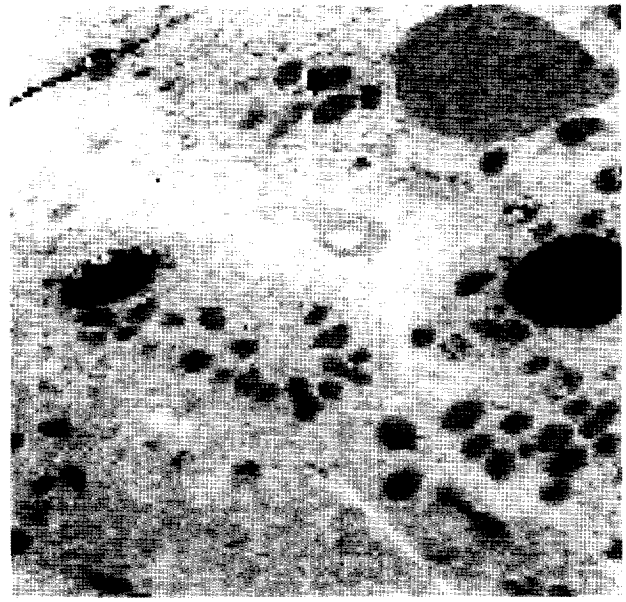

Fig. 36. A thickness-projected water distribution map in a hydrated cryosection as determined by valence-loss EELS in STEM (Sun *et al.*, 1993).

treated as standard reference spectra whose superposition coefficients ($f_v^{(j)}$) can be determined by fitting the observed spectrum with the standard spectra using the multiple least squares technique. Fig. 36 shows a thickness-integrated concentration map of water in a hydrated cryosection (Sun *et al.*, 1995). The brighter contrast indicates higher local thickness-integrated water concentration. This is an excellent example of EELS application in biological science.

X. ELECTRON-DENSITY FLUCTUATION IN SMALL METALLIC PARTICLES AND HYDRODYNAMIC MODEL

In a small metallic particle, the quantized energy levels form a discrete electronic structure. If the energy-level spacing is comparable to or larger than the relevant energy parameters in a physical phenomenon, the discreteness of levels may give rise to anomalies quite distinct from the normal behavior in the bulk material. The imaginary dielectric function of a metal particle is found to be inversely proportional to the size of the particle (Kawabata and Kubo, 1966; Kreibig and Fragstein, 1969). The dependence of the electrical conductivity and dielectric response function for small metal particles have been given by Ruppin and Yatom (1976).

In dielectric response theory, described in all the sections above, the distribution of valence electrons in the scattering object is assumed to be unaffected by the impact of the incident electron, and the charge at the surface was attributed to local polarization. However, a problem is raised when the particle size becomes so small that the number of the valence electrons in the scattering object is no longer large. The electron-density disturbance by the induced surface charges becomes significant in this case. A different theoretical approach must be taken in order to include the effect of electron-density fluctuation in the scattering object (Echenique and Ritchie, 1979).

There are many quantum mechanical theories regarding the plasmon oscillation and damping in metals (Bohm, 1953; Nozieres and Pine, 1958; Ferrell, 1956, 1957; Hasegawa and Watabe, 1969; Hasegawa, 1971). The plasmon is derived from a quantization phenomenon, as represented by the harmonic oscillator model, analogous to a phonon. These theories were developed for large media and cannot be easily modified to calculate the motion of electrons in a small object under the impact of an external charged particle.

To consider density fluctuation in a metallic particle, the free-electron gas model is assumed, so that the electrons are treated as a charged-'fluid' with potential gradient and pressure gradient. This is a hydrodynamic model, in which the behavior of the perturbed electron gas and the electric field are described by a set of linearized hydrodynamic equations (Ritchie, 1957; Fujimoto and Komaki, 1968; Crowell and Ritchie, 1968): (a) the force equation, (b) Poisson's equation and (c) the continuity equation.

$$\frac{\partial}{\partial t}\nabla\tilde{\Phi}(\mathbf{r},t) = -\frac{e}{m}\nabla\tilde{V}(\mathbf{r},t) + \frac{\beta^2}{n_0}\nabla\tilde{n}(\mathbf{r},t), \qquad (10.1a)$$

$$\nabla^2\tilde{V}(\mathbf{r},t) = \frac{e}{\varepsilon_0}[\tilde{n}(\mathbf{r},t) + \delta(x-x_0)\delta(y)\delta(z-vt)], \qquad (10.1b)$$

and

$$\nabla^2\tilde{\Phi}(\mathbf{r},t) = \frac{\partial}{\partial t}\tilde{n}(\mathbf{r},t)/n_0, \qquad (10.1c)$$

where $\tilde{\Phi}(\mathbf{r},t)$ and $\tilde{n}(\mathbf{r},t)$ are perturbations in the velocity potential and electron density, respectively, in the electron gas; n_0 is the electron density in the undisturbed state of the electron gas and β is the root-mean-square (rms) propagation speed of the disturbance through the electron gas. The appropriate boundary conditions are (i) continuity of the electric potential at the surface of the sphere, (ii) continuity of the normal component of the electric displacement at the surface of the sphere, and (iii) the vanishing of the normal component of the disturbance velocity at the surface of the sphere. If one is interested only in the resonance dispersion relation of the system, the delta function term in eqn. (10.1b) can be dropped. If the time-dependent term $\tilde{n}(\mathbf{r},t)$ is expressed as $\tilde{n}(\mathbf{r},t) = \tilde{n}(\mathbf{r})\exp(i\omega t)$, $\tilde{n}(\mathbf{r})$ is determined by

$$\left[\nabla^2 + \frac{\omega^2 - \omega_p^2}{\beta^2}\right]\tilde{n}(\mathbf{r}) = 0, \qquad (10.2)$$

or equivalently

$$[\nabla^2 + \frac{\omega^2 - \omega_p^2}{\beta^2}]\nabla^2\tilde{V}(\mathbf{r}) = 0. \qquad (10.3)$$

The solution of either eqn. (10.2) or eqn. (10.3) would give the dispersion relation of the metal system.

The solution of the hydrodynamic equations has been given analytically for spherical metal particles (Fujimoto and Komaki, 1968; Crowell and Ritchie, 1968; Ruppin, 1978; Barberan and Bausells, 1985), and the final results are quoted here. The plasmon resonance frequency for a small metallic particle is determined by

$$\frac{2L+1}{L}\left(\frac{\omega^2}{\omega_p^2}\right) - 1 = \frac{L+1}{qa}[J_L(qa)/J_L'(qa)], \qquad (10.4)$$

where $q = (\omega^2 - \omega_p^2)^{1/2}$, and $J_L(x)$ is the spherical Bessel function. It is apparent that the resonance frequency depends on the size of the particle. For large-size particles with $qa >> 1$, this result reduces to $\omega = \omega_p\sqrt{\frac{L}{2L+1}}$ [see eqn. (5.9)], just as expected. Ruppin (1978) has shown the increase of volume and surface plasmon energies as well as the FWHM of the volume plasmon peak with a decrease in particle size. Figure 37 shows the calculated surface and volume plasmon frequencies of a spherical metallic particle for the lowest four modes $L = 1$–4. The spatial dispersion shows a significant effect on the energy of the surface plasmon if the particle is smaller than 10 nm in diameter. The plasmon frequencies increase with the decrease of particle size.

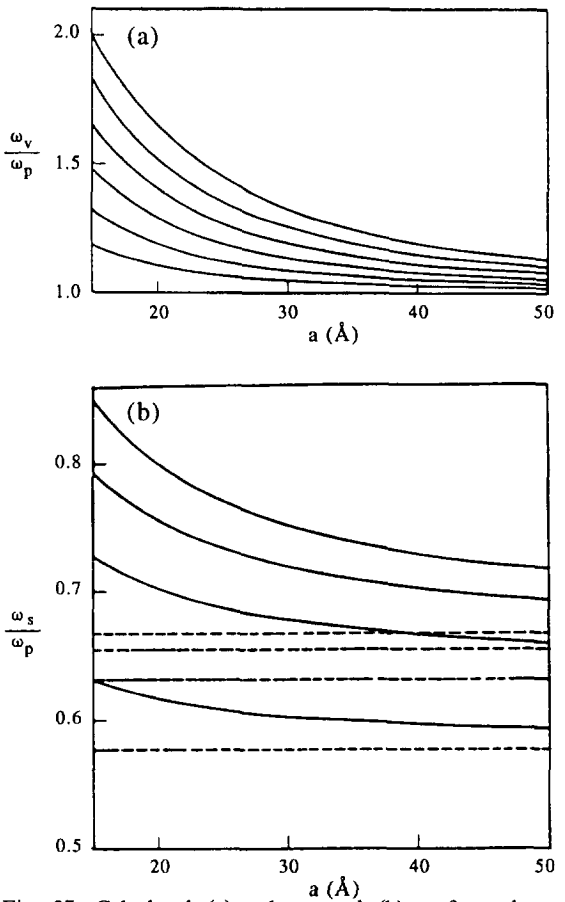

Fig. 37. Calculated (a) volume and (b) surface plasmon frequencies for the lowest four modes of a metal particle, as a function of its radius. Full lines: with spatial dispersion included; broken curves: without spatial dispersion.

Experimental studies of Acheche *et al.* (1986) and Batson *et al.* (1976) have confirmed the theoretically predicted results. The dependence of volume plasmon frequency on particle size is directly related to the dispersion relationship. In the electron-gas model, the frequency is related to the wave vector q by (Lindhard, 1954)

$$\omega^2(q) = \omega^2(q) + \frac{3}{5}v_F^2q^2, \qquad (10.5)$$

where v_F is the Fermi velocity. The review by Schattschneider and Jouffrey (1995) has given a systematic description on the dispersion relation in plasmon excitations. For small particles, the wave vector q is quantized and is determined by the particle size for the reasons described below (Acheche *et al.*, 1986). For a sphere of radius a, the minimum value of q is $\frac{1}{2a}$; the maximum wavelength of the charge fluctuation must be smaller than or equal to the diameter of the sphere. The maximum of q is q_c, thus $\frac{1}{2a} < q < q_c$. From eqn. (10.5), the volume plasmon frequency depends on the radius of the particle, as observed experimentally by Acheche *et al.* (1986). Figure 38 shows a group of experimental data from gallium clusters. The volume plasmon frequency increases significantly when the particle size is small. For

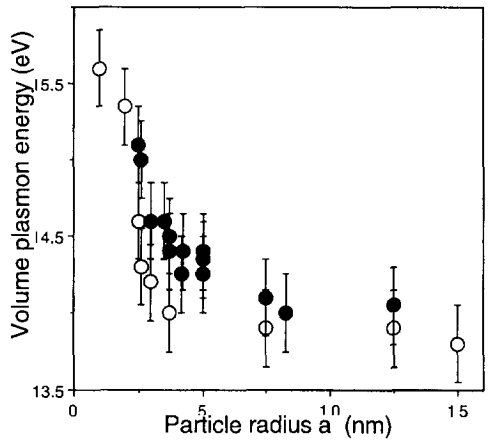

Fig. 38. Variation of the volume plasmon energy in metallic (open circles) and oxidized (solid circles) gallium particles (from Acheche *et al.*, 1986).

particles larger than 10 nm in diameter, the size effect becomes unimportant and the theories presented in the last few sections hold.

When the particle becomes very small, quantum effect may appear in the experimentally observed surface plasmon energy (Ouyang *et al.*, 1992); the surface plasmon energy showed a dip when the particle size decreased from 20 to 4 nm, in contrast to the calculated result shown in Fig. 37. In this case, calculation based on the hydrodynamic model cannot interpret the observed phenomenon. But the origin of this phenomenon is not yet clear.

For cylindrical geometry, the hydrodynamic equations have been solved to describe the dispersion relation in carbon nanotubes (Yannouleas *et al.*, 1994). The results indicate the dimensionality crossovers of the volume plasmon in coaxial carbon nanotubes, depending on the number of graphite layers in the tube. The solution of the hydrodynamic equations for supported metal particles has also been obtained by Wang and Cowley (1987d). For a thin metal slab, the excitation probability was calculated by Ritchie (1957) [e.g. eqn. (3.25)].

XI. LOCALIZATION EFFECT IN SURFACE EXCITATION

Plasmons refer to the collective excitations of the valence electrons in a solid. The charge oscillation associated with the plasmon can reach the entire medium even though the excitation source is a fine electron probe. Therefore, plasmon excitation is usually referred to as a delocalized scattering process which occurs even when the electron is far from the medium. From eqn. (3.13a), the excitation probability of the surface plasmon drops quickly when the incident electron is far from the surface, but the surface excitation still occurs even when the beam impact parameter is larger than 2 nm from the surface (see Fig. 10). It is necessary to estimate the largest impact parameter of an electron before the plasmon excitation occurs. This distance is approximately the localization parameter for the excitation.

The localization effect is best seen in the energy-filtered images formed by the electrons which have suffered energy loss. For a chemically sharp interface of two media, the drop in intensity of the characteristic plasmon peak of one medium as the electron impact parameter increases is a direct measurement of the localization. This experiment has been performed in TEM with the use of an electron energy-filter (Wang and Shapiro, 1995). For a cross-section Al/Ti multilayer media, the volume plasmons of Al and Ti locate at two distinct energies, as shown previously in Fig. 6; it is thus possible to set the energy-filter at the Al peak. The energy-filtered image directly reflects the decrease in the intensity of the 15 eV Al plasmon peak as a function of the impact parameter.

Figure 39a and Fig. 39b show a pair of energy-filtered high-resolution TEM images of a cross-section Al/Ti (111) interface recorded using elastic electrons (0-loss) and Al plasmon-loss electrons, respectively. The crystal lattices are clearly resolved in the 0-loss image. The Al and Ti layers have an epitaxial relation and the interface is (111). The atom rows are clearly resolved. Chemical imaging using atomic inner-shell ionization edges has shown that, at a spatial resolution of 0.4 nm, the interface is chemically sharp (Wang and Shapiro, 1995). In the 15 eV plasmon-loss filtered electron image, the Al side shows stronger intensity, but the interfacial region does not show a sharp transition. The intensity drop across the interface reflects the delocalization effect in plasmon excitation.

To estimate the spatial resolution of the plasmon-loss electron image, a line scan was made across the Al/Ti interface, and the result is shown in Fig. 40. The fine oscillation in the intensity profile is due to the lattice fringes. The intensity profile drops within a distance of 1 nm around the interface, thus, the spatial resolution is approximately 1.0 nm.

To provide a theoretical interpretation regarding the spatial resolution observed in the plasmon-loss electron image shown in Fig. 40, eqn. (3.13a) is applied to calculate the plasmon-loss intensity as a function of the electron impact distance from the interface, the result is shown in Fig. 41 for an energy window of $13 < \Delta E < 17$ eV. The intensity drop at the interface is qualitatively in agreement with the experimental observation shown in Fig. 40. The spatial resolution is half of the width within which the intensity drops from the flat Al region to the flat Ti region. Although the interface was assumed to be chemically sharp in the calculation, the spatial resolution is limited to about 1 nm.

A quantum mechanical description of image formation in STEM has been outlined by Kohl and Rose (1985), and the theory was applied to calculate the energy-filtered plasmon-loss electron image of small metal particles in STEM (Kohl, 1983). A recent calculation by Muller and Silcox (1995) has shown that a resolution approaching 0.5 nm can be achieved in energy-filtered images using valence-loss electrons.

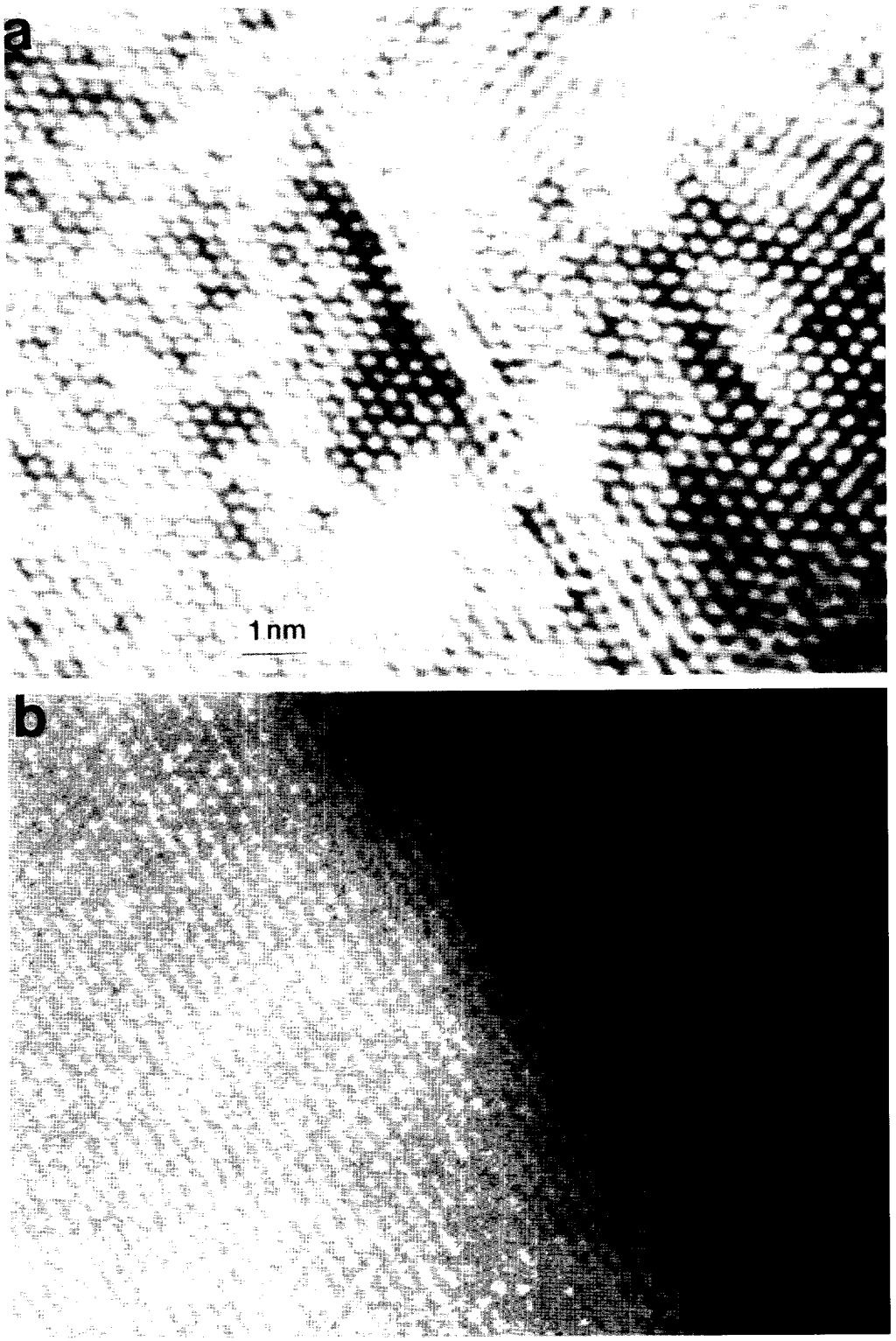

Fig. 39. (a) Zero-loss and (b) 15 eV Al-plasmon loss energy-selected high-resolution TEM images of an Al/Ti (111) interface, showing the localization effect of plasmon excitation at interfaces. Energy window width $\Delta = 4$ eV. Beam azimuth [110].

XII. QUANTUM THEORY OF VALENCE ELECTRON EXCITATION

The classical dielectric response theory is a convenient method for describing valence excitations in high-energy electron scattering, and it has shown remarkable success even for particles smaller than a few nanometers. For metals under the free-electron approximation, quantum mechanical charge-density fluctuation theory (Ashley and Ferrell, 1976) has shown equivalent results to those obtained using dielectric response theory (Ritchie, 1981; Ritchie and Howie, 1988). In the excitations of small metal particles, both theories have given identical results (Ferrell and Echenique, 1985). The review given by Echenique *et al.* (1990) is a comprehensive description of the dynamic interaction of a fast ion with condensed

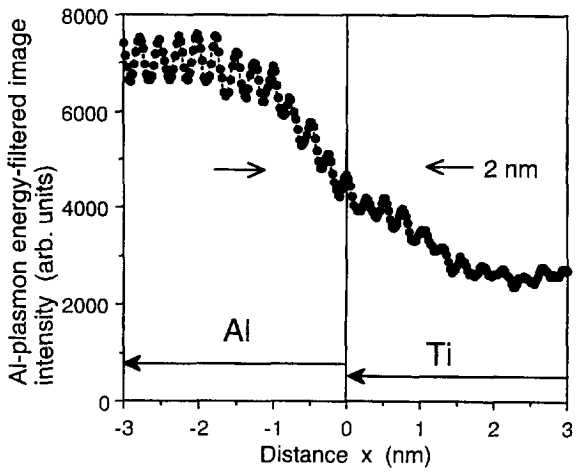

Fig. 40. An intensity line scan across the Al/Ti interface from the image recorded using the 15 eV Al-plasmon-loss electron image (Fig. 37b), showing the dependence of inelastic absorption function on the impact parameter x of the electron from the interface. This curve determines the spatial resolution of valence-loss electron imaging.

matter. In this section, the equivalence of dielectric response theory with the quantum theory is proved for a general case. This exercise is necessary to establish the basis of the classical theory.

A. *Quantum mechanical basis of classical theory*

Figure 42 shows schematically a many-particle system of electrons undergoing perturbation by a fast electron with velocity $\mathbf{v} = v\hat{z}$. The coordinates of the electrons are referred to some arbitrary origin at a point O. We omit spin indices for simplicity and only consider spin-independent interactions. Eigenstates and eigenenergies of the crystal electrons are represented by $|n>$ and $\hbar\omega_n$, respectively. The $|n>$ states are assumed orthonormal and complete, and the index n represents all observable quantum states characteristic of the system. A plane wave basis set is taken for the incident electron: $\exp(2\pi i\mathbf{K}\cdot\mathbf{r})$. The Hamiltonian H′ characterizing inter-

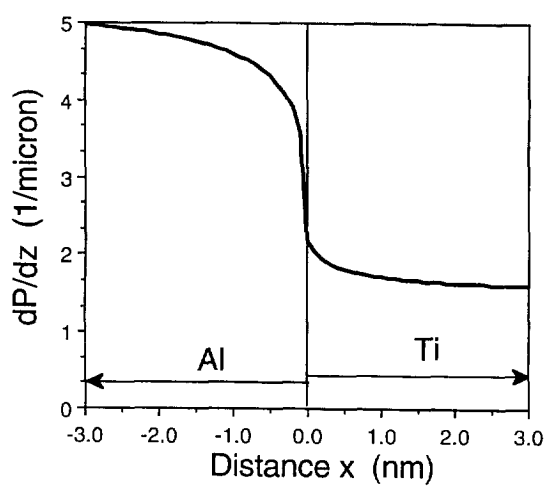

Fig. 41. Calculated excitation probability across an Al/Ti interface for an energy loss in a range of $13 < \Delta E < 17$ eV. The interface position is indicated by a vertical line.

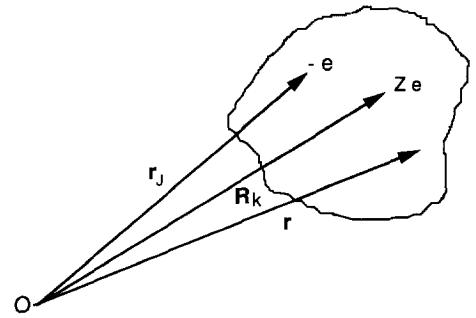

Fig. 42. Interaction of an external electron with the electrons and nuclei in a dielectric media system.

action between the fast electron and the crystal electrons is

$$H'(\mathbf{r}) = \sum_J \frac{e^2}{4\pi\varepsilon_0|\mathbf{r}-\mathbf{r}_J|} - \sum_k \frac{Z_k e^2}{4\pi\varepsilon_0|\mathbf{r}-\mathbf{r}_k|}, \tag{12.1}$$

where $\mathbf{r}_J$ and $\mathbf{R}_k$ are the positions of the Jth crystal electron and the kth nucleus of charge $Z_k e$, respectively.

The standard first-order perturbation theory is applied to obtain the cross-section for excitation of a transition of the many-electron system from its ground state $|0>$ to a state $|n>$, accompanied by the transition of the fast electron between momentum eigenstates characterized by wave vectors $\mathbf{K}$ (with $\mathbf{v} = h\mathbf{K}/\mathbf{m}_0$) and $\mathbf{K}_f$. From the Golden rule

$$\sigma_{n0} = \frac{2\pi}{\hbar^2 v}\sum_{K_f} |<n|\int d\mathbf{r}\exp[2\pi i\mathbf{k}\cdot\mathbf{r}]\frac{1}{4\pi\varepsilon_0} \left\{\sum_J \frac{e^2}{|\mathbf{r}-\mathbf{r}_J|} - \sum_k \frac{Z_k e^2}{|\mathbf{r}-\mathbf{R}_k|}\right\} |0>|^2 \delta(E/\hbar - E_f/\hbar - \omega_{n0}), \tag{12.2}$$

where $\omega_{n0} = \omega_n - \omega_0$, $\mathbf{k} = \mathbf{K} - \mathbf{K}_f$, E and E_f stand for the energy of the incident electron before and after interacting with the crystal. The delta function stands for the conservation of energy. The contribution by nuclei will be dropped because of the orthonormal property of $|n>$. The sum over K_f is to integrate the contributions made by the electron excitations of different momentum transfers but the same energy-loss. Changing variables:

$$E - E_f = \frac{h^2}{2m_0}(K^2 - K_f^2) = \frac{h^2}{2m_0}(2\mathbf{k}\cdot\mathbf{K} - k^2) = h\mathbf{k}\cdot\mathbf{v} - \frac{h^2k^2}{2m_0}, \tag{12.3}$$

carrying out the integral over $\mathbf{r}$ in (12.2) and using an identity

$$\int d\mathbf{r}\frac{\exp(-2\pi i\mathbf{u}\cdot\mathbf{r})}{|\mathbf{r}-\mathbf{r}'|} = \frac{\exp(-2\pi i\mathbf{u}\cdot\mathbf{r}')}{\pi u^2}, \tag{12.4}$$

yields

$$\sigma_{n0} = \frac{2\pi}{\hbar^2 v}\left[\frac{e^2}{4\pi\varepsilon_0}\right]^2 \sum_{K_f} \frac{|\rho_{n0}(\mathbf{k})|^2}{\pi^2 k^4}\delta(E/\hbar - E_f/\hbar - \omega_{n0}), \tag{12.5a}$$

where

$$\rho_{n0}(\tau) = <n|\sum_J \exp(-2\pi i\tau\cdot\mathbf{r}_J)|0> \tag{12.5b}$$

is the matrix element of the density operator. For fast electrons, the sum over K_f can be replaced by an integral, thus

$$\sigma_{n0} = \frac{2}{\pi\hbar^2 v}\left[\frac{e^2}{4\pi\varepsilon_0}\right]^2 \int d\mathbf{k}\frac{|\rho_{n0}(\mathbf{k})|^2}{k^4}\delta(2\pi\mathbf{k}\cdot\mathbf{v} - 2\pi^2\hbar k^2/m_0 - \omega_{n0}). \tag{12.6}$$

To introduce an impact parameter conjugate for momentum transfer, the recoil of the incident electron is ignored; that is, the term proportional to k^2 in the argument of the delta function is dropped (Ritchie, 1981). The larger v becomes, the less important will be the neglected term. Thus eqn. (12.6) is approximated as

$$\sigma_{n0} \approx \frac{2}{\pi\hbar^2 v}\left[\frac{e^2}{4\pi\varepsilon_0}\right]^2 \int d\mathbf{k}\frac{\rho_{n0}(\mathbf{k})}{k^2} \int d\mathbf{u}\frac{\rho^*_{n0}(\mathbf{u})}{u^2}\delta(\mathbf{k}-\mathbf{u})\delta(2\pi\mathbf{k}\cdot\mathbf{v} - \omega_{n0}). \tag{12.7}$$

Making use of an identity

$$\delta(\mathbf{k}_b - \mathbf{u}_b) = \int d\mathbf{b}\exp[2\pi i(\mathbf{k}_b - \mathbf{u}_b)\cdot\mathbf{b}] \tag{12.8}$$

in order to express eqn. (12.6) in terms of a spatial variable $\mathbf{b}$, where $\mathbf{b}=(b_x,b_y,0)$, $\mathbf{k}_b=(k_x,k_y,0)$ and $\mathbf{u}_b=(u_x,u_y,0)$. Eqn. 12.7 may be rewritten as

$$\sigma_{n0} = \frac{2}{\pi\hbar^2 v}\left[\frac{e^2}{4\pi\varepsilon_0}\right]^2 \int d\mathbf{k}\frac{|\rho_{n0}(\mathbf{k})|^2}{k^4}\delta(2\pi\mathbf{k}\cdot\mathbf{v} - \omega_{n0}) = \frac{4}{\hbar^2}\left[\frac{e^2}{4\pi\varepsilon_0}\right]^2 \int d\mathbf{b}|\int d\mathbf{k}\frac{\rho_{n0}(\mathbf{k})}{k^2} \exp[2\pi i\mathbf{k}\cdot\mathbf{b}]\delta(2\pi k_z v - \omega_{n0})|^2. \tag{12.9}$$

Expressing the energy-conserving delta function in terms of an integral over time, i.e.

$$\delta(2\pi k_z v - \omega_{n0}) = \frac{1}{2\pi}\int dt\exp[2\pi i k_z v t - i\omega_{n0}t], \tag{12.15}$$

and writing out the matrix element, s_{n0} may be expressed as an integral over impact parameter $\mathbf{b}$,

$$\sigma_{n0} = \int d\mathbf{b}|a_{n0}(\mathbf{b})|^2, \tag{12.16a}$$

where

$$a_{n0}(\mathbf{b}) = \frac{1}{i\pi\hbar}\frac{e^2}{4\pi\varepsilon_0}\int d\mathbf{k}\frac{\rho_{n0}(\mathbf{k})}{k^2}\exp[2\pi i\mathbf{k}\cdot\mathbf{b}] \int dt\exp[2\pi i k_z v t - i\omega_{n0}t] = \frac{1}{i\hbar}\int_{-\infty}^{\infty} dt <n|\left\{\sum_J \frac{e^2}{4\pi\varepsilon_0|\mathbf{b}+v\hat{z}t-\mathbf{r}_J|}\right\} |0> \times\exp[-i\omega_{n0}t] = \frac{1}{i\hbar}\int_{-\infty}^{\infty} dt <n|H'|0>\exp[-i\omega_{n0}t]. \tag{12.16b}$$

Therefore, a_{n0} may be regarded as the probability amplitude that the crystal electron system will experience a transition under the influence of the Coulomb field of a classical point electron traveling with constant velocity v along a path specified by the impact parameter b, beginning at $z = -\infty$ and ending at $z = \infty$. As is not surprising, eqn. (12.16b) agrees exactly with the result of a first-order quantum perturbation derivation of this probability amplitude, in which the interaction Hamiltonian H′ is taken in the classically prescribed, time-dependent form:

$$H' = \sum_J \frac{e^2}{4\pi\varepsilon_0|\mathbf{b}+v\hat{z}t-\mathbf{r}_J|}. \tag{12.17}$$

The result presented in eqn. (12.16a) and eqn. (12.16b) has been generalized by Ritchie and Howie (1988) for a case in which the incident electron beam is not a plane wave but a converged electron probe in STEM. They showed that, when all inelastically scattered electrons are collected, the measured probability of exciting a given transition may be computed theoretically as if the microprobe consisted of an incoherent superposition of classical trajectories distributed lateral to the beam direction according to the probe intensity function.

B. *Density operator and dielectric response theory*

Before starting from eqn. (12.9) to derive dielectric response theory, the density operator is considered first. In inelastic electron scattering, an important quantity is the so called mixed dynamic form factor which is related to the density operator by (Kohl and Rose, 1985; Kohl, 1995; Wang, 1995)

$$S(\mathbf{u},\mathbf{u}')\sum_{n\neq 0}\rho_{0n}(\mathbf{u})\rho_{n0}(-\mathbf{u}'). \tag{12.18}$$

The role played by $S(\mathbf{u},\mathbf{u}')$ in inelastic scattering is equivalent to that taken by the crystal potential V in elastic scattering. $S(\mathbf{u},\mathbf{u}')$ and $V(\mathbf{r})$ are the only two structurally related quantities that determine the behavior of electron scattering in crystals. The mixed dynamic form factor is directly related to the generalized dielectric function $e_{uu'}(\omega)$ (Kohl and Rose, 1985) by

$$S(\mathbf{u},\mathbf{u}') = \int_{-\infty}^{\infty} d\omega \frac{2\pi i\hbar\varepsilon_0}{e^2[1-\exp(-\hbar\omega/k_B T)]} \left\{\frac{\tau^2}{\varepsilon_{\mathbf{uu}'}(\omega)} - \frac{\tau^2}{\varepsilon^*_{\mathbf{u}'\mathbf{u}}(\omega)}\right\}. \quad (12.19)$$

If one takes a special case with $\mathbf{u}=\mathbf{u}'$, eqn. (12.19) is simplified as

$$S(\mathbf{u},\mathbf{u}) = \sum_{n\neq 0} |\rho_{n0}(\mathbf{u})|^2 = \int_{-\infty}^{\infty} d\omega \frac{4\pi\hbar\varepsilon_0}{e^2[1-\exp(-\hbar\omega/k_B T)]} u^2 \mathrm{Im}\left\{-\frac{1}{\varepsilon_{\mathbf{uu}}(\omega)}\right\}, \quad (12.20)$$

where $\mathrm{Im}\left\{-\frac{1}{\varepsilon_{\mathbf{uu}}(\omega)}\right\} = \mathrm{Im}\left\{-\frac{1}{\varepsilon(\omega,\mathbf{u})}\right\}$ is just the energy-loss function.

For valence electron excitation, the condition $|\hbar\omega| > > k_B T$ is always satisfied. Thus, the integration of ω from $-\infty$ to 0 vanishes in eqn. (12.20), since $[1-\exp(-\hbar\omega/k_B T)]^{-1} \approx 0$. Under this approximation, eqn. (12.20) becomes

$$S(\mathbf{u},\mathbf{u}) = \frac{4\pi\hbar\varepsilon_0}{\mathbf{e}^2} \int_0^{\infty} d\omega\, u^2\, \mathrm{Im}\left\{-\frac{1}{\varepsilon(\omega,\mathbf{u})}\right\}. \quad (12.21)$$

The total excitation probability of the crystal electrons is now calculated. Summing over n in eqn. (12.9) for all valence states n ($n > 0$),

$$\sigma_t = \sum_{n\neq 0} \sigma_{n0} = \frac{2}{\pi\hbar^2 v}\left[\frac{e^2}{4\pi\varepsilon_0}\right]^2 \sum_{n\neq 0} \int d\mathbf{k} \frac{1}{k^4} \delta(2\pi k_z v - \omega_{n0}) |\rho_{n0}(\mathbf{k})|^2. \quad (12.22)$$

This procedure is carried out in order to include the excitations of all the possible crystal valence states which, in practice, means collecting electrons scattered to all different angles with different energy-losses. The energy conservation law requires $\hbar\omega_{n0} = \hbar\omega$ (for an energy-loss $\hbar\omega$). Substituting eqn. (12.18) into eqn. (12.22) and using eqn. (12.21), one finds

$$\frac{d\sigma_t}{d\omega} = \frac{e^2}{4\pi^3\varepsilon_0\hbar v^2} \int dk_x \int dk_y \frac{1}{k_x^2 + k_y^2 + (\omega/2\pi v)^2} \mathrm{Im}\left\{-\frac{1}{\varepsilon(\omega,\mathbf{k})}\right\} \approx \frac{e^2}{4\pi^2\varepsilon_0\hbar v^2} \mathrm{Im}\left\{-\frac{1}{\varepsilon}\right\} \ln[1 + (2\pi u_c v/\omega)^2]. \quad (12.23)$$

This is identical to eqn. (3.17). Thus, the equivalence of classical dielectric response theory and quantum transition theory is proven. This equivalence is based on assumptions that all the scattered electrons of different energies and wave vectors are collected by the spectrometer and that the relativistic effect is ignored. For valence electron excitation, the collection angle of the spectrometer is usually much larger than the characteristic scattering angle $\Theta_E \approx \Delta E/2E_0$, typically about 0.1 mrad, where E_0 is the energy of the incident electron; almost all the electrons are collected if diffraction effects are weak.

The classical theory and the quantum theory can be compared in the following aspects. (1) If one is interested in the angular distribution (or dispersion relation) of inelastically scattered electrons, the quantum theory must be used, because the electron trajectory defined in classical theory cannot describe the electron angular distribution as a result of scattering. (ii) The multiplasmon effect (Sunjic and Lucas, 1971), which refers to the excitation of more than one plasmon in a single scattering process (Ashley and Ritchie, 1970; Spence and Spargo, 1971; Schattschneider *et al.*, 1987), is ignored in the classical theory. The quantum mechanical theory of Lucas and Sunjic (1972) has considered this effect although its excitation probability is very small. (iii) The wave property of an incident electron is ignored in classical electron energy-loss theory. For an electron probe of finite size, the theory needs to be modified to include the shape function of the electron probe (Ritchie and Howie, 1988). The relativistic effect can also be easily included in the classical theory.

In conclusion, the classical theory, particularly in cases where the geometrical configuration of the dielectric media is complex, is the most convenient method for interpreting valence-electron excitation. This theory should be applicable to almost all experimental situations unless the quantum size effect is significant.

XIII. SUMMARY

Plasmon oscillations characterize the response of a dielectric medium to the stimulation of an external charged particle. Valence-loss spectra represent the interband transitions and the modes of collective excitation of valence electrons. Surface plasmons are resonance modes of surface charges induced by a fast moving electron in different geometrical configurations. In this article, we have reviewed the classical electron energy-loss theory for calculating the resonance modes and excitation probabilities of plasmons in condensed matter. The objective of this review was to provide a comprehensive coverage, starting from fundamental equations, of dielectric response theory and its applications for calculating the excitation probability (as a function of the impact parameter/position) of plasmons in thin films, surfaces, interfaces, isolated particles and supported particles. The article is aimed at providing a guidance for readers who are interested in quantitative valence-loss spectroscopy. The classical energy-loss theory is equivalent to the quantum mechanical theory, provided all the scattered electrons are collected by the spectrometer. The hydrodynamic model was introduced to include the fluctuation of electron density when the particle size is smaller than 10 nm.

With increasing interest in nanophase and nanostructured materials, characterizing the interband transition of each individual nanoparticle is relevant to many problems of practical importance. Quantized energy levels are expected to occur in the valence band when the particle size is less than 10 nm. Valence-loss spectroscopy performed using a fine electron probe in scanning transmission electron microscopy is a unique technique that will provide the dielectric response information from a small region. This review provides a systematic theoretical description of the technique. More experimental research is necessary to establish and expand the applications of valence-loss spectroscopy in materials science.

XIV. NOTE

FORTRAN source codes have been developed for using eqn. (3.10a) and eqn. (3.25), to calculate single-loss spectra of interface/surface excitations and surface and volume excitations in a thin crystal slab in TEM, respectively. A FORTRAN source code has also been developed for calculating single-loss valence electron excitation spectra acquired in REM geometry. These programs will be freely provided by the author, upon request via e-mail.

Acknowledgements—Thanks to Profs J. M. Cowley, C. Colliex, R. F. Egerton and A. Howie for timely advice which guided the author into the field of valence-electron excitation and plasmon oscillations. The author is grateful to Drs P. E. Batson, C. Colliex, R. Garcia-Molina, R. D. Leapman, A. Rivacoba and S. Q. Sun for kindly providing some of the illustrations used in the text. Thanks also go to Prof. A. Howie and Prof. R. F. Egerton for critical reading of the manuscript.

REFERENCES

Acheche, M., Colliex, C. and Trebbia, P., 1986. Characterization of small metallic clusters by electron energy-loss spectroscopy. *Scanning Electron Microsc.*, **I,** 25–32.

Ajayan, P. M., Iijima, S. and Ichihashi, T., 1993. Electron energy-loss spectroscopy of carbon nanometer-size tubes. *Phys. Rev. B*, **47,** 6859–6862.

Ashley, J. C. and Ferrell, T. L., 1976. Excitation by fast electrons of surface plasmons on spherical voids in a metal. *Phys. Rev. B*, **14,** 3277–3281.

Ashley, J. C. and Ritchie, R. H., 1970. Double-plasmon excitation in free-electron gas. *Phys. Stat. Sol.*, **38,** 425–434.

Ashley, J. C., Tung, C. J. and Ritchie, R. H., 1979. Electron inelastic mean free paths and energy losses in solids. I. aluminum metal. *Surf. Sci.*, **81,** 409–426.

Bah, M. L., Akjouj, A. and Dobrzynski, L., 1992. Response functions in layered dielectric media. *Surf. Sci. Rep.*, **16,** 95–131.

Barberan, N. and Bausells, J., 1985. Plasmon excitation in metallic spheres. *Phys. Rev. B*, **31,** 6354–6359.

Barrachina, R. O. and Gras-Marti, A., 1992. Note on the energy lost by a charged particle specularly reflecting at a surface. *Ultramicroscopy*, **45,** 345–349.

Batson, P. E., 1994. EELS at biried interfaces: pushing towards atomic resolution. *Microsc. Soc. Am. Bull.*, **24,** 371–374.

Batson, P. E., 1983. Surface plasmon scattering on flat surface at grazing incidence. *Ultramicroscopy*, **11,** 299–302.

Batson, P. E., 1982. A new surface plasmon resonance in clusters of small aluminum spheres. *Ultramicroscopy*, **9,** 277–282.

Batson, P. E., 1980. Damping of bulk plasmons in small aluminum spheres. *Solid State Commun.*, **34,** 477–480.

Batson, P. E., Chen, C. H. and Silcox, J., 1976. Plasmon dispersion at large wave vectors in Al. *Phys. Rev. Lett.*, **37,** 937–940.

Batson, P. E. and Silcox, J., 1983. Experimental energy-loss function $\mathrm{Im}[-1/\varepsilon(\omega,q)]$, for aluminum. *Phys. Rev. B*, **27,** 5224–5239.

Bohm, D., 1953. A collective description of electron interactions: III. Coulomb interaction in a degenerate electron gas. *Phys. Rev.*, **92,** 609–625.

Bolton, J. P. R. and Chen, M., 1995. Electron energy loss in multilayered slabs. *Ultramicroscopy*, **60,** 247–263.

Born, M. and Wolf, E., 1980. *Principle of Optics: Electromagnetic Theory of Propagation, Interference and Diffraction of Light.* Pergmon, New York, pp. 633–663.

Brako, R., Hrncevic, J. and Sunjic, M., 1975. Curvature dependence of surface phonon and plasmon frequencies. *Z. Physik, B*, **21,** 193–201.

Bursill, L. A., Stadelmann, P. A., Peng, J. L. and Prawer, S., 1994. Surface plasmon observed for carbon nanotubes. *Phys. Rev. B*, **49,** 2882–2887.

Chu, Y. T., Warmack, R. J., Ritchie, R. H., Little, J. W., Becker, R. S. and Ferrell, T. L., 1984. Contribution of the surface plasmon to energy-losses by electrons in a cylindrical channel. *Particle Accelerators*, **6,** 13–17.

Cini, M., 1977. Dielectric response of arbitrary surfaces and size quantized metals. *Surf. Sci.*, **62,** 148–1640.

Colliex, C., 1984. Electron energy-loss spectroscopy in the electron microscope. In: *Advances in Optical and Electron Microscopy*, V. E. Cosslett and R. Barer (eds). Academic Press, London, vol. 9, pp. 65–177.

Cowley, J. M., 1982. Surface energies and surface structure of small crystals studied by use of a STEM instrument. *Surf. Sci.*, **114,** 587–606.

Cowley, J. M. and Wang, Z. L., 1986. Defocused dark-field image of crystal surfaces. *Ultramicroscopy*, **19,** 217–224.

Crowell, J. and Ritchie, R. H., 1968. Radiative decay of Coulomb-stimulated plasmons in spheres. *Phys. Rev.*, **172,** 436–440.

Dravid, V. P., Lin, X. W., Wang, Y. Y., Wang, X. K., Yee, A., Ketterson, J. B. and Chang, R. P. H., 1993. Buckytubes and derivatives: their growth and implications for Buckyball formation. *Science*, **259,** 1601–1602.

Echenique, P. M., Bausells, J. and Rivacoba, A., 1987. Energy-loss probability in electron microscopy. *Phys. Rev. B*, **35,** 1521–1524.

Echenique, P. M., Flores, F. and Ritchie, R. H., 1990. Dynamic screening of ions in condensed matter. *Solid State Phys.*, **43,** 229–312.

Echenique, P. M., Howie, A. and Wheatley, D. J., 1987. Excitation of dielectric spheres by external electron beams. *Phil. Mag. B*, **56,** 335–345.

Echenique, P. M. and Pendry, J., 1975. Absorption profiles at surfaces. *Phys. C*, **8,** 2936–2945.

Echenique, P. M., Ritchie, R. H., Barberan, N. and Inkson, J., 1981. Semiclassical image potential at a solid surface. *Phys. Rev. B*, **20,** 2567–2580.

Echenique, P. M. and Ritchie, R. H., 1979. Spatial excitation patterns induced by swift ions in condensed matter. *Phys. Rev. B*, **23,** 6486–6492.

Echenique, P. M. and Howie, A., 1985. Image force effects in electron microscopy. *Ultramicroscopy*, **16,** 269–272.

Economou, E. N., 1969. Surface plasmons in thin films. *Phys. Rev.*, **182,** 539–554.

Egerton, R. F., 1986. *Electron Energy-Loss Spectroscopy in the Electron Microscope.* Plenum Press, New York.

Evans, N. D. and Wang, Z. L., 1992. Separating the surface and volume plasmon energy-loss intensity distributions in MgO and $MgAl_2O_4$. *Proc. 50th Ann. Meet. of Electron Microsc. Soc. America*, G. W. Bailey, J. Bentley and J. A. Small (eds). San Francisco Press, San Francisco, pp. 1256–1257.

Evans, N. D., Zinkle, S. J., Bentley, J. and Kenik, E. A., 1991. Quantification of metallic aluminum profiles in Al^+ implanted $MgAl_2O_4$ spinal by electron energy-loss spectroscopy. *Proc. 49th Ann. Meet. of Electron Microsc. Soc. America*, G. W. Bailey (ed.). San Francisco Press, San Francisco, pp. 728–729.

Feibelman, P. J. and Knotek, M. L., 1978. Reinterpretation of electron-stimulated desorption data from chemisorption systems. *Phys. Rev. B*, **18,** 6531–6539.

Ferrell, R. A., 1957. Characteristic energy-loss of electrons passing through metal foils. II. Dispersion relation and short wavelength cutoff for plasmon oscillations. *Phys. Rev.*, **107,** 450–462.

Ferrell, R. A., 1956. Angular dependence of the characteristic energy-loss of electrons passing through metal foils. *Phys. Rev.*, **101,** 554.

Ferrell, T. L. and Echenique, P. M., 1985. Generation of surface excitations on dielectric spheres by an external electron beam. *Phys. Rev. Lett.*, **55**, 1526–1529.

Ferrell, T. L., Warmack, R. J., Anderson, V. E. and Echenique, P. M., 1987. Analytical calculation of stopping power for isolated small sphere. *Phys. Rev. B*, **35**, 7365–7371.

Fujimoto, F. and Komaki, K., 1968. Plasmon oscillations excited by a fast electron in a metallic particle. *J. Phys. Soc. Japan*, **25**, 1679–1687.

Garcia-Molina, R., Gras-Marti, A., Howie, A. and Ritchie, R. H., 1985. Retardation effects in the interaction of charged particle beams with bounded condensed media. *J. Phys. C Solid State Phys.*, **18**, 5335–5345.

Geiger, J., 1967. Inelastic electron scattering in thin films at oblique incidence. *Phys. State Sol.*, **24**, 457–460.

Gervasoni, J. L. and Arista, N. R., 1992. Energy-loss and plasmon excitation during electron emission in the proximity of a solid surface. *Surf. Sci.*, **260**, 329–346.

Gumbs, G. and Horing, N. J. M., 1991. Plasma losses by charged particles in thin films: effects of spatial dispersion, phonon, and magnetic field. *Phys. Rev. B*, **43**, 2119–2130.

Hasegawa, M., 1971. Theory of plasmon damping in metals: II. Effects of electron–ion interaction. *J. Phys. Soc. Japan*, **31**, 649–667.

Hasegawa, M. and Watabe, M., 1969. Theory of plasmon damping in metals: I. General formulation and application to an electron gas. *J. Phys. Soc. Japan*, **27**, 1393–1414.

Howie, A., 1988. Localized surface imaging and spectroscopy in the scanning transmission electron microscope. In: *Surface and Interface Characterization by Electron Optical Methods*, A. Howie and U. Valdre (eds). Plenum Press, New York.

Howie, A., 1983. Surface reaction and excitation. *Ultramicroscopy*, **11**, 141–148.

Howie, A. and Milne, R. H., 1985. Excitations at interfaces and small particles. *Ultramicroscopy*, **18**, 427–434.

Howie, A. and Milne, R. H., 1984. Electron energy-loss spectra and reflection images from surfaces. *J. Microsc.*, **136**, 279–285.

Howie, A. and Walsh, C., 1991. Interpretation of valence-loss spectra from composite media. *Microsc. Microanal. Microstruct.*, **2**, 171–181.

Hunt, J. A., 1991. An example of spectrum imaging used for comparison of EELS quantitative analysis techniques on Al–Li. *Proc. 49th Ann. Meet. of Electron Microsc. Soc. America*, G. W. Bailey (ed.). San Francisco Press, San Francisco, pp. 726–727.

Illman, B. L., Anderson, V. E., Warmack, R. J. and Ferrell, T. L., 1991. Energy-loss profiles of transmitted electrons incident on dielectric spheroids. *Ultramicroscopy*, **35**, 1–10.

Illman, B. L., Anderson, V. E., Warmack, R. J. and Ferrell, T. L., 1988. Spectrum of surface-mode contribution to the differential energy-loss probability by electrons passing by a spheroid. *Phys. Rev. B*, **38**, 3045–3049.

Johnson, D. W., 1975. A Fourier method for numerical Kramers–Kronig analysis. *J. Phys. A (math., Gen., Phys.)*, **8**, 490–495.

Joy, D. C., Luo, S., Dunlap, J. R., Williams, D. and Cao, S., 1994. Stopping-power determination for compound by EELS. *Proc. 52th Ann. Meet. of Electron Microsc. Soc. America*, G. W. Bailey and A. J. Garratt-Reed (eds). San Francisco Press, San Francisco, pp. 948–949.

Kawabata, A. and Kubo, R., 1966. Electronic properties of fine metallic particles. II. Plasmon resonance absorption. *J. Phys. Soc. Japan*, **21**, 1765–1772.

Kliewer, K. L. and Fuchs, R., 1974. Theory of dynamical properties of dielectric surfaces. In: *Aspects of the Study of Surfaces*, I. Prigogine and S. A. Rice (eds). Wiley, U.K., vol. 27, pp. 355–541.

Knotek, M. L. and Feibelman, P. J., 1979. Stability of ironically bonded surfaces in ionizing environments. *Surf. Sci.*, **90**, 78–90.

Knotek, M. L. and Feibelman, P. J., 1978. Ion desorption by core-hole Auger decay. *Phys. Rev. Lett.*, **40**, 964–967.

Kohl, H., 1983. Image formation by inelastically scattered electrons: image of a surface plasmon. *Ultramicroscopy*, **11**, 53–66.

Kohl, H. and Rose, H., 1985. Theory of image formation by inelastically scattered electrons in the electron microscope. *Adv. Electron. Electron Phys.*, **65**, 173–227.

Kreibig, U. and Fragstein, C. V., 1969. The limitation of electron mean free path in small silver particles. *Z. Physik*, **224**, 307–323.

Kröger, E., 1970. Transition radiation, Cerenkov radiation and energy-losses of relativistic charged particles traversing thin foils at oblique incidence. *Z. Physik*, **235**, 403–421.

Kuzuo, K., Terauchi, M. and Tanaka, M., 1992. Electron energy-loss spectra of carbon nanotubes. *Jpn. J. Appl. Phys.*, **31**, L1484–1487.

Leapman, R. D. and Hunt, J. A., 1995. Compositional imaging with electron energy loss spectroscopy. *J. Microsc. Soc. Am.*, **1**, 93–108.

Leapman, R. D., Sun, S. Q., Hunt, J. A. and Andrews, S. B., 1994. Biological electron energy loss spectroscopy in the field-emission STEM. *Scanning Microsc. (Suppl.)*, **8**, 245–259.

Lin, X. W., Wang, Y. Y., Dravid, V. P., Michalalcos, P. M. and Kung, M. C., 1993. Valence states and hybridization in vanadium oxide systems investigated by transmission EELS. *Phys. Rev. B*, **47**, 3477–3481.

Lindhard, J., 1954. On the properties of a gas of charged particles. *Dan. Vidensk. Selsk. Mat. Fys. Medd.*, **28**, 1–57.

Little, J. W., Ferrell, T. L., Callcott, T. A. and Arakawa, E. T., 1982. Radiative decay of surface plasmons in oblate spheroids. *Phys. Rev. B*, **26**, 5953–5956.

Lucas, A. A. and Sunjic, M., 1972. Fast-electron spectroscopy of collective excitations in solids. *Prog. Surf. Sci.*, **2**, 75–137.

Mahan, G. D., 1990. *Many-Particle Physics*, 2nd edn. Plenum Press, New York, pp. 459–474.

Mamola, K. C., Warmack, R. J. and Ferrell, T. L., 1987. Surface-plasmon excitation by electrons in microlithographically produced channels. *Phys. Rev. B*, **35**, 2682–2686.

Marks, L. D., 1982. Observation of the image force for fast electrons near an MgO surface. *Solid State Commun.*, **43**, 727–729.

Martinez-Torregrosa, A., Garcia-Molina, R. and Gras-Marti, A., 1990. Electron beam deflection by a dielectric wedge. *Ultramicroscopy*, **34**, 283–287.

Maxwell-Garnett, J. C., 1906. Colors in metal glasses and in metallic films, solution II. *Phil. Trans. Roy. Soc.*, **205**, 237–288.

Maxwell-Garnett, J. C., 1904. Colors in metal glasses and in metallic films. *Phil. Trans. Roy. Soc.*, **203**, 385–420.

Mullejans, H., Bleloch, A. L., Howie, A. and Tomita, M., 1993. Secondary electron coincidence detection and time of flight spectroscopy. *Ultramicroscopy*, **52**, 360–368.

Muller, D. A. and Silcox, J., 1995. Delocalization in inelastic scattering. *Ultramicroscopy*, **59**, 195–213.

Natta, M., 1969. Surface plasmon oscillations in bubble. *Solid State Commun.*, **7**, 823–825.

Nozieres, P. and Pine, D., 1958. Electron interaction in solids. General formulation. *Phys. Rev.*, **109**, 741–761.

Otto, A., 1967. Theory of plasmon excitation in thin films by electrons of non-normal incidence. *Phys. Stat. Sol.*, **22**, 401–406.

Ouyang, F., Batson, P. E. and Issacson, M., 1992. Quantum size effects in the surface-plasmon excitation of small metallic particles by electron-energy-loss spectroscopy. *Phys. Rev. B*, **46**, 15421–15425.

Ouyang, F. and Issacson, M., 1989. Accurate modeling of particle–substrate coupling of surface plasmon excitation in EELS. *Ultramicroscopy*, **31**, 345–350.

Ouyang, F. and Issacson, M., 1989. Surface plasmon excitation of objects with arbitrary shape and dielectric constant. *Phil. Mag. B*, **60**, 481–492.

Palik, E. D. (ed.) 1985. *Handbook of Optical Constants of Solids*. Academic Press, Inc., London.

Raether, H., 1980. *Excitation of Plasmons and Interband Transitions by Electrons*. Springer–Verlag, New York.

Raether, H., 1967. Surface plasmon oscillations as a tool for surface examinations. *Surf. Sci.*, **8**, 233–246.

Richter, H. and Geiger, J., 1981. Energy-losses of fast electrons in multi-layer systems. *Z. Phys. B—Condensed Matter*, **42**, 39–45.

Ritchie, R. H., 1981. Quantum aspects of the spatial resolution of energy-loss measurements in electron microscopy. I. Broad-beam geometry. *Phil. Mag. A*, **44**, 931–942.

Ritchie, R. H., 1957. Plasma losses by fast electrons in thin films. *Phys. Rev.*, **106**, 874–881.

Ritchie, R. H. and Howie, A., 1988. Inelastic scattering probabilities in scanning transmission electron microscopy. *Phil. mag. A*, **58**, 753–767.

Rivacoba, A., Aizpurua, J. and Zabala, N., 1995a. Target geometry dependence of electron energy- losses spectra in scanning transmission electron microscopy (STEM). *Scanning Microsc.*, **9**, 927–938.

Rivacoba, A., Apell, P. and Zabala, N., 1995b. Energy loss probability of STEM electrons in cylindrical surfaces. *Nucl. Meth. Instrum.*, **B96**, 465–469.

Rivacoba, A., Zabala, N. and Apell, P., 1994. Energy-loss of STEM electrons in coupled surfaces. *Surf. Sci.*, **307-309**, 868–873.

Rivacoba, A., Zabala, N. and Echenique, P. M., 1992. Theory of energy-loss in scanning transmission electron microscopy of supported small particles. *Phys. Rev. Lett.*, **69**, 3362–3365.

Ruppin, R., 1978. Plasmon frequencies of small metal spheres. *J. Phys. Chem. Solids*, **39**, 233–237.

Ruppin, R. and Yatom, H., 1976. Size and shape effects on the broadening of the plasma resonance absorption in metals. *Phys. Stat. Sol. b*, **74,** 647–654.

Schattschneider, P., Födermayr, F. and Su, D. S., 1987. Coherent double-plasmon excitation in aluminum. *Phys. Rev. Lett.*, **59,** 724–727.

Schattschneider, P. and Jouffrey, B., 1995. Plasmons and related excitations. In: *Energy Filtering Transmission Electron Microscopy*. Springer Series in Optical Science, Springer–Verlag, **71,** pp. 151–224.

Schmeits, M., 1981. Inelastic scattering of fast electrons by spherical surfaces. *J. Phys. C: Solid State Phys.*, **14,** 1203–1216.

Schmeits, M. and Dambly, L., 1991. Fast-electron scattering by bispherical surface-plasmon modes. *Phys. Rev. B*, **44,** 12706–12712.

Schmeits, M. and Lucas, A. A., 1977. Physical adsorption and surface plasmon. *Surf. Sci.*, **64,** 176–196.

Smythe, W., 1950. *Static and Dynamic Electricity*. McGraw–Hill Book Company, Inc., New York.

Spence, J. C. H. and Spargo, A. E. C., 1971. Observation of double-plasmon excitation in aluminum. *Phys. Rev. Lett.*, **26,** 895–897.

Stern, E. A. and Ferrell, R. A., 1960. Surface plasmon oscillations of a degenerate electron gas. *Phys. Rev.*, **120,** 130–136.

Stratton, J. A., 1941. *Electromagnetic Theory*. McGraw-Hill, New York, pp. 393–419; 555–573.

Sun, S. Q., Shi, S.-L., Hunt, J. A. and Leapman, R. D., 1995. Quantitative water mapping of cryosectioned cells by electron energy loss spectroscopy. *J. Microsc.*, **177,** 18–30.

Sun, S. Q., Shi, S.-L. and Leapman, R. D., 1993. Water distributions of hydrated biological specimens by valence electron energy loss spectroscopy. *Ultramicroscopy*, **50,** 127–139.

Sunjic, M. and Lucas, A. A., 1971. Multiple plasmon effects in the energy-loss spectra of electrons in thin films. *Phys. Rev. B*, **3,** 719–729.

Tougaard, S. and Kraaer, J., 1991. Inelastic-electron-scattering cross sections for Si, Cu, Ag, Au, Ti, Fe and Pd. *Phys. Rev. B*, **43,** 1651–1661.

Tung, C. J., Ashley, J. C. and Ritchie, R. H., 1979. Electron inelastic mean free paths and energy losses in solids. II. Electron gas statistical model. *Surf. Sci.*, **81,** 427–439.

Ugarte, D., Colliex, C. and Trebbia, P., 1992. Surface- and interface-plasmon modes on small semiconducting spheres. *Phys. Rev. B*, **45,** 4332–4343.

Wang, Y. Y., Zhang, H. and Dravid, V. P., 1993a. Electronic structure and dielectric function of oxide superconductors via transmission EELS with a cold field emission TEM. *Ultramicroscopy*, **52,** 523–532.

Wang, Y. Y., Zhang, H., Dravid, V. P., Han, P. D. and Payne, D. A., 1993b. Anisotropic dielectric function and electronic structure of infinite layer compound (Sr1-xCax)yCuO$_2$. *Phys. Rev. B*, **48,** 9810–9814.

Wang, Y. Y., Zhang, H., Dravid, V. P., Shi, D., Hinks, D. G., Zheng, Y. and Jorgensen, J. D., 1993c. Evolution of the low energy excitation and dielectric function of Ba1-xKxBiO3 with K- doping ($0 < x < 0.5$). *Phys. Rev. B*, **47,** 14503–14509.

Wang, Y. Y., Feng, G. F., Sutto, T. E. and Shao, Z., 1991. Dielectric function of BaBiO3 investigated by electron-energy-loss spectroscopy and ellipsometry. *Phys. Rev. B*, **44,** 7098–7101.

Wang, Y. Y. and Ritter, A. L., 1991. Optical excitations in Bi2Sr2CaCu2O8 and Bi2Sr2CuO6 by electron energy loss spectroscopy. *Phys. Rev. B*, **43,** 1241–1244.

Wang, Z. L., 1995. *Elastic and Inelastic Scattering in Electron Diffraction and Imaging*. Plenum Press, New York.

Wang, Z. L., 1996. *Reflection Electron Microscopy and Spectroscopy for Surface Analysis*. Cambridge University Press, U.K.

Wang, Z. L., 1993. Electron reflection, diffraction and imaging of bulk crystal surfaces in TEM and STEM. *Rep. Prog. Phys.*, **56,** 997–1065.

Wang, Z. L., 1991. Reflection electron imaging and spectroscopy studies of metal reduction at alpha-alumina (0,-1,2) surfaces. *J. Microsc.*, **163,** 261–274.

Wang, Z. L. and Cowley, J. M., 1987a. Surface plasmon excitation for supported metal particles. *Ultramicroscopy*, **21,** 77–94.

Wang, Z. L. and Cowley, J. M., 1987b. Generation of surface plasmon excitation of supported metal particles by an external electron beam. *Ultramicroscopy*, **21,** 347–366.

Wang, Z. L. and Cowley, J. M., 1987c. Excitation of the supported metal particle surface plasmon with external electron beam. *Ultramicroscopy*, **21,** 335–346.

Wang, Z. L. and Cowley, J. M., 1987d. Size and shape dependence of the surface plasmon frequencies for supported metal particle systems. *Ultramicroscopy*, **21,** 97–108.

Wang, Z. L. and Shapiro, A. J., 1995. Energy-filtering and composition-sensitive imaging in surface and interface studies using HREM. *Ultramicroscopy*, **60,** 115–135.

Walls, M. G. and Howie, A., 1989. Dielectric theory of localized valence energy-loss spectroscopy. *Ultramicroscopy*, **28,** 40–42.

Walsh, C. A., 1991. An analytical expression for the energy-loss of fast electrons traveling parallel to the axis of a cylindrical interface. *Phil. Mag. B*, **63,** 1063–1078.

Walsh, C. A., 1989. Analysis of electron energy-loss spectra from electron-beam-damaged amorphous AlF_3. *Phil. Mag. A*, **59,** 227–246.

Yannouleas, C., Bogachek, E. N. and Landman, U., 1994. Dimensionality crossovers of the s plasmon in coaxial carbon nanotubes. *Phys. Rev. B*, **50,** 7977–7980.

Yuan, J., 1989. Determination of the microscopic optical dielectric function of a material. *Inst. Phys. Conf. Ser. No 98* Chap. 2, pp. 45–48.

Yubero, F. and Tougaard, S., 1992. Model for quantitative analysis of reflection-electron-energy-loss spectra. *Phys. Rev. B*, **46,** 2486–2497.

Zabala, N. and Echenique, P. M., 1990. Energy-loss of fast electrons moving near plane boundaries with dispersive media. *Ultramicroscopy*, **32,** 327–335.

Zabala, N. and Rivacoba, A., 1993. Electron energy-loss near supported particles. *Phys. Rev. B*, **48,** 14534–14542.

Zabala, N. and Rivacoba, A., 1991. Support effects on the surface plasmon modes of small particles. *Ultramicroscopy*, **35,** 145–150.

Zaremba, E., 1985. Van der Waals interaction between an atom and a surface defect. *Surf. Sci.*, **151,** 91–102.

Zhang, H., Wang, Y. Y. and Dravid, V. P., 1993. Anisotropic dielectric properties of YBa2Cu4O8 investigated by EELS. *Physica C*, **208,** 231–237.